Faculty of Engineering & Faculty of Science
The Chinese University of Hong Kong

Joint Faculty Research Day
12 June 2008

Designed by Faculty of Science

Today's Programme

Morning Session

9:30-10:00am **Keynote Address**
Prof. YUE On Ching Science Advisor, Innovation and Technology Commission
Innovation and Technology Development in Hong Kong

10:00-10:50am **Forum on collaborative research and grant applications**
Chairman: Prof. WONG Kam Fai (Faculty of Engineering)
Panel: Prof. YUE On Ching (ITC, HKSAR); Prof. XU Yangsheng & Dean Peter YUM (Faculty of Engineering); Dean KWAN Hoi Shan & Prof. Samuel SUN (Faculty of Science)

10:50-11:20am *Coffee Break*

11:20-11:40am **General introduction of research activities in Faculty of Science**
Prcf. Raymond CHAN, Associate Dean (Research), Faculty of Science

11:40-12:00nn **General introduction of research activities in Faculty of Engineering**
Prcf. Helen MENG, Associate Dean (Research), Faculty of Engineering

12:00-1:30pm **Lunch and posters presentation** in Reading Room, 6/F Ho Sin Hang Engineering Bldg.

Afternoon Session: Thematic Talks

Chairman: Prof Raymond CHAN

1:30-1:50pm **Prof. KONG Siu Kai** Department of Biochemistry
My story on surface plasmon resonance development

1:50-2:10pm **Prof. DU Ruxu** Department of Mechanical and Automation Engineering
Introduction to precision engineering

2:10-2:30pm **Prof. JIANG Liwen** Department of Biology
Protein dynamics and organelle biogenesis in plant cells

2:30-2:50pm **Prof. Thierry BLU** Department of Electronic Engineering
Detection of brain activity using wavelets in functional MRI

2:50-3:10pm **Prof. Jimmy YU** Department of Chemistry
Fabrication of nanomaterials for energy and environmental applications

3:10-3:40pm *Coffee Break*

Chairman: Prof Helen MENG

3:40-4:00pm **Prof. Anthony SO** Department of Systems Engineering and Engineering Management
A semidefinite programming approach to sensor network localization and molecular conformation

4:00-4:20pm **Prof. CHU Ming Chung** Department of Physics
Opening a door in elementary particle physics – the Daya Bay reactor neutrino experiment

4:20-4:40pm **Prof. HUANG Jianwei** Department of Information Engineering
Power control in wireless multi-carrier communication systems

4:40-5:00pm **Prof. WONG Hoi Ying** Department of Statistics
Analysis of callable bull/bear contracts

5:00-5:20pm **Prof. TSANG Hon Ki** Department of Electronic Engineering
Silicon photonics: recent advances and future prospects

5:20-5:30pm **Prizes presentation**

Message from Dean of Engineering and Dean of Science

May we extend a warm welcome to all the participants of the Joint Faculty Research Day especially to the distinguished guest speaker, Professor Yue On Ching, and our fellow colleagues to share with us your valuable insights and experiences on the latest research development in engineering and science disciplines.

The Joint Faculty Research Day aims to present new perspectives in engineering and science, and to promote and foster interaction and collaboration among faculty members. We are sure that today's forum is a good occasion for us all to establish and consolidate cross-disciplinary research, which will be vital for facing challenges over the next decade.

This year, a Student Posters Competition is also introduced to encourage students' participation and to promote excellence in research at post-graduate level. Research posters of short-listed students will be showcased and outstanding researches will be recognized and awarded the Best Student Poster Award.

Finally, we thank you for coming to the Joint Faculty Research Day. We hope you can take an active part in today event and we wish you a very enjoyable and fruitful day.

Dean of Engineering
Prof Peter Yum Tak Shing

Dean of Science
Prof Kwan Hoi Shan

Speaker Abstract

Innovation and Technology Development in Hong Kong

Prof. YUE On Ching
Science Advisor, Innovation and Technology Commission, HKSAR
onching@itc.gov.hk

ABSTRACT

Established in 2000, the Innovation and Technology Commission, in collaboration with other government departments, the industrial and commercial sectors, tertiary institutes and industry support organisations, strives to build a solid foundation for innovation and technology development. The Commission has been working to support applied research and development, foster technology ventures, provide funding schemes and technological infrastructure, and develop human capital. Prof OnChing Yue is the Science Advisor of the Commission and he will give an account of the measures provided by the Commission to support applied R&D.

BIOGRAPHY

Prof. OnChing Yue is the Science Advisor in the HKSAR Innovation and Technology Commission, providing assistance and advice to the Commissioner on technology development under the government's new strategic framework for innovation and technology.

Prof. Yue was born in Macao, grew up in Hong Kong and immigrated with his parents to the United States in 1963. He joined the Radio Research Lab at Bell Labs in 1977 after receiving his Ph.D. in Electrical and Computer Engineering from the University of California at San Diego. After spending 26 years at Bell Labs, he became a visiting professor in the Information Engineering Department at the Chinese University of Hong Kong in 2003. In September 2005, Prof. Yue took leave from CUHK and joined the Innovation and Technology Commission.

Before leaving Bell Labs, Prof. Yue was a department director in the Advanced Technologies division. His department was responsible for developing new algorithms and protocols for improving and predicting the performance and reliability of wireless networks.

Prof. Yue has over 20 journal publications and over 30 conference papers. Among his 18 patents, the one on mechanisms for guaranteeing Quality of Service (QoS) in Internet Protocol (IP) networks was named as one of 2003's top five patented new technologies by MIT Technology Review in 2004. His research interests include wireless access networks (3G, wireless LANs and PANs), security (DDoS, priority access and sensor networks), and application QoS (VoIP, TCP, streaming video and games).

My Story on Surface Plasmon Resonance Development

Prof. KONG Siu Kai
Department of Biochemistry, Faculty of Science
skkong@cuhk.edu.hk

ABSTRACT

The detection of biomolecular species such as pathogen antigens or disease markers from patient samples is an important area to improve the well-being of humankind. Until now, optical signal transduction techniques such as fluorescence and surface plasmon resonance (SPR) are playing major roles in detecting biomolecular interactions. For SPR, it is extremely sensitive to variations in optical properties at the interface between metal and dielectric layer. It can be used as refractive index probe to monitor a real-time interaction between an analyte in solution and its specific partner immobilized on the metal surface without the use of labels. In this 15-min presentation, I will review how a SPR biosensor was developed by using phase change through a joint force between science and engineering.

BIOGRAPHY

Prof. SK Kong received his PhD degree from CUHK in 1989 and joined the Department of Biochemistry, CUHK in 1991. He teaches immunology and analytical biochemistry. His main research focus involves cancer biochemistry, red blood cells differentiation and biosensor development.

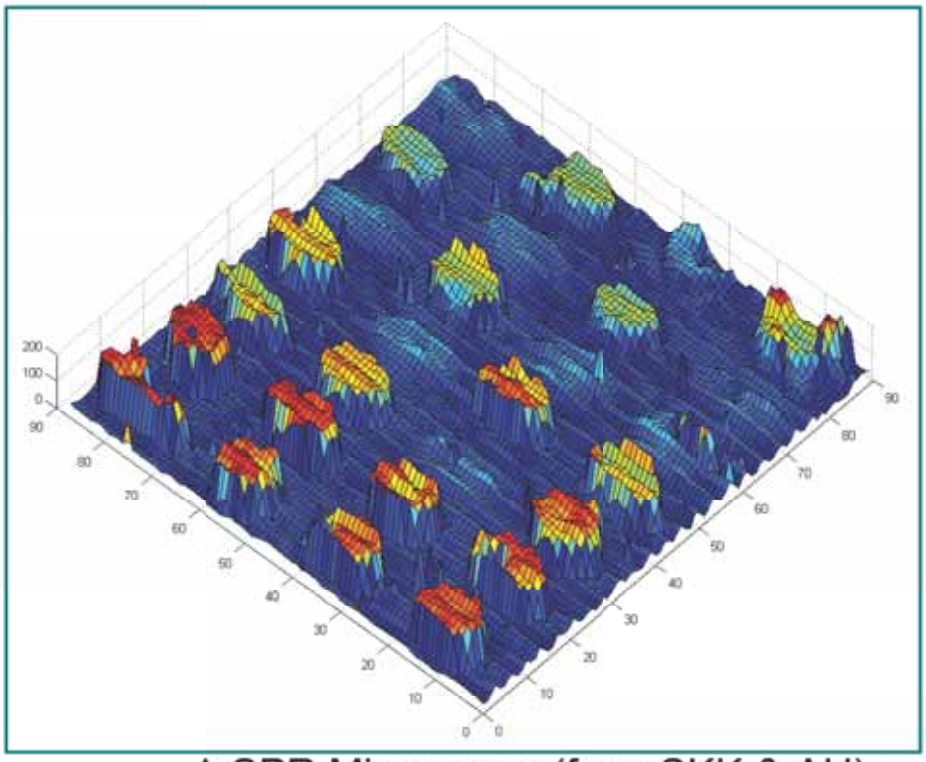

A SPR Micro-array (from SKK & AH)

Introduction to Precision Engineering

Prof. DU Ru Xu

Department of Mechanical and Automation Engineering, Faculty of Engineering

rdu@mae.cuhk.edu.hk

ABSTRACT

The mission of The Institute of Precision Engineering is to invent, develop and deploy new and able technologies in precision engineering for the well-being of Hong Kong, the nearby Pearl River Delta area, China and the world. The institute is directly under the university involving both the Faculty of Engineering and Faculty of Science. Currently, it has 34 team members, including 4 faculty members, 12 post doctoral researchers, 12 post graduate students, as well 5 technician / support staff. The annual budget is about HK$20 million. It also has a mirror operation in Shenzhen with 16 people. The current research projects include:

- Design and build mechanical watch movement;

- Energy efficient controllable mechanical metal forming press;

- Micro CNC gear hobbing machine;

- Micro Wire EDM machine;

- Micro assembly; and

- Solar air conditioning systems.

Details about the IPE could be found at http://www.ipe.cuhk.edu.hk

BIOGRAPHY

Professor Ruxu Du was born in China in 1955. He received his Master's degree in Automation from the South China University of Technology in 1983 and his PhD degree in Mechanical Engineering from the University of Michigan in 1989. He taught in the University of Windsor, in Windsor, Ontario (1991 – 1998) and University of Miami, in Coral Gables, Florida (1999 – 2001). Currently, he is a Professor in the Department of Mechanical and Automation Engineering at The Chinese University of Hong Kong (CUHK). He is also the Director of the Institute of Precision Engineering at the CUHK and the Director of the Center for Precision Engineering at the Chinese Academy of Sciences / CUHK Shenzhen Institute of Advanced Integration Technology in Shenzhen, China. Over the years, he has received over HK$93 million research grants. Currently, his research team consists of over 30 members in Hong Kong and over 18 members in Shenzhen, with an annual budget over HK$20 million.

His research interests include precision engineering, condition monitoring and fault diagnosis, manufacturing processes (metal forming, machining, plastic injection molding and etc.), as well as energy and materials. He has published over 180 papers in international journals and international conferences. He also has a number of patents and has won a number of awards. He is Associate Editor of three journals: International Journal of Control and Intelligent Systems, Computer-Aided Design and Applications, and Journal of Machine Design and Mechanisms, and is a member of editorial board of International Journal of Power and Energy Systems. He has been in the organizing committees of many international conferences and is the Co-Chair of the Second Asian International Symposium on Mechantronics (AISM 2006).

Protein Dynamics and Organelle Biogenesis in Plant Cells

Prof. JIANG Liwen
Department of Biology, Faculty of Science
ljiang@cuhk.edu.hk

ABSTRACT

Protein dynamics and organelle biogenesis are important topics in plant cell biology. One of the major research programs in my laboratory has been focused on the identification and molecular characterization of plant prevacuolar compartment (PVC) and endosomal compartment (EE) for their roles in mediating protein transportation in the secretory and endocytic pathways. In this talk, I will first present our approaches being used to study protein trafficking and organelle dynamics in plant cells. I will then use our studies on the identification and characterization of PVC and EE as examples to illustrate the efforts and limitations of our studies.

BIOGRAPHY

Dr. Jiang is currently a Professor at the Department of Biology of CUHK. He obtained his B.Sc. in 1984 from South China Agricultural University and M.Sc. in 1991 from University British Columbia. After obtaining his Ph.D. from Simon Fraser University in 1996, he then worked as a postdoctorial reseach associate for four years at the Institute of Biological Chemistry of Washington State University. Dr. Jiang became an Assistant Professor of CUHK in 2000 and Professor since 2007. Dr. Jiang's research interest has been focused on protein targeting and organelle biogenesis in plant cells, as well as their potential application in plant biotechnology.

Key Reference

1. Miao Y, KY Li, HY Li, XQ Yao and *Jiang L (2008) Vacuolar transport of aleurain-GFP and 2S albumin-GFP fusions is mediated by the same prevacuolar compartments in tobacco BY-2 and Arabidopsis suspension cultured cells. The Plan: Journal (submitted)
2. Lam SK, Cai Y, Hillmer S, Robinson DR, and *Jiang L (2008) SCAMPs highlight the developing cell plate during cytokinesis in tobacco BY-2 cells. Plant Physiology (in press)
3. Miao Y and *Jiang L (2007) Transient expression of fluorescent fusion proteins in protoplasts of suspension cultured cells. Nature Protocols 2: 2348-2353.
4. Lam SK, YC Tse, DG Robinson and *Jiang L (2007) Tracking down the elusive early endosome. Trends in Plant Science 12: 497-505.
5. Lam SK, CL Siu, S Hillmer, S Jang, G An, DG Robinson and Jiang L (2007) Rice SCAMP1 defines clathrin-coated, trans Golgi-located tubular vesicular structures as an early endosome in tobacco BY-2 cells. The Plant Cell 19: 296-319
6. Miao Y, PK Yan, H Kim, I Hwang and *Jiang L (2006) Localization of GFP fusions with the seven Arabidopsis vacuolar sorting receptors to prevacuolar compartments in tobacco BY-2 cells. Plant Physiology 142: 945-962
7. Tse YC, SW Lo, S Hillmer, P Dupree and *Jiang L (2006) Dynamic response of prevacuolar compartments to Brefeldin A in plant cells. Plant Physiology 142: 1442-1459
8. Miao Y, PK Yan, H Kim, I Hwang and *Jiang L (2006) Localization of GFP Fusions with the Seven Arabidopsis Vacuolar Sorting Receptors to Prevacuolar Compartments in Tobacco BY-2 Cells. Plant Physiology 142: 945-962
9. Mo BX, YC Tse and *Jiang L (2006) Plant prevacuolar/endosomal compartments. International Reviews of Cytology 253: 96-129
10. Tse YC, BX Mo, S Hillmer, M Zhao, DG Robinson, SW Lo and *Jiang L (2004) Identification of multivescular bodies as prevacuolar compartments in Nicotiana tabacum BY-2 cells. The Plant Cell 16: 672-693

Detection of Brain Activity using Wavelets in Functional MRI

Prof. Thierry BLU
Department of Electronic Engineering, Faculty of Engineering
tblu@ee.cuhk.edu.hk

ABSTRACT

Functional Magnetic Resonance Imaging (fMRI) provides "instantaneous" photographies of the brain activity. It is often used to localize which part of the brain is active when the patient is subjected to a specific stimulus (auditive, visual,...), or performs a given task (speak, move, ...). Compared to standard MRI settings which are unsuitable for functional studies due to their low acquisition rate, the fMRI modality provides functional informations, at the expense of a substantial noise increase though. The problem of localizing the activation based on a repetition of these informations (typically, in an on-off experiment) amounts to testing each voxel imaged for the active/non-active hypothesis.

However, given the very high noise level, spatial correlations of the activation patterns have to be taken into account. To this end, we present a new wavelet-based framework that provides an "integrated" approach: the data is processed in the wavelet domain (e.g., by thresholding wavelet coefficients), and a suitable statistical test procedure is done in the spatial domain. This method is based on conservative assumptions only and therefore it has a strong type-I error control.

The main contributions of our technique are demonstrated by experimental results. An implementation of our framework is readily available as a toolbox (WSPM) for SPM, the standard software for neuroimaging.

BIOGRAPHY

Professor Thierry Blu got his M.Sc. in Ecole Polytechnique (France) in 1986 and his M.Eng. and Ph.D in Telecom Paris (France) in 1988 and 1996 respectively. Before joining the Department of Electronic Engineering of the CUHK as a Professor in 2008, Professor Blu was a project leader and lecturer at the Swiss Federal Institute of Technology (EPFL) in Lausanne, Switzerland from 1998-2007. From 1988-1998, he had also worked as a Chief Telecommunication Engineer at France Telecom R&D.

Professor Blu was the recipient of two best paper awards from the IEEE Signal Processing Society (2003 and 2006). One of his papers on wavelet image denoising was cited in the "Reader's Choice" column of the IEEE Signal Processing Magazine (September 2007 and January 2008 issues). Patented aspects of his research related to the interpolation of "Finite Rate of Innovation" signals have also been transferred to Qualcomm Inc. (San Diego, CA) for applications to Ultra Wide Band communications. Between 2002 and 2006, Prof. Blu has been an Associate Editor of the IEEE Transactions on Image Processing and since 2006, of the IEEE Transactions on Signal Processing. He is currently an IEEE Senior Member and a member of the Technical Committee "Signal Processing Theory and Methods" of the IEEE Signal Processing Society. Professor Blu's research interests are in wavelets, multiresolution analysis, multirate filterbanks, interpolation, approximation and sampling theory, image denoising, psychoacoustics, optics, wave propagation. More generally, the interplay between the acquisition of physical data and their sampling, with a special focus on biomedical applications.

Fabrication of Nanomaterials for Energy and Environmental Applications

Prof. Jimmy YU

Department of Chemistry and Environmental Science Programme, Faculty of Science

jimyu@cuhk.edu.hk

ABSTRACT

Energy and environment are the biggest challenges of the 21st century. It is ironic that such big problems may be solved by something very small. Nanomaterials, with attractive chemical and physical properties, are being explored for their potential in energy and environmental applications. For example, when nanosized anatase TiO2 is illuminated by UV, it triggers an energetic response that can split water molecules to form hydrogen gas and oxidize pollutants to environmentally acceptable products. Pure titanium dioxide powders, however, have poor quantum efficiency and are difficult to recycle. The development of more effective and easily recyclable photocatalysts is therefore crucial. Several strategies for photocatalytic activity enhancement, including noble metal sensitization, non-metal doping, and the inclusion of mesopores have been developed. The preparation methods for enhanced TiO2-based photocatalysts as well as other semiconductor oxides and chalcogenides will be described. The uses of these nanomaterials will be discussed in this presentation.

BIOGRAPHY

Prof. Jimmy Chai-mei Yu received his Ph.D. degree in Environmental Analytical Chemistry from University of Idaho. He joined the Department of Chemistry in 1995 after teaching for over ten years in the United States. He is now Professor and Director of Studies of the Environmental Science Programme at CUHK. Prof. Yu's research interests focus on nanomaterials and their environmental applications. He has received prestigious research awards and holds several patents for his inventions.

Key Reference

1. J.G. Yu, J.C. Yu, W.K. Ho, L. Wu, X.C. Wang, J. Am. Chem. Soc. 126, 3422 (2004).
2. L.Z. Zhang, J.C. Yu, M.S. Mo, L. Wu, Q. Li, K.W. Kwong, J. Am. Chem. Soc. 126, 8116 (2004).
3. J.C. Yu, X.C. Wang, L. Wu, W.K. Ho, L.Z. Zhang, G.T. Zhou, Adv. Funct. Mater. 14, 1178 (2004).
4. X.C. Wang, J.C. Yu, Y.D. Hou, X.Z. Fu, Adv. Mater. 17, 99 (2005).
5. M.S. Mo, J.C. Yu, L.Z. Zhang, S.K.A. Li, Adv. Mater. 17, 756 (2005).
6. J.C. Yu, W.K. Ho, J.G. Yu, H.Y. Yip, P.K. Wong, J.C. Zhao, Environ. Sci. Technol. 39, 1175 (2005).
7. X.C. Wang, J.C. Yu, Y.L. Chen, L. Wu, X.Z. Fu, Environ. Sci. Technol. 40, 2369 (2006).
8. F.Q. Sun, J.C. Yu, Angew. Chem. Int. Ed. 46, 773 (2007).
9. X.L. Hu, J.C. Yu, J.M. Gong, Q. Li, G.S. Li, Adv. Mater. 19, 2324 (2007).
10. X.L. Hu, J.C. Yu, Adv. Funct. Mater. 18, 1 (2008).

A Semidefinite Programming Approach to Sensor Network Localization

Prof. Anthony SO

Department of Systems Engineering and Engineering Management, Faculty of Engineering

manchoso@se.cuhk.edu.hk

ABSTRACT

It is a trivial matter to see that given the coordinates of n points in R^k, the distance between any two points can be computed efficiently. However, the inverse problem --- given a subset of interpoint distances, find the coordinates of points (called a realization) in R^k (where k>=1 is fixed) that fit those distances --- turns out to be anything but trivial. In fact, this problem has been shown to be NP-hard for any fixed k>=1. Besides being a theoretical curiosity, this problem arises from many applications, e.g., surveying, satellite ranging, sensor network localization and molecular conformation, just to name a few. Thus, many heuristics have been proposed. However, they either do not have any theoretical guarantees, or they work only for some very restricted classes of instances.

Recently, Biswas and Ye (2004) have proposed a semidefinite programming (SDP) based model for the problem and have reported its superb experimental performance. Our work is motivated by the desire to explain this phenomenon in a rigorous manner. We show that the SDP model can be used to find a realization in the required dimension if the input instance satisfies certain uniqueness property. This uniqueness property has a straightforward geometric interpretation, and it allows us to identify a large class of efficiently realizable instances. Furthermore, it allows us to make some interesting connections with various notions in the rigidity theory of graphs. We then show how ideas from the theory of tensegrities can be used to enhance the SDP model, which in turn allows us to design efficient heuristics for many of the applications.

BIOGRAPHY

Professor Anthony Man-Cho So received his BSE degree in Computer Science from Princeton University in 2000 with minors in Applied and Computational Mathematics, Engineering and Management Systems, and German Language and Culture. He then received his MSc degree in Computer Science in 2002, and his PhD degree in Computer Science with a PhD minor in Mathematics in 2007, all from Stanford University. Professor So joined the Department of Systems Engineering and Engineering Management at the Chinese University of Hong Kong in 2007. His current research focuses on the interplay between optimization theory and various areas of algorithm design, such as computational geometry, stochastic optimization, combinatorial optimization, and algorithmic game theory.

Opening a Door in Elementary Particle Physics - the Daya Bay Reactor Neutrino Experiment

Prof. CHU Ming Chung
Department of Physics, Faculty of Science
mcchu@phy.cuhk.edu.hk

ABSTRACT

One of the most dramatic breakthroughs in physics recently is the discovery that neutrinos have mass, through the discovery of neutrino oscillation - a neutrino travelling in space transforms from one type to another. The fact that neutrinos are massive and oscillate has profound implications in particle physics, cosmology and astrophysics; it opens the door to physics beyond the Standard Model of Particle Physics, and it may hold the key to explaining why matter dominates anti-matter in the universe, a key condition for our existence. However, the value of a key parameter to describe neutrino oscillation, q13, remains unknown. The best approach for determining q13 is to measure the flux of antineutrinos from nuclear reactors at different locations, with the detectors installed underground to suppress the cosmogenic background. An international team of physicists has decided to mount such an experiment at the Daya Bay Nuclear Power Plant, and a group of local scientists has been actively involved from the very beginning. This project will help us to establish Hong Kong as a regional centre in fundamental physics research and build long-term collaboration with leading research institutes worldwide.

BIOGRAPHY

Prof. Chu Ming-chung obtained his BSc and PhD in Physics in 1983 and 1987 respectively, both from Caltech. In recent years, his research interest is in the areas of Astrophysics, Cosmology, and Particle Physics.

Power Control in Wireless Multi-carrier Communication Systems

Prof. HUANG Jianwei
Department of Information Engineering, Faculty of Engineering
jwhuang@ie.cuhk.edu.hk

ABSTRACT

Multi-carrier communication techniques have been successfully implemented in various wireless networks, and have become the core for 4G mobile communication systems. For example, Orthogonal Frequency-Division Multiplexing (OFDM) has been used in standards such as Wireless LAN (802.11 a/g), WiMAX (802.16), Digital audio/video broadcasting (DAB/DVB) and Ultra Wideband (UWB). The major benefits of using multi-carrier techniques include high spectrum efficiency and resistance against multi-path interferences.

In this talk, we consider the power control problem in wireless multi-carrier communication systems. We solve the problem using an Asynchronous Distributed Pricing (ADP) algorithm, which has a nice interpretation of distributed Pigovian taxation. We show the optimality and convergence of the ADP algorithm using supermodular game theory, which is a game with various nice features and wide applications in engineering and economics.

BIOGRAPHY

Professor Huang Jianwei is an Assistant Professor in the Department of Information Engineering at the Chinese University of Hong Kong. He received the M.S. and Ph.D. degrees in Electrical and Computer Engineering from Northwestern University (Evanston, IL, USA) in 2003 and 2005, respectively. From 2005 to 2007, He worked as a Postdoctoral Research Associate in the Department of Electrical Engineering at Princeton University (Princeton, NJ, USA). In 2004 and 2005, he worked in the Mathematics of Communication Networks Group at Motorola (Arlington Heights, IL, USA) both as a full time summer intern and a part time researcher. In 1999, he worked as a summer intern in the Department of Change Management at GKN Westland Aerospace (Cowes, Isle of Wight, UK). His main research interests lie in the area of modeling and performance analysis of communication networks, with specific areas including cognitive radio networks, wideband OFDM and CDMA systems, wireless medium access control, multimedia communications, network economics, and applications of optimization theory and game theory.

Professor Huang is an Associate Editor of (Elsevier) Journal of Computer & Electrical Engineering, the Lead Guest Editor of the IEEE Journal of Selected Areas in Communications special issue on "Game Theory in Communication Systems", the Lead Guest Editor of Journal of Advances in Multimedia special issue on "Collaboration and Optimization in Multimedia Communications", and a Guest Editor of Journal of Advances in Multimedia special issue on "Cross-layer Optimized Wireless Multimedia Communications". He will be the Technical Program Committee Co-Chair of the International Conference on Game Theory for Networks (GameNets'09), and is a TPC member for many conferences such as IEEE INFOCOM, GlobeCom, WCNC, ICCCN, CCNC, and CrownCom. Professor Huang is the recipient of a 2001 Walter P. Murphy Fellowship at Northwestern University and a 1999 Chinese National Excellent Student Award.

Analysis of Callable Bull / Bear Contracts

Prof. WONG Hoi Ying
Department of Statistics, Faculty of Science
hywong@sta.cuhk.edu.hk

ABSTRACT

Callable Bull / Bear Contract (CBBC) has grown substantially since it was introduced to the market by the Hong Kong Exchange and Clearing Limited (HKEx) on 12 June 2006. The average daily turnover has increased from below $100 million in the first 12 months after the launch of the market to about $1.4 billion in the first quarter of 2008. Meanwhile, the number of newly listed CBBCs has surged from 29 in the third quarter of 2006 to 323 in the first quarter of 2008. Thus, the pricing and hedging CBBC can be regarded as a billion dollar question nowadays. In fact, the CBBC first appears in Europe where it is called turbo warrant. In some European countries, buying and selling turbo warrants constitutes over 50% of all derivatives trading nowadays. CBBCs are special types of barrier options in which the rebate is calculated as another exotic option. HKEx describes that CBBC is less sensitive to the change in volatility of the underlying asset compared to derivatives warrants or standard option contracts. Hence, it is more suitable for betting the market direction without engaging too much in volatility risk. In this talk, I present the analysis of CBBC based on several market models for stock price dynamics. The most important message is that CBBC can be very sensitive to the volatility risk, which is in a sharp contrast to the message by HKEx, and the sensitivity depends on the model which is used to value the product. Finally, I will talk about possible engineering techniques that may be useful to build a pricing, hedging and risk management system for exotic derivatives, such as CBBC, and the corresponding challenges.

BIOGRAPHY

Dr. Wong, Hoi Ying received his PhD in Mathematics from Hong Kong University of Science and Technology in 2001. He started his academic career in the Chinese University of Hong Kong as an assistant lecturer, is now assistant professor of Department of Statistics, and will be advanced to associate professor on 1 August 2008. He also served as Director of MSc in Risk Management Science in 2004-2005, and is now serving as the Coordinator of a joint Risk Management programme between CUHK and Hong Kong Institute of Bankers. He has been consultant of commercial banks and Hong Kong Monetary Authority. His research interest includes derivatives pricing, financial risk management, financial econometrics, interest rate modeling and mathematical finance. His papers published in journals in the fields of finance, mathematics and operational research, such as Mathematical Finance, SIAM on Numerical Analysis, Journal of Complexity, Journal of Derivatives, Journal of Empirical Finance, Journal of Futures Markets, Quantitative Finance, IIE transactions, European Journal of Operational Research, etc.

Silicon Photonics: Recent Advances and Future Prospects

Prof. TSANG Hon Ki
Department of Electronic Engineering, Faculty of Engineering
hktsang@ee.cuhk.edu.hk

ABSTRACT

Silicon photonics is attracting increasing attention around the world because of its important potential applications. Apart from having established applications in optical telecommunications, silicon photonics offers the possibility of solving the heat and high power dissipation problems of electrical interconnects that limit the performance of high speed computers. The development of silicon based optical modulators, photodectors and other waveguide functional elements may eventually lead to the development of low-power dissipation, high-speed optical interconnects needed in future computers, as well as to the development of low cost optical chips for next-generation fiber-to-the-home networks. Another emerging area for silicon photonics is in optical sensing. Unlike silica glass, silicon has low optical loss at mid-wave infrared wavelengths, thus opening the possibility for spectroscopic applications of silicon chips at the mid-wave infrared wavelengths (3-5 microns) which correspond to the fundamental rotational and vibrational resonances of many different species of gases. This talk will review recent advances in silicon photonics at CUHK including work on nonlinear silicon photonics, the silicon Raman amplifier and laser, the use of ion implantation to enhance the performance on nonlinear devices, and ion implanted waveguides for silicon based photodetectors at the wavelengths used in optical communications. The narrow linewidths of the silicon Raman laser will be discussed in the context of possible applications in wavelength modulation spectroscopy applications. The prospects for integrated silicon chips for gas sensing applications at mid-wave infrared wavelengths will be discussed.

BIOGRAPHY

Professor Tsang Hon Ki received the B.A. (Hons) degree in 1987 in Engineering (Electrical and Information Sciences), and the Ph.D. and M.A. degrees in 1991, all from the University of Cambridge. He was a research visitor Bell Communications Research Inc. (Bellcore, USA) in 1990 (and again in 1993) and a postdoctoral fellow at the University of Bath (UK) between 1991-93. He joined the Department of Electronic Engineering at The Chinese University of Hong Kong in 1993. In 2001-03 he took no-pay leave from CUHK to manage R&D on silicon photonics at Bookham Technology plc. He has published over 200 papers in journals or conference proceedings and was a former chair of the IEEE LEOS Hong Kong Chapter. He currently serves as an associate editor of the IEEE LEOS Newsletter, and on the technical program committees of various IEEE and OSA conferences.

Student Posters

XU Lin **Supervisor: Prof. TSANG Hon Ki**
Department of Electronic Engineering, Faculty of Engineering

Project Title "Colorless WDM-PON optical network unit (ONU) based on integrated non-reciprocal traveling-wave optical modulator and optical loop mirror"

Wavelength Division Multiplexing Passive Optical Networks

Lin Xu and H.K. Tsang
lxu@ee.cuhk.edu.hk
Department of Electronic Engineering, The Chinese University of Hong Kong, Shatin, Hong Kong

BACKGROUND

WDM-PON is a next generation technology which uses multiple optical wavelengths to increase the upstream and/or downstream bandwidth available to end users in the access network. Although DWDM technology is mature in long haul communications, it has not yet been applied to optical access networks because of their high costs.

CHALLENGES

Reduction of costs in WDM PON will be the key challenge for their deployment

WDM-PON scheme with colorless ONU :
A cost-effective solution would ideally employ the same components in each customer transceiver that should thus be independent of the wavelength assigned by the network

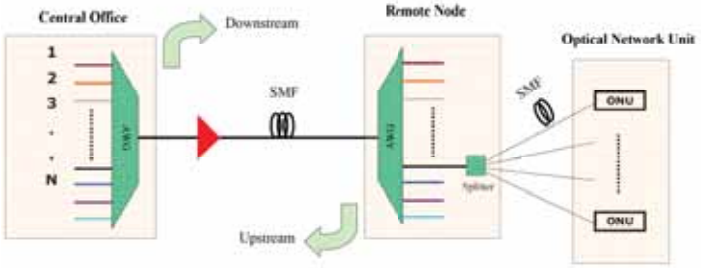

Proposed Scheme

Colorless WDM-PON ONU based on integrated non-reciprocal optical phase modulator and optical loop mirror

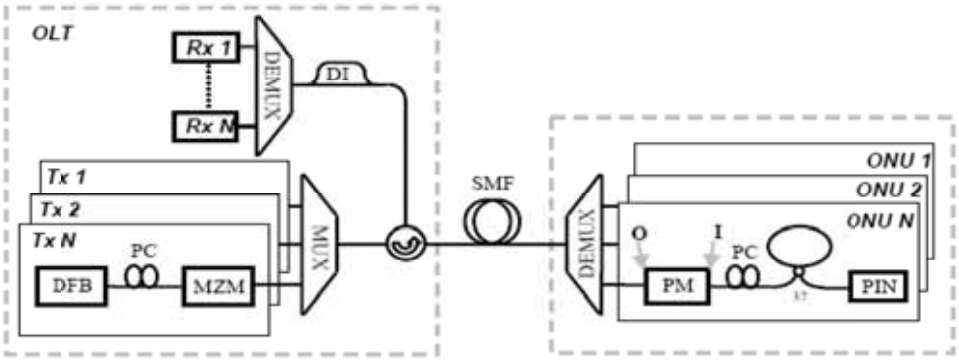

Fig. PM: phase modulator O: output port of PM I: input port of PM SMF: single mode fiber PC: polarization controller (not needed in integrated version) OLT: optical line terminal ONU: optical network unit

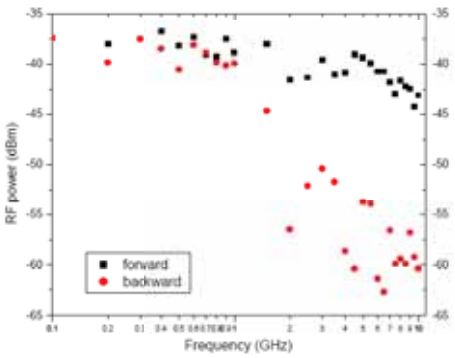

Fig. Frequency response of phase modulator

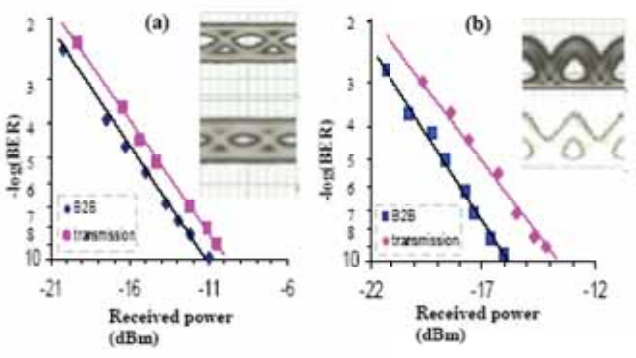

Fig. BER measurements for (a) downstream NRZ and (b) upstream DPSK signal. The upper and lower inset pictures are eyediagrams for back-to-back and after transmission

SUMMARY

A novel remodulation scheme using the non-reciprocity of optical phase modulator and a linear optical loop mirror was evaluated

Traveling wave modulator is transparent to downstream light and effective modulation to upstream light

The technique has a simple and cost effective ONU structure, which has potential for low cost silicon integration

ZHENG Liu **Supervisor: Prof. Jeffrey XU Yu**
Department of Systems Engineering and Engineering Management, Faculty of Engineering

Student Poster

Project Title "Shape Anomaly Detection: A Probabilistic Approach Using Hidden Markov Models"

Shape Anomaly Detection: A Probabilistic Approach Using Hidden Markov Models

Zheng Liu
CUHK
Jeffrey Xu Yu
CUHK
Lei Chen
HKUST
Di Wu
CUHK

Contributions

- We propose a new framework based on the segmental HMM to detect the shape anomalies under a scaling, translation and rotation invariant manner.
- We propose an efficient detection algorithm based on dynamic programming.
- We demonstrate that our algorithm can effectively detect the shape anomalies from a large collection of shapes.

Acknowledgment

This work was supported by a grant of RGC, Hong Kong SAR, China (No. 418206).

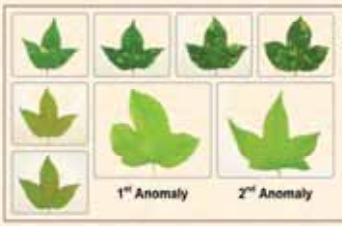

Shape Anomaly Detection is Useful!

- **An Example in Biology**
  - The left figure shows the 1st and 2nd anomalies in the shape collection of liquidambar formosana leaves.
- **Other Areas**
  - Many applications in medicine, genetics, archaeology, geography, agriculture and etc.

Background

- **Shape Representation**
  - The shapes are stored as time series of distances between the centroid and the boundary points.
- **Segmental Hidden Markov Model**
  - A segmental HMM with K states is described by the transition matrix, as well as a probability distribution over the duration for each state.

A Naïve Solution (NHMM)

- **A Segmental HMM for Time Series**
  - The transition matrix is left-to-right.
  - The initial state distribution: [1, 0, …, 0]
- **Alignment and Segmentation**
  - The training samples must be aligned first.
  - Each aligned time series is segmented into K pieces to construct a K-state segmental HMM.
- **Detection with the Segmental HMM**
  - The segmental HMM is trained with the classical EM algorithm.
  - $\hat{P}_t^{(1)} = \max_s \{p(s \mid y_1, y_2, \ldots, y_t) \mid s = s_1, s_2, \ldots, s_t; s_t = i\}$
  - $\hat{P}_t^{(i)} = \max_{d_i}(\max_j \hat{P}_t^{(i-d_i)} a_{ji}) p(d_i) p(y_1, y_2, \ldots, y_t \mid \theta_i)$
  - A viterbi-like algorithm based on dynamic programming.

Our Proposed Solution (GHMM)

- **A Generalized HMM for Shape Time Series**
  - To achieve rotation invariance, alignment avoidance and better quality.
  - We allow transition from state K to state 1.
  - The initial state distribution: [1/K, 1/K, …, 1/K]
- **Optimal Time Series Segmentation**
  - Shape time series are segmented by minimizing the variance of the approximation errors.
- **Detection with the Generalized HMM**
  - The new detection algorithm is based on dynamic programming.
  - A priority queue is used to further improve the speed.

Results on Two Real Data Sets

- Shapes in the 1st row are five examples from the training samples.
- Shapes in the 2nd, 3rd and 4th row are the top five anomalies detected by different algorithms.

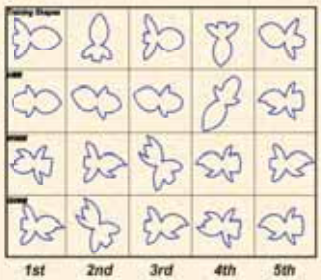

The Arrow Data Set

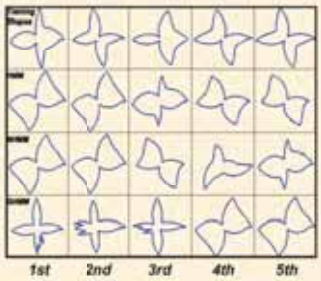

The Diatom Data Set

Comparison with the Deterministic Approach

- The synthetic data set consists of five kinds of shapes as show in the 1st row, which are from the mixed bag data set.
- The deterministic algorithm WKX detects the anomalies based on the nearest neighbor distance. The shape with the maximum nearest neighbor distance is considered as the first anomaly.

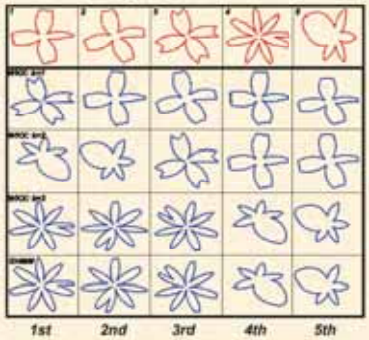

- The WKX algorithm has a parameter k which is the total number of anomalies in the data set. It works well only when k is correct.
- Our algorithm GHMM can detect anomalies successfully with unsupervised learning for fairness.

Efficiency of the Proposed Solution

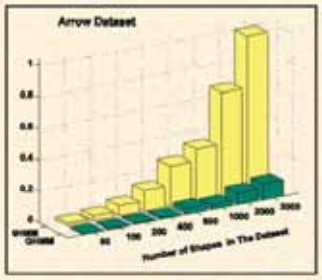

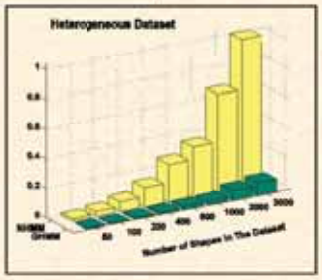

PANG Wai Man **Supervisor: Prof. Pheng Ann HENG & Prof. Tien Tsin WONG**

Department of Computer Science and Engineering, Faculty of Engineering

Project Title "Tileable BTF"

Tileable BTF

M. K. Leung, W. M. Pang, C. W. Fu, T. T. Wong and P. A. Heng,
Department of Computer Science and Engineering, The Chinese University of Hong Kong

Overview & Goals

We propose a modular framework to efficiently apply the *Bidirectional Texture Functions (BTF)*, a kind of high dimensional texture with variable lighting and viewing directions, onto 3D object surfaces. Previous approaches *spent hours to synthesize BTF directly* on the surfaces space. Moreover, the synthesized result cannot be reused for different geometric objects, and the synthesis has to be repeated on same object for different BTF dataset.

Our goal is to *decouple the BTF synthesis from the surface geometry*, so that changing the surface geometry does not require re-synthesizing the BTF. To achieve this, we introduce the tile space. Synthesis only occurs when creating the BTF tiles, while the BTF tile-sets are *reusable* to any objects. A novel tile synthesis method is also proposed, which is more suitable for high dimensionality and enormous storage nature of the BTF data.

Bunny dressed with REACTDIFFUSE BTF

Real BTF datasets used

Synthetic BTF datasets used

Overview of Framework

Approach

Starting from the BTF raw data, we compress the data using *doubly projected spherical harmonics* to make it compact enough for the GPU. Then, BTF tile set is build based on the compressed data. A tile set contains color edged synthesized tiles, in which edge with same color can be connected seamlessly.

Our proposed tile synthesis approach is based on the standard quilting tile synthesis method. But we consists of four sub-steps: corner sampling, edge synthesis, frame construction, and interior area synthesis. This significantly reduce the length of cut path in each quilting step to improve the quality of seamless synthesis.

In order to reduce the distortion, object surfaces are reparameterized using polycube map approach. Then, the tiles are placed on the surface of object with all shared edges having matched color as criteria.

The rendering of local illumination requires a TBN transformation to convert between the coordinate system of world and the BTF local system.

$$\begin{pmatrix} t_x \\ t_y \\ t_z \end{pmatrix} = \begin{pmatrix} T_x & T_y & T_z \\ B_x & B_y & B_z \\ N_x & N_y & N_z \end{pmatrix} \begin{pmatrix} w_x \\ w_y \\ w_z \end{pmatrix}$$

A TBN matrix transformation is applied to the world coordinate of light and camera directions.

Result

We had applied our method on various 3D objects and both real and synthetic BTF datasets. One can observe that there is no obvious seams after the BTF is tiled on the objects.

Apart from local illumination with single light source, we render our results with environment lighting using importance sampling approach. The rendered results show our proposed method can effectively produce seamless BTF synthesis on object surfaces and render in real-time. While the new approach allows *appearance-geometry decoupling* and capable to *Instant-redressing* of BTF.

The Tiling Process

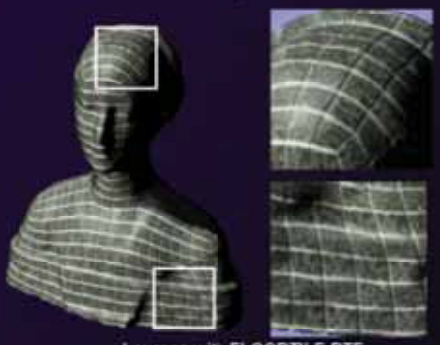

Laurana with FLOORTILE BTF

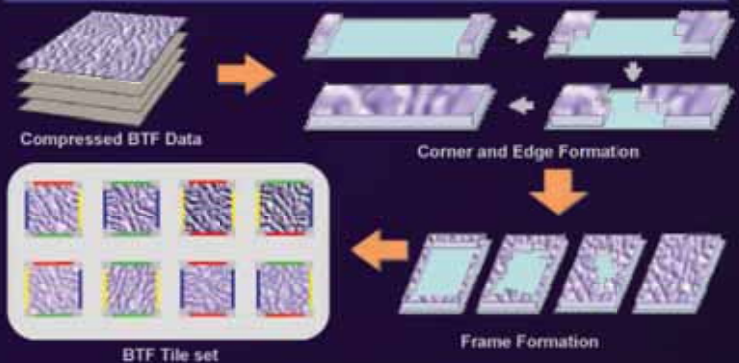

Proposed BTF Tiles Synthesis

Render with Environment Lighting

Associated Publication

M. K. Leung, W. M. Pang, C. W. Fu, T. T. Wong and P. A. Heng,
IEEE Transactions on Visualization and Computer Graphics, vol. 13 no. 5, pp. 953-965, September/October, 2007.

TAM Lam Chi **Supervisor: Prof. DU Ru Xu**
Department of Mechanical and Automation Engineering,
Faculty of Engineering

Student Poster

Project Title "Virtual Library of Mechanical Watch Movements"

Virtual Library of Mechanical Watch Movements

The Virtual Library of Mechanical Watch Movements is divided into three sections. Currently, it consists of nine records organized as follows:

The Mechanical Clock Escapements

- The Graham Escapement

The Mechanical Watch Escapements

- The English Lever Escapement
- The Swiss Lever Escapement
- The Daniels Co-Axial Double-Wheel Escapement
- The Spring Detent Escapement
- The Cylinder Escapement
- The Verge Escapement

The Accessory Mechanisms

- The Automatic Winding System
- The Moon Phase Mechanism

For each record in the Virtual Library, detailed background information, 3D CAD models, and computer animation video clips are offered. The Virtual Library is accessible on the internet at:

http://www.ipe.cuhk.edu.hk/projects/10_library.html

CHENG Lap Kei **Supervisor: Prof. Chester SHU**
Department of Electronic Engineering, Faculty of Engineering

Project Title "Wavelength Transparent SBS Slow Light Using XGM-Wavelength Converter and Brillouin Fiber Laser"

Wavelength Transparent SBS Slow Light Using XGM-Wavelength Converter and Brillouin Fiber Laser

Alan Cheng, Mable P. Fok, and Chester Shu
Department of Electronic Engineering and Center for Advanced Research in Photonics, The Chinese University of Hong Kong, Shatin, N.T., Hong Kong

ABSTRACT: We demonstrate a wavelength transparent stimulated Brillouin scattering (SBS) slow light architecture using a cross gain modulation (XGM) wavelength converter and a Brillouin fiber laser. The input signal is wavelength converted to become automatically aligned with the resonance induced by SBS. The maximum delay achieved is 26 ns with a 30 dB Brillouin gain. The operating wavelength window is over 40-nm and the induced delay variation is smaller than 0.2 ns.

Introduction

- Applications of slow light
  - Optical buffering
  - Tunable optical delay line
  - Enhancement of interaction time in optical fiber
- Characteristics of slow light via stimulated Brillouin scattering
  - Continuously tunable delay
  - Fiber-optic approach
  - Requirement of wavelength alignment between pump and signal
- Advantages of our approach
  - Auto-alignment between pump and signal wavelengths
  - Wavelength transparent operation

Experimental setup

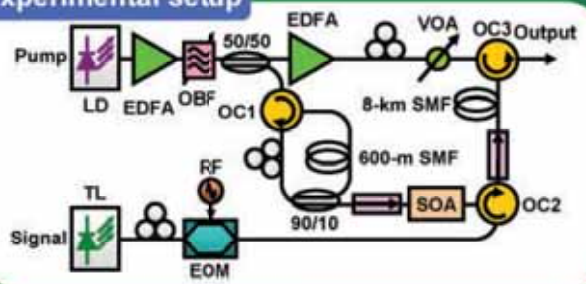

Principle and Schematic illustration

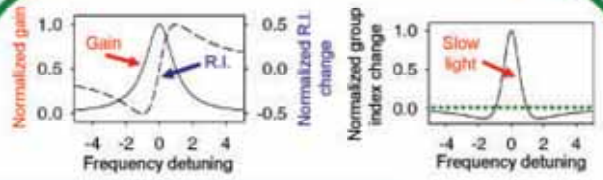

- By Kramer-Kronig relations
  - → R.I. change is associated with frequency dependent gain
  - → Rapid change of R.I. is obtained at the gain peak frequency
  - → Group velocity change is resulted from the rapid change of R.I.

$$n_g = n_p + \omega \frac{dn_p}{d\omega}$$

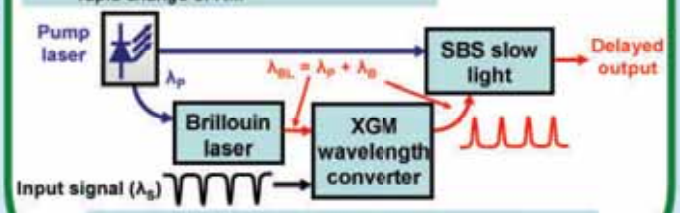

- λ_{BL} and λ_p differ by Stokes wavelength shift (λ_B)
- Input signal (λ_s) is converted to λ_{BL}
- Slow light is achieved at λ_{BL}

Measurement results

Characteristics of Brillouin fiber laser

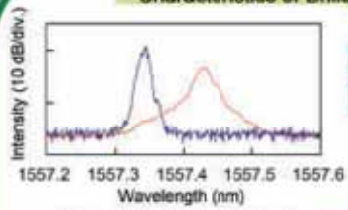

- Pump power: 15 dBm
- Brillouin shift: 10.83 GHz (~0.088 nm)

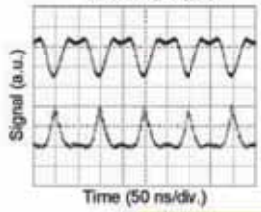

- Input: inverted
- Repetition rate: 10 MHz
- Inverted pulse width: 30 ns

- By XGM, the converted output becomes non-inverted

Continuously tunable delay

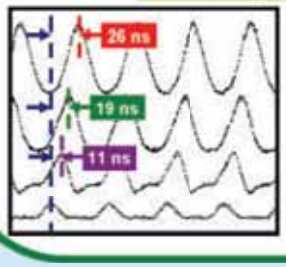

- Continuously tunable delay up to 26 ns with different Brillouin gain

Gain	Delay
10 dB	11 ns
20 dB	19 ns
30 dB	26 ns

Measurement results

Wavelength transparent characteristics

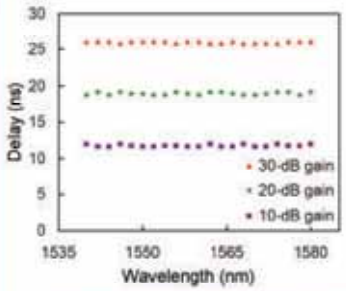

Output pulse profiles at 30 dB SBS gain

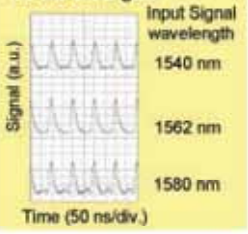

- SBS slow light applicable to different input signal wavelengths without changing the pump wavelength
- The delay variation is less than 0.2 ns over 40-nm wavelength tuning range

Conclusion

We demonstrate a wavelength transparent SBS slow light scheme using a XGM wavelength converter and a Brillouin fiber laser. The input signal is converted and aligned to the SBS induced resonance regardless of its original wavelength. Continuously tunable delay up to 26 ns has been achieved with 30-ns input pulses. The wavelength transparent operation offers a practical means to delay signals in optical communication networks.

KAN Wai Chi **Supervisor: Prof. Emma Macpherson**
Department of Electronic Engineering, Faculty of Engineering

Project Title "Application of Terahertz Imaging to Osteoarthritis"

Student Poster

Application of Terahertz Imaging to Osteoarthritis

Kanis W.C. Kan[1], Wing-Sze Lee[2], W H Cheung[2], Emma Pickwell-MacPherson[1]

[1]Department of Electronic Engineering, The Chinese University of Hong Kong.
[2]Department of Orthopaedics & Traumatology, The Chinese University of Hong Kong.

Introduction - **Osteoarthritis (OA) is the most common form of arthritis and is caused by the breakdown of cartilage. The loss of cartilage causes friction between bones and results in inflammation, swelling and pain at the joint. Early diagnosis of OA can help to prevent further deterioration. X-ray imaging is the current clinical technique used to diagnosis OA and is used to track the status of OA over time. However, it is unable to detect changes during the early stage. Hence, a new noninvasive imaging technique is in pressing need for early diagnosis as well as a non-ionizing approach for monitoring the disease situation.**

Terahertz pulsed imaging (TPI) is a novel non-ionizing imaging modality. Several special features of TPI give it the potential to be suitable for a variety of medical applications [1]. One of these is its ability to reveal the depth information of some biological samples, thus, in this study, we investigated the feasibility of TPI as a diagnosis tool for OA. Here, we demonstrate how to process the THz data in order to determine and quantify symptoms of OA.

OA Samples

Figure 1: Photograph of rabbit left knee joint. Cartilage covered on the surface of femoral condyle. With thanks to W. Lee from the Dept. of Orthopaedics & Traumatology for Figures 1-3.

Figure 2: *Photograph of rabbit femoral condyles (sample IM66) with OA symptom.*

Figure 3: *Histology of IM66 showing the cartilage area in light pink and the subchondral bone in dark pink under the blue line.*

Formalin fixed femoral knee joints with OA are harvested from white female rabbits were used as samples for study. The medial side of femoral condyle often suffers seriously on OA symptom. The histology collected from the area with OA shown that cartilage gets thinner and is degenerated.

Data Processing

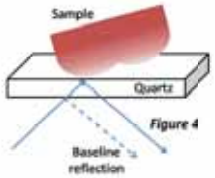

Figure 4

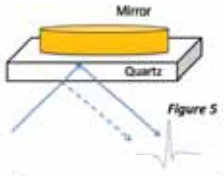

Figure 5

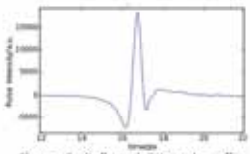

Figure 6: *Reflected THz pulse off a mirror.*

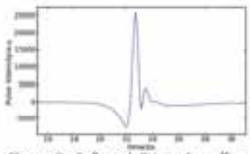

Figure 7: *Reflected THz pulse off a mirror with a new THz emitter. Note the additional secondary peak.*

$$FFT(\text{Impulse Function}) = FFT(\text{Filter}) \times \frac{FFT(\text{Sample} - \text{Baseline})}{FFT(\text{Reference} - \text{Baseline})}$$

[Equation 1]

The shape of the THz pulse generated by the system is illustrated in Fig.6 which was obtained by reflection off a mirror. The shape of the pulse is dependent on the terahertz emitter. Therefore, the THz pulse changed when a new emitter is used as shown on Fig. 7. Data processing is performed to remove system variability by deconvolved the raw data with Equation 1.

Results

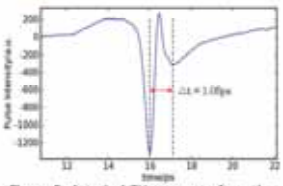

Figure 8: *A typical THz response from the OA sample IM51 (raw data).*

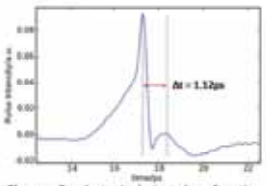

Figure 9: *A typical impulse function (processed data) from the OA sample IM51.*

Two peaks are found in the processed waveform of sample IM51. The first peak is the reflection of THz light from the quartz/sample interface and the second peak is the reflection within sample caused by change of refractive index. In this case, the optical delay between peaks is proportional to the thickness of the particular tissue inside the sample.

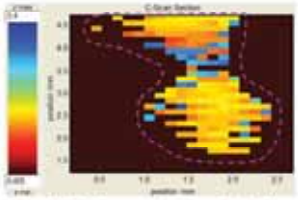

Figure 10: Color map of the optical delay between the two peaks in processed data set of IM51.

Sample	IM51		IM66	
	Mean optical delay	S.D.	Mean optical delay	S.D.
Raw	1.06	0.05	0.83	0.06
Process1	0.96	0.08	1.11	0.11

Table 1: The mean and standard deviation of optical delay.

The optical delays of each pixel within the area of interest were calculated and plotted in Fig. 10. The blue pixels correspond to areas where the tissue is thickest (optical delay is greatest) and the redder pixels correspond to where the tissue is thinnest.

Conclusions

In summary, we have shown how terahertz image data can be processed to extract features of interest, and that careful processing of the data enables consistent comparisons to be made without loss of detail. Furthermore, we have demonstrated that terahertz pulsed imaging is able to give a quantitative measure of features due to osteoarthritis - the optical delay between peaks on the processed waveform is correlated to the thickness of sample tissue.

Reference

[1] V. P. Wallace, P. F.Taday, A. J. Fitzgerald, R. M. Woodward, J.Cluff, and D. D.Arnone, "Terahertz pulsed imaging and spectroscopy for biomedical and pharmaceutical applications", *Faraday Discuss., 126, in press (2004)*

Joint Faculty Research Day 2008

CHEUNG Yang **Supervisor: Prof. Dah-ming CHIU**

Department of Information Engineering, Faculty of Engineering

Project Title "Can Bilateral ISP Peering Lead to Network-wide Cooperative Settlement"

Can Bilateral ISP Peering Lead to Network-wide Cooperative Settlement

Abstract

The Internet includes thousand of Internet service providers (ISPs) which are interconnected to provide connectivity and service for end-users. Traditionally, the settlement between the ISPs are determined based on bilateral agreements that are resultant from pair-wise negotiation. Although this settlement mechanism is intuitive and easy to implement, it does not encourage network-wide cooperation, as the bilateral charges typically do not lead to a fair division of revenue among All ISPs that are involved in carrying the same flows of traffic. This problem is getting more severe with various emerging new Internet business models.

We try to determine the existence and achievability of bilateral prices that can achieve fair revenue division among ISPs. In particular, we use Shapley value as the basis for deriving fair prices. Under a qute general topology and traffic model, we find that there exists prices that make the revenue Division under bilateral settlement equal to that calculated under Shapley value. The corresponding "Fair price" exhibits several Nice and desirable characteristics. Moreover, it can be approximated reasonably well by the ISPs with limited local Information in today's Internet. This represents one of the first steps of building a future netwcrk with a better economic-technological foundation.

Models

Topological Model

- Uses AS-level hierarchical model to represent current tier-based Internet;
- Considers:
  - ***T*** tiers (illustrated as horizental levels),
  - ***N*** ISP nodes (circles),
  - arbitrary users(squaress) subscribed to bottom tier ISPs;
- Three connection types:
  - transit links (black),
  - peering links(red), and
  - multi-homing links(blue)
- Define topology ***G*** = (***T,N, p, d***), where ***p*** is the peering probability, ***d*** is the multi-homing factor.

Traffic Model

- Uses ***α*** to denote the probability of traffic going local.
- ***α*** is a parameter to determine the distribution of traffic's travel distance.

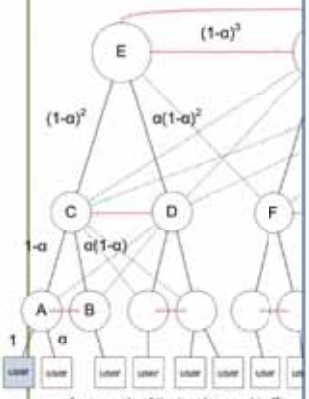

An example of the topology and traffic model

Settlements

Bilateral Settlement

- The settlement used in the current Internet;
- The charging between two ISPs is determined by mutual agreements;
- We consider a per-traffic tier-based charging scheme;
- A charge P_t is paid by the ISP subscriber to the ISP provider at tier t per unit traffic regardless of traffic direction;
- A fixed revenue obtained from all users is P_u.

$$\gamma_{u,t}(P) = \begin{cases} 2P_t, & \text{for local traffic,} \\ P_t, & \text{for peering traffic,} \\ P_t - P_{t-1}, & \text{for upstream traffic,} \end{cases}$$

for $t \in \{1,\ldots,T-1\}$, and

$$\gamma_{u,T}(P) = \begin{cases} -P_{T-1}, & \text{for upstream traffic,} \\ 0, & \text{for local peering traffic,} \end{cases}$$

where $P = (P_t, \forall\, t \in \{1,\ldots,T-1\})$.

Bilateral settlement pricing function

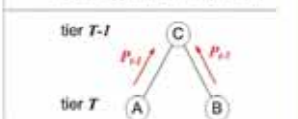

An example of Bilateral settlement considering a traffic from A to B

Shapley Settlement

- The settlement mechanism that divides the revenue among ISPs according to Shapley value;
- Shapley value provides a unique fair allocation of benefits obtained from a coalition among all participating players.
- Shapley value satisfies four axioms:
  - **Efficiency:** players distribute among themselves the resource available to grand coalition,
  - **Symmetry:** if two players are symmetric, their payoffs are the same,
  - **Dummy:** dummy player receive no payoff,
  - **Additivity:** the Shapley value of a combined game is equal to the Shapley value of the separated games.
- The total revenue obtain by users P_u are redistributed to each ISP according to its

$$\varsigma_n(b) = \frac{1}{|\mathcal{N}|!} \sum_{\pi \in \mathcal{N}} [v(\mathcal{S} \cup \{n\}, a, b] - v(\mathcal{S}, a, b)]$$

Shapley value function

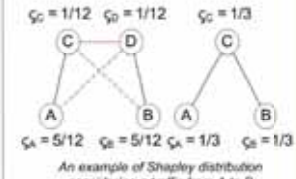

An example of Shapley distribution considering a traffic from A to B

Fair Price Achievement and its Properties

The Fair Price

We calculate the traffic-based price for each tier such that bilateral settlement could produce the same revenue distribution as Shapley settlement. We define the set of corresponding prices P^* as the fair price:

$$P_u \sum_{n \in N_t} \sum_{(a,b) \in \mathbf{B}} \mathbb{P}(a,b)\varsigma_n(a,b) = \sum_{n \in N_t} \sum_{(a,b) \in \mathbf{B}} \mathbb{P}(a,b)\gamma_{u,t}(P^*) + P_u \times 1_{\{t=T\}}, \forall\, t \in \{1,\ldots,T\}$$

We found that the fair price P^* in hierarchical topology G is having the following relationship:

$$2(1-\alpha\rho_{t+1})P_t^* = P_u\Big\{\sum_{(a,b)\in\mathbf{B}} \mathbb{P}(a,b) \sum_{n \in N_t} \varsigma_n(a,b) + 2(1-\alpha)(1-\alpha\rho_t)P_{t-1}^*\Big\}$$

The fair price at tier t is to find the per-traffic price that accounts the contribution of tier t, plus the price that contains the contribution of the upper tiers so that the upper tiers can achieve Shapley settlement by charging tier t ISPs P^*_{t-1}.

Properties of the Fair Price

- Implementing fair price among ISPs help converging the current bilateral settlement to Shapley value, which provide several nice fairness grounds;
- The fair price is reasonable when we look into the its sensitivity of varies parameters;

Sensitivity to traffic pattern *α*

- The fair price is decreasing in $\alpha \in (0,1]$;
- The traffic is more likely to be handled by tiers that lower tiers when ***α*** increases;
- ISPs at higher tiers have less contribution, hence they needed to charge less;
- This setting can better reveal the actual cost needed to transport a traffic;
- This setting also advocates short traffic routes.

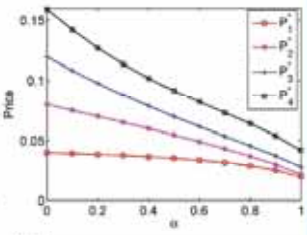

Sensitivity to peering probability *p*

- The fair price is decreasing in $\rho_t, t \in [1,\ldots,T-1]$
- More traffic passes through peering links without using upstream connections when ***p*** increases.
- Hence lower tiers pay less to upstream ISPs;
- Figure shows fair prices below tier3 decreases;
- Fair price of tier2 increases as it losos relatively cheap short-distance traffic. The actual revenue, however, has decreased.
- This setting advocates tiers to establish peering links.

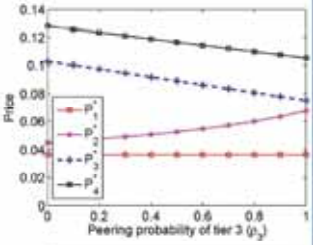

Sensitivity to multi-homing factor *d*

- The fair price of an ISP increases with multi-homing factor ***d*** if the ISP is a vital node for connectivity;
- Shapley value in this setting values connectivity more than redundancy;
- When d -> infinity, fair price -> 0, as contribution of each ISP along the path is virtually zero;
- This setting advocates ISPs to expend their connectivity to untouched destinations.

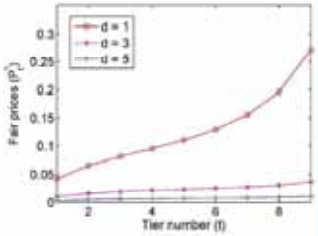

Distributed and Local Approximation

- Shapley value requires centralized calculations with complete information on the topology and traffic patterns of each ISP;
- The approximation is based on two observations:
  1. Shapley value can be approximated by the degree of importance,
  2. A reasonable anticipation of the peering parameter is sufficient to produce a close fair price.
- The approximation reduces the information required to local information:
  1. ISP's own traffic patterns,
  2. ISP's own peering statistics, and
  3. The importance of the ISP in its tier.
- Random case simulation on the right shows close differences between the centralized and the approximated calculation.

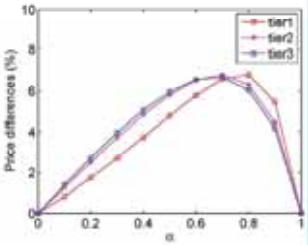

LAM Hiu Man **Supervisor: Prof. YAM Yeung**
Department of Mechanical and Automation Engineering,
Faculty of Engineering

Project Title "A Stroke Analysis Technique for A Chinese-styled Art Robot"

Student Poster

Department of Mechanical and Automation Engineering
The Chinese University of Hong Kong

A STROKE ANALYSIS TECHNIQUE FOR A CHINESE-STYLED ART ROBOT

Josh H.M. Lam

— an Engineering approach to study Chinese paintings and calligraphies

■ Drawing Platform

- High precision, 5 DOFs (x, y, z, z-rotation, pitch) manipulator

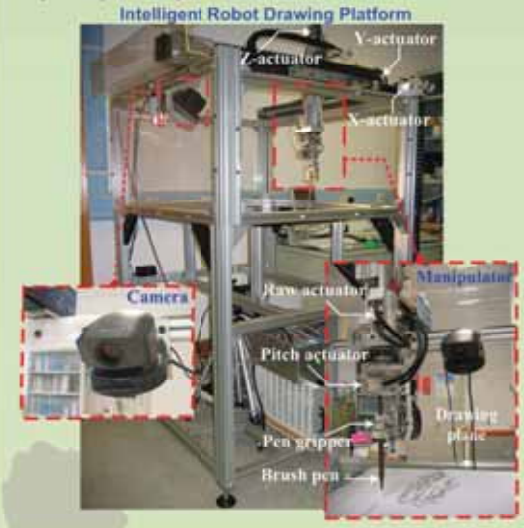

■ Previous Work

- Full Stroke Execution
  - Bézier curve representaion
  - GA-based stroke trajectory generation

- Experimental Acquisition of Brush Footprints
  - Setup with glass plate and video camera
  - Instantaneous footprint capturing and indexing for modeling and simulation

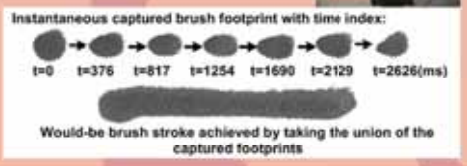

■ Recent Work: Stroke Analysis

- Accurate branches matching in intersection regions
- Effectively reduce computational time
- Generate smooth medial axis for stroke execution

- Triangular mesh approximation (Delaunay Triangulation, triangle filtering and replacement)
- Internal Edges Refinement based on smoothed local symmetry
- Medial axis interpolation using Bezier curve

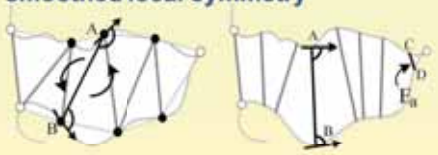

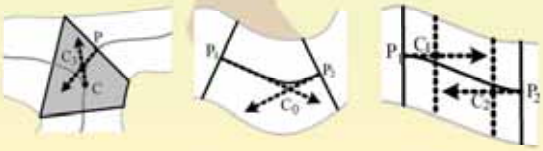

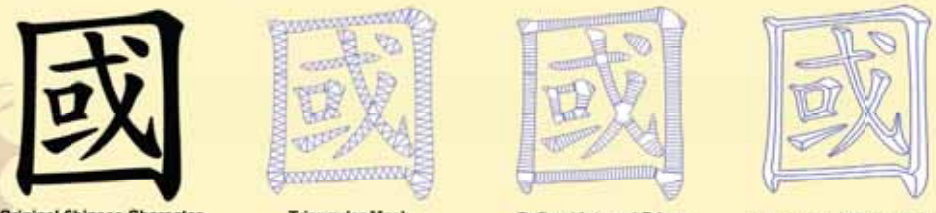

http://www.mae.cuhk.edu.hk/~icsl
Intelligent Control System Laboratory

PAN Yunpeng **Supervisor: Prof. Jun WANG**
Department of Mechanical and Automation Engineering,
Faculty of Engineering

Project Title "Robust Model Predictive Control Using a Discrete-Time Recurrent Neural Network"

Robust Model Predictive Control Using a Discrete-Time Recurrent Neural Network

Yunpeng Pan and Jun Wang
Department of Mechanical and Automation Engineering
The Chinese University of Hong Kong, Shatin, New Territories, Hong Kong
{ypan, jwang}@mae.cuhk.edu.hk

Abstract

Robust model predictive control (MPC) has been investigated widely in the literature. However, for industrial applications, current robust MPC methods are too complex to employ. In this poster, a discrete-time recurrent neutal network model is presented to solve the minimax optimization problem involved in robust MPC. The neural network has global exponential convergence property and can be easily implemented using simple hardware. A numerical example is provided to illustrate the effectiveness and efficiency of the proposed approach.

1 Introduction

Model predictive control (MPC) is a powerful technique for optimizing the performance of control systems, with several advantages over other control systems [1]. MPC applies on-line optimization to the model of a system, by taking the current state as an initial state, a optimization problem is solved at each sample time, and at the next computation time interval, the calculation repeated with a new state.

MPC that take consideration of uncertainties in the process model is called robust MPC. One way to deal with uncertainties in MPC is the worst case approach, which obtains a sequence of feedback control laws that minimizes the worst case cost. In industrial processes, it required the real-time solution to a minimax optimization problem. Although the robustness of MPC has been studied and is now well understood, the research outcomes are conceptual controllers that can work in principle but not suitable for hardware implementation. As a result, further investigations on a more implementable controller are needed.

One very promising approach to dynamic optimization is to apply recurrent neural networks. Recurrent neural networks are brain-like computational models for solving optimization problems in real time. Compared with traditional numerical methods for constrained optimization, neural networks have several advantages: first, they can solve many optimization problems with time-varying parameters; second, they can handle large-scale problems with their parallelizable ability; third, they can be implemented effectively using VLSI or optical technologies.

Neural networks for optimizationand their engineering applications have been widely investigated in the past two decades. Many neural network models have been proposed for solving both linear and nonlinear programming problems. In this poster, we present a discrete-time recurrent neural network model for solving the quadratic minimax optimization problem associated with robust MPC. The neural network is globally exponentially convergent to the saddle point of the objective function.

2 Problem Formulation

2.1 Process Model

Consider the following discrete-time linear system with global bounded uncertainties:

$$\begin{aligned} x(k+1) &= Ax(k) + Bu(k), \\ y(k) &= Cx(k) + Du(k), \end{aligned} \tag{1}$$

with the constraints

$$\begin{aligned} v_{\min} \le v(k) \le v_{\max}, \\ \Delta v_{\min} \le \Delta v(k) \le \Delta v_{\max}, \\ u_{\min} \le u(k) \le u_{\max}, \\ y_{\min} \le y(k) \le y_{\max}. \end{aligned} \tag{2}$$

where $k \ge 0$, $x(k) \in \mathbb{R}^n$ is the state vector, $u(k) \in \mathbb{R}^m$ is the input vector, and $y(k) \in \mathbb{R}^p$ is the output vector. $v(k) \in \mathbb{R}^l$ denotes the vector of bounded uncertainties. $u_{\min} \le u_{\max}$ $v_{\min} \le v_{\max}$ $y_{\min} \le y_{\max}$ are vectors of upper and lower bounds.

2.2 Robust MPC Design

MPC is a step-by-step optimization technique: at each sampling time k, measure or estimate the current state, obtain the optimal input vector by solving a optimization problem. When bounded uncertainties are considered explicitly, a robust MPC law can be derived by minimizing the maximum cost within the model described by the uncertainty set. The optimal control action is obtained by solving a minimax optimization problem:

$$\min_{\Delta u} \max_{v} \quad J(\Delta u, v), \tag{3}$$

subjected to the constraints in (2).

The objective function $J(\Delta u, v)$ can be with an infinite or finite, linear or quadratic norm criterion. In this poster, we consider an objective function with a finite horizon quadratic criterion:

$$\begin{aligned} J(\Delta u, u) = &\sum_{j=0}^{N} \|r(k+j|k) - y(k+j|k)\|^2_{\Theta} + \|y(k+j|k) - y(k+j-1|k)\|_{\Phi} + \\ &\sum_{j=0}^{N-1} \|\Delta u(k+j|k)\|^2_{\Psi} + \|\Delta u(k+j|k)\| \end{aligned} \tag{4}$$

where k is the current time step, $y(k+j|k)$ denotes the predicted output, $r(k+j|k)$ denotes the reference trajectory of output signal (desired output), and $\Delta u(k+j|k)$ denotes the input increment, where $\Delta u(k+j|k) = u(k+j|k) - u(k+j-1+j|k)$. $\Psi \in \mathbb{R}^{m\times m}$, $\Phi \in \mathbb{R}^{p\times p}$, $\Theta \in \mathbb{R}^{m\times m}$ are appropriate weighting matrices. N denotes the predictive horizon ($1 \le N$). N_u denotes the control horizon ($0 < N_u \le N$). After N_u control moves, $\Delta u(k+j|k)$ becomes zero.

According to the process model (1):

$$y(k+j) = CA^j x(k) + C\sum_{i=0}^{j} A^i Bu(k+j-i-1) + Du(k+j), \quad j = 1, \ldots, N \tag{5}$$

Define the variable vectors $z = \Delta u(k) = [\Delta u(k|k) \quad \cdots \quad \Delta u(k+N_u-1|k)]^T \in \mathbb{R}^{mN_u}$, $u = u(k) \in \mathbb{R}^m$. By neglecting the constraints on $u(k)$ and $y(k)$, the problem (3) can be rewritten as a minimax quadratic programming problem:

$$\begin{aligned} \min_{z} \max_{v} \quad & \frac{1}{2} z^T Q z + v^T u - u^T H z - \frac{1}{2} u^T R u - b^T z \\ \text{s.t.} \quad & z \in \Omega, \quad u \in W \end{aligned} \tag{6}$$

where Ω and W are two box set defined as $\Omega = \{z \in \mathbb{R}^{N_u m} | \Delta u_{\min} \le z \le \Delta u_{\max}\}$, $W = \{u \in \mathbb{R}^m | u_{\min} \le u \le u_{\max}\}$. The coefficient matrices and vectors Q, R, H, b and c are obtained from A, B, C, D, (4) and (5).

The solution to the minimax quadratic programming problem (6) gives the vector of control action $\Delta u(k)$. The control law is given by $u(k) = f(\Delta u(k) + u(k-1))$, where $u(k) = [u(k|k) \quad \cdots \quad u(k+N_u-1|k)]^T \in \mathbb{R}^{lN_u}$, and $f(\cdot)$ is defined as

$$f(z_i) = \begin{cases} z_i & \text{if } z_i \in \Omega, \\ l_i & \text{if } z_i > l_i. \end{cases} \tag{7}$$

where G and l are obtained from (2) and (5).

In industrial control processes, to solve large-scale minimax optimization problems in real-time is a major obstacle for robust MPC. In the next section, we will propose a recurrent neural network for solving (6).

3 Neural Network Approach

3.1 Neural Network Model

In recent years, many neural network models have been proposed for solving optimization problems. In particular, continuous-time neural networks for solving minimax problems has been investigated in [2, 3]. However, in view of the availability of the digital hardware and the compatibility to the digital computers, discrete-time neural network is more desirable in practical implementation. In this section, we proposed a discrete-time recurrent neural network for minimax problem (6).

By the saddle point condition [4], (6) can be formulated as a linear variational inequality (LVI):

$$(u - u^*)^T (Mx^* + q) \ge 0, \quad \forall x \in \Omega, \tag{8}$$

where

$$M = \begin{bmatrix} Q & -H^T \\ H^T & R \end{bmatrix}, \quad q = \begin{bmatrix} c \\ b \end{bmatrix}, \quad \Omega = \Omega \times W. \tag{9}$$

According to the well-known saddle point theorem [4], $w^* = (u^*, u^*)$ is a saddle point of $J(u, w)$ if satisfying

$$J(u^*, w) \le J(u^*, w^*) \le J(u, w^*), \quad \forall (u, w) \in \Omega. \tag{10}$$

We define the saddle point set $\Omega^* = \{(u^*, w^*) \in \Omega | (u^*, w^*) \text{ satisfy } (10)\}$ and assume Ω^* is not empty. It is obvious that if $(u^*, w^*) \in \Omega^*$, then (u^*, u^*) is the optimal solution to the minimax problem (6).

According to inequalities (10), we can get that u^* is a global minimizer of the objective function $J(u, w^*)$ with respect to Ω, while w^* is the global minimizer of $J(u^*, w)$ with respect to W. As a result, the following LVIs hold:

$$(u - u^*)^T (Qu^* + c - Hw^*) \ge 0, \quad \forall u \in \Omega, \tag{11}$$

$$(w - w^*)^T (Hu^* + b + R^T w^*) \ge 0, \quad \forall w \in W. \tag{12}$$

According to the basic property of the projection mapping on a closed convex set:

$$[z - P_\Omega(z)]^T [P_\Omega(z) - v] \ge 0, \quad \forall z \in \mathbb{R}, v \in \Omega. \tag{13}$$

Based on (11)-(13) and lemma 1 in [2], we can get that $(u^*, w^*) \in \Omega^*$ if and only if the following equationsholds:

$$u^* = P_\Omega[u^* - \alpha(Qu^* + c - Hw^*)] \tag{14}$$

$$w^* = P_W[w^* + \alpha(Hu^* + b + H^T w^*)] \tag{15}$$

where $\alpha > 0$ is a scaling constnt, $P_\Omega(\cdot)$ and $P_W(\cdot)$ are piecewise activation functions defined as:

$$P_\Omega(z_i) = \begin{cases} \Delta v_{\min}, & z_i < \Delta v_{\min}, \\ z_i, & \Delta v_{\min} \le z_i \le \Delta v_{\max}, \\ \Delta v_{\max}, & z_i > \Delta v_{\max}. \end{cases} \quad P_W(z_i) = \begin{cases} w_{\min}, & z_i < w_{\min}, \\ z_i, & w_{\min} \le z_i \le w_{\max}, \\ w_{\max}, & z_i > w_{\max}. \end{cases} \tag{16}$$

Based on the equations (14) and (15), we propose a recurrent neural network for solving (6) as follow:

$$\begin{cases} u(t+1) = P_\Omega[u(t) - \alpha(Qu(t) + c - Hw(t))] \\ w(t+1) = P_W[w(t) - \alpha(Hu(t) + b + H^T u(t))] \end{cases} \tag{17}$$

The proposed recurrent neural network model (17) has a simple structure, and can be easily implemented using digital hardware.

3.2 Convergence Analysis

Definition 1. *Neural network (17) is said to be globally exponentially convergent to the equilibrium point (u^*, w^*) if both u^* and w^* satisfy*

$$\begin{aligned} \|u(t) - u^*\| &\le \alpha_0 \|u(0) - u^*\| e^{-\alpha t}, \quad \forall t \ge 1; \\ \|w(t) - w^*\| &\le b_0 \|w(0) - w^*\| e^{-\alpha t}, \quad \forall t \ge 1; \end{aligned} \tag{18}$$

where α is a positive constant independent of the initial point, α_0 and b_0 are positive constant dependent on the initial point.

Lemma 1. *The neural network (17) has a unique equilibrium point, which is the saddle point of $J(u, w)$.*

Lemma 2. *For all $z \in \mathbb{R}^n$,*

$\|P_\Omega(z) - P_\Omega(z)\|^2 \le \|z - z\|^2$, $\|P_W(z) - P_W(z)\|^2 \le \|z - z\|^2$.

Define $\lambda_i^Q \ge 0 (i = 1, \ldots, N_u m)$, $\lambda_i^R \ge 0 (j = 1, \ldots, Nq)$ as the eigenvalues of Q, R respectively, let $\lambda_{\min}^Q$, $\lambda_{\max}^Q$, $\lambda_{\min}^R$, $\lambda_{\max}^R$ be the smallest and largest eigenvalues of Q and R. Define two functions:

$$\psi^{(1)}(\alpha) = \begin{cases} 1 - \lambda_{\min}^Q \alpha, & 0 < \alpha \le 2/(\lambda_{\min}^Q + \lambda_{\max}^Q) \\ \lambda_{\max}^Q \alpha - 1, & 2/(\lambda_{\min}^Q + \lambda_{\max}^Q) \le \alpha < +\infty \end{cases} \tag{19}$$

$$\psi^{(2)}(\alpha) = \begin{cases} 1 - \lambda_{\min}^R \alpha, & 0 < \alpha \le 2/(\lambda_{\min}^R + \lambda_{\max}^R) \\ \lambda_{\max}^R \alpha - 1, & 2/(\lambda_{\min}^R + \lambda_{\max}^R) \le \alpha < +\infty \end{cases} \tag{20}$$

Then we give the following lemma:

Lemma 3. *$\psi^{(1)}(\alpha) < 1$ and $\psi^{(2)}(\alpha) < 1$ if and only if*

$$0 < \alpha < \min\{2/\lambda_{\max}^Q, 2/\lambda_{\max}^R\}. \tag{21}$$

Theorem 1. *With any α that satisfies (21), the neural network (17) is globally exponentially convergent to the saddle point of $J(u, w)$.*

3.3 Control Scheme

The control scheme based on proposed recurrent neural network can be summarized as follows:

1. Let $k = 1$. Set terminal time T, sample time t, predictive horizon N, control horizon N_u, weighting matrices Φ and Θ.
2. Calculate process model matrices and neural network parameters.
3. Solve the quadratic minimax problemn (6) using the proposed recurrent neural network, obtaining the optimal control action $\Delta u(k)$.
4. Calculate the optimal input vector $u(k) = f(\Delta u(k) + u(k-1))$, the first element $u(k|k)$ is sent to the process.
5. If $k < T$, set $k = k + 1$, return to step 2; otherwise, end.

4 Numerical Example

Consider a two-tank system described in [5], which is a two-input, two-output system, with the flow rates of the two inlet streams as the two inputs, and the liquid level in each tank as the two output variables.

By sampling at 0.2 min using a zero-order holder, the following discrete-time state-space model can be obtained:

$$\begin{aligned} x(k+1) &= \begin{bmatrix} 0.923 & 0.077 \\ 0.067 & 0.933 \end{bmatrix} x(k) + \begin{bmatrix} 0.148 & 0 \\ 0 & 0.113 \end{bmatrix} u(k) \\ y(k) &= \begin{bmatrix} 1 & 0 \\ 0 & 1 \end{bmatrix} x(k) \end{aligned} \tag{22}$$

The set-point for the liquid levels (output) of tanks 1 and 2 are 0.8 and 0.7, respectively; the prediction and control horizons are $N = 10$ and $Nu = 4$; weighting matrices $\Phi = I$, $\Psi = 1I$; scaling constant $\alpha = 0.2$; an uncertainty $-0.02 \le w \le 0.02$ is considered to affect both liquid levels of tanks 1 and 2; moreover, the following constraints are considered:

$$\begin{aligned} \begin{bmatrix} 0 \\ 0 \end{bmatrix} \le u(k) \le \begin{bmatrix} 0.5 \\ 0.5 \end{bmatrix}, \quad \begin{bmatrix} 0 \\ 0 \end{bmatrix} \le y(k) \le \begin{bmatrix} 0.8 \\ 0.7 \end{bmatrix} \\ \begin{bmatrix} -0.05 \\ -0.05 \end{bmatrix} \le \Delta u(k) \le \begin{bmatrix} 0.05 \\ 0.05 \end{bmatrix} \end{aligned} \tag{23}$$

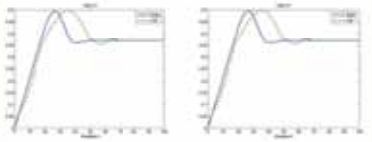

Figure 1. Input signals oftanks 1 and 2 using the proposed RNN approach and LMI approach.

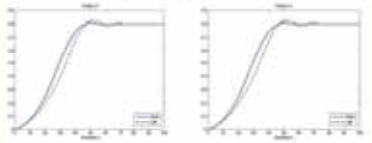

Figure 2. Output responses of tanks 1 and 2 using the proposed RNN approach and LMI approach.

In order to compare the effectiveness and efficiency of the proposed approach, a linear matrix inequalities (LMI) approach [5] is also applied to the process. The simulation results are showed in Figs. 1 - 2. We can see that the proposed neural network approach gives a better set-point tracking performance with faster stable output responses.

5 Conclusion

This poster presents a new approach to robust MPC based on a discrete-time recurrent neural network by solving a minimax optimization problem. The neural network is proved to have global exponential convergent property. Simulation results show the superior performance of the neural network approach. Compared with alinear matrix inequalities approach, the proposed neural network approach gives a better performance in set-point tracking.

References

[1] Camacho, E., Bordons, C.: Model Predictive Control. Springer (2004)

[2] Gao, X., Liao, L., Xue, W.: A neural network for a class of convex quadratic minimax problems with constraints. IEEE Trans. Neural Netw. **15** (2004) 622-628

[3] Gao, X., Liao, L.: A novel neural network for a class of convex quadratic minimax problems. Neural Computation **18** (2006) 1818-1846

[4] Bazaraa, M., Sherali, H., Shetty, C.: Nonlinear programming: theory and algorithms. (1993)

[5] Alamo, T., Ramirez, D., Camacho, E.: Efficient implementation of constrained min–max model predictive control with bounded uncertainties: a vertex injection approach. Journal of Process Control **15** (2005) 149–158

HUANG Lin **Supervisor: Prof. XU Qiang**
Department of Computer Science and Engineering,
Faculty of Engineering

Project Title "On Modeling the Lifetime Reliability of Manycore Processors"

Student Poster

ON MODELING THE LIFETIME RELIABILITY OF MANYCORE PROCESSORS

Lin Huang and Qiang Xu
Department of Computer Science & Engineering
The Chinese University of Hong Kong, Shatin, N.T., Hong Kong

Introduction

Advancements in technology enable the integration of many embedded processing elements on a single silicon die. State-of-the-art processor has started to employ this technique to improve performance through parallel execution instead of frequency increase, which has the benefits of power-efficiency and short time-to-market. Nvidia Geforce 8800 128-core GPU and Tilera Tile 64-core general purpose processor have already been released to the market. Intel has also demonstrated an 80-core teraflop processor prototype in 2006. Various research teams have projected that thousand-core processor chips will become commercially available in the foreseeable future.

At the same time, while the relentless scaling of CMOS technology has brought with it enhanced functionality and improved performance in every new generation, the associated ever-increasing on-chip power and temperature densities make the lifetime reliability of high-performance integrated circuits (ICs) one of the major concerns for the industry today.

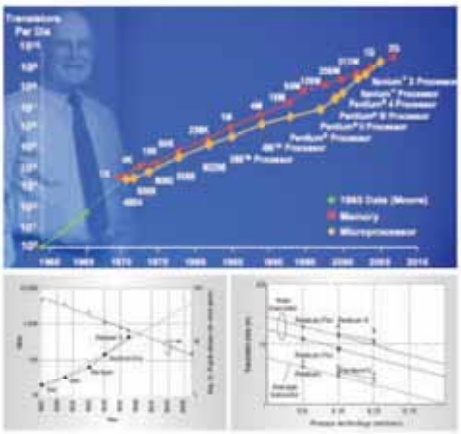

Figure 1. Moore's Law Continues

Figure 2. Trend to Manycore

Challenges

Based on this observations, we model a manycore processor as a load-sharing nonrepairable *k*-out-of-*n* G system with general reliability functions for embedded cores, which introduce three challenges to estimating the lifetime reliability. First, an active embedded core may frequently alternative between the processing and wait state, depending on whether it is performing tasks. An embedded core can also be in the standby mode, if standby redundancy schemes are used. Each state has its own failure distribution. Note that, to capture the aging effect of cores, these distributions cannot be exponential ones which has good mathematical tractability. Second, we only know the task allocation mechanism; while the number of components in each state at a particular moment is dependent on the current workload and hence is uncertain. Third, since the embedded cores share the workload, the failure of one core may results in higher load and hence increasing failure rate on surviving cores.

Figure 4. States of an Embedded Core

Key Features

a) Manycore processors are nonrepairable systems.
Unlike traditional board-level multiprocessor systems that can be easily repaired by replacing defective chip, embedded cores are integrated on silicon die in manycore processors and it is extremely difficult to repair or replace a faulty core, if not possible.

Figure 3. IBM System 360 Model 30 (1960s) and Intel 80-Core Teraflop (2006)

b) They are k-out-of-n G system.
n is the total number of embedded cores fabricated on-chip and *k* is the minimum number of cores required for the system's functioning. Typically, *n* is larger than *k* to provide fault tolerance.

c) They are load-sharing system.
Each embedded core carry only part of the load assigned by operating system. Empirical studied shows that a core's failure rate highly depends on its workload that determines the temperature and voltage applied to the circuit.

d) Embedded cores will age in operation.
That is, we expect an increasing failure rate when a core gets older.

Methods

We first capture the relationship between task allocation mechanisms and the accumulated usage time in either state of cores by using M^c/M/c queuing model. Sequentially, we prove that if the failure distributions of embedded cores can be represented by accelerated failure-time model (AFTM), the lifetime reliability of a core only depends on its accumulated usage time in two states, independent of details events in its lifetime, and therefore achieve the reliability function of an embedded system under a certain task allocation mechanism and workload. Finally, we figure out the reliability function of entire manycore processor by modeling this system as a *k*-out-of-*n* G system.

Conclusion

State-of-the-art technology enables the integration of a great amount of embedded cores on a single silicon die. Meanwhile, aggressive technology scaling has an ever-increasing adverse impact on the lifetime reliability of such large integrated circuits. The analytical model proposed in this work enable us to analyze the impact of architecture redundant schemes, operating system task allocation mechanisms, processor workload, and IC products' aging effect on the lifetime reliability of manycore processors.

ZHANG Peng **Supervisor: Prof. DU Ru Xu**
Department of Mechanical and Automation Engineering,
Faculty of Engineering

Project Title "Design and Fabrication of New Energy Harvest Device Based on Thermal Driven Micro Flow"

Design and Fabrication of New Energy Harvest Device Based on Thermal Driven Micro Flow

Zhang Peng, Prof. R. Du

In the 21st century, energy is one of the biggest concerns. Through the research, various kinds of methods are invented to capture and convert energy from nature resources of different forms such as solar, wind, mineral, and etc. On other hand, the recent advance of Micro-Electro-Mechanical Systems (MEMS) technology has opened new ways for us to use micro / nano scale physical and chemical effects. Based on these micro / nano scale effects, new energy capture and conversion methods become possible. In this research, a new energy harvest device is proposed. The basic idea is to capture the thermal energy and converts to kinetic energy and then the electric energy. The key component of the new device is the Knudsen compressor which is based on the rarefied flow phenomenon of thermal creep. In this study, the possibility of Knudsen compressor filled with nano scale aerogel working in atmosphere pressure is first studied by computer simulation. It shall be pointed out that as the Knudsen number becomes large due to the decreased characteristic length, the flow can only be described from a molecular point of view. Thus, the Direct Simulation Monte Carlo (DSMC) method is used. The simulation results provide the information for design and fabricate a Knudsen compressor.

Knudsen Compressor Driven by Solar Energy

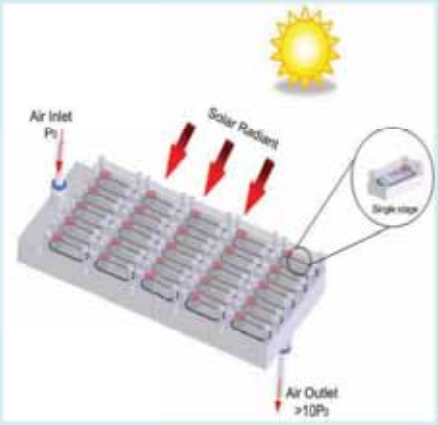

Multi-Stages Knudsen Compressor

Single Stage Knudsen Compressor

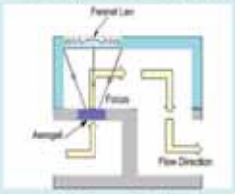

A-A Cross-Section

Theory about Thermal Creep

Elementary single stage of a thermal creep

If the aperture area A becomes comparable to the mean free path (λ), The mass fluxes at the hot and the cold end of the channel are $\overline{m_1 C_1}$ and $\overline{m_2 C_2}$ respectively. Then

$$\frac{\overline{m_1 C_1}}{\overline{m_2 C_2}} = \frac{p_1}{p_2}\sqrt{\frac{T_2}{T_1}} = \frac{P_1}{P_2}\left(\frac{T_2}{T_1}\right)^{\frac{n+1}{2}} = \left(\frac{T_2}{T_1}\right)^{\frac{n}{2}} \geq 1$$

The above analysis indicates a flow creeping from cold to hot.

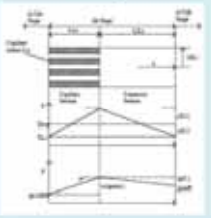

Illustrative one stage of a Knudsen Compressor[Wang]

The analysis of the Knudsen compressor is based on the Equations below

$$\mu_1 = \prod_{i=1}^{n} P_i = \prod_{i=1}^{n} (1 + \varepsilon_i \frac{\Delta P_i}{P_{avi}} \frac{Q_{1i}}{Q_{2i}})$$

$$(1+(\varepsilon_i/2)\frac{\Delta P_i}{P_{avi}})\alpha_i \frac{Q_{1i}}{Q_{2i}} \cong 1$$

$$M_s = \frac{P_{av1} F_p A [2kk/m\delta T_{av1}]^{1/2}}{(L_c/L_t)} \frac{\Delta T_p}{T_{av1}} Q_{1i}(1-\kappa_i)$$

$$Q_{1i} = \sum_{i=1}^{n} (\frac{\Delta T}{L_{ti}}) K_{ni} A_i (1 - P_i) A_i$$

$$A_i = \frac{2(2kT_{av1}/m\delta)^{1/2} K n_i L_{ti}}{Q_{1i}(\Delta T_p) P_{av}(1-\kappa_i)} M_{ave}$$

Simulation Results by DSMC

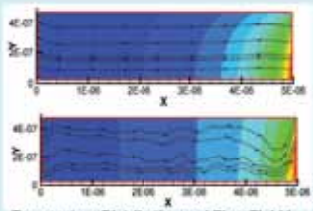

Temperature Distribution and Flow Field in Micro Channel

Simulation results show the gas flow in the same micro-channel have different direction under different Kn. In lower fig.(Kn=50), the gas flows from cold end to the hot end, This is consisting with our expectation. Buy in upper fig.(Kn=0.05), the flow direction is opposite. It is because the Knudsen number determine which effect is dominate effect in the micro-channel, the pressure driven flow or thermal driven flow.

In this fig., we found the zero mass flow happens at Kn=2. Another interesting phenomenon is the mass flow is not monotonous increasing or decreasing with the Kn. There is a maximum mass flow happens at Kn=5 (corresponding to P=0.01atm). This is because the trade-off between gas velocity and density. In our design, we can adjust the dimensions and operating pressure to make the Knudsen compressor working around the maximum mass flow rate.

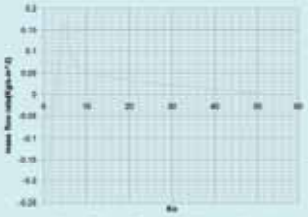

Mass Flow Rate of Different Knudsen number

Technologies Involved

A high porous solid material, aerogel has the lowest density of any solid known to man and earns the nickname,"solid blue smoke."

The aerogle's extremely fine microstructure and high thermal insulating property could greatly improve the performance of Knudsen Compressor.

Microstructure of Aerogel

Thermal Insulator

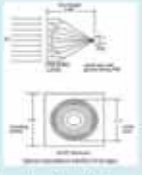

Cross-Section fo Fresnel Lens

Linear Fresnel Array

A Fresnel lens is a type of lens invented by French physicist Augustin-Jean Fresnel. Compared to earlier lenses, the Fresnel lens is much thinner, thus passing more light and allowing lighthouses to be visible over much longer distances.

iPE
http://www.ipe.cuhk.edu.hk
Rm 410, William M.W. Mong Engineering Building, CUHK, Shatin, N.T., Hong Kong
Tel: (852) 2609 8054. Fax: (852) 2603 6002

AU Chun Hang **Supervisor: Prof. KWAN Hoi Shan**
Department of Biology, Faculty of Science

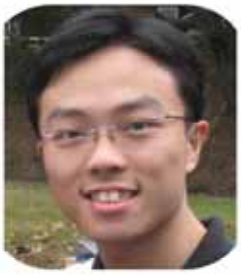

Student Poster

Project Title "Gene expression studies of the dikaryotic mycelium and primordium of Lentinula edodes by serial analysis analysis of gene expression"

Gene expression studies of the dikaryotic mycelium and primordium of *Lentinula edodes* by serial analysis of gene expression

W. W. Y. CHUM; K. T. P. NG; R. S. M. SHIH; C. H. AU; H. S. KWAN*

Mycological Research (2008), in press
(doi: 10.1016/j.mycres.2008.01.028)

Department of Biology, The Chinese University of Hong Kong

Acknowledgement
This project was supported by the CERG research grant CUHK4139/98M & CUHK4147/01M from the Research Grants Council of the Hong Kong Special Administrative Region, PRC.

Abstract

Lentinula edodes (Shiitake mushroom) is a common edible mushroom that has high nutritional and medical value. Although a number of genes involved in the fruiting of the species have been identified, little is known about the process of differentiation from dikaryotic mycelium to primordium. In this study, serial analysis of gene expression (SAGE) was applied to determine the gene expression profiles of the dikaryotic mycelium and primordium of *L. edodes* in an effort to advance our understanding of the molecular basis of fruiting body development. A total of 6,363 tags were extracted (3,278 from the dikaryotic mycelium and 3,085 from the primordium), 164 unique tags matched the in-house expressed sequence tag (EST) database. The difference between the expression profiles of the dikaryotic mycelium and primordium suggests that a specific set of genes is required for the fruiting body development. In the transition from the mycelium to the primordium, different hydrophobins were expressed abundantly, fewer structural genes were expressed, transcription and translation became active, different genes became involved in intracellular trafficking, and stress responses were expressed. These findings advance our understanding of fruiting body development. We used cDNA microarray hybridization and Northern blotting to verify the SAGE results, and found SAGE to be highly efficient in the performance of transcriptome analysis. To our knowledge, this is the first SAGE study of a mushroom.

Life Cycle of *Lentinula edodes* (香菇)

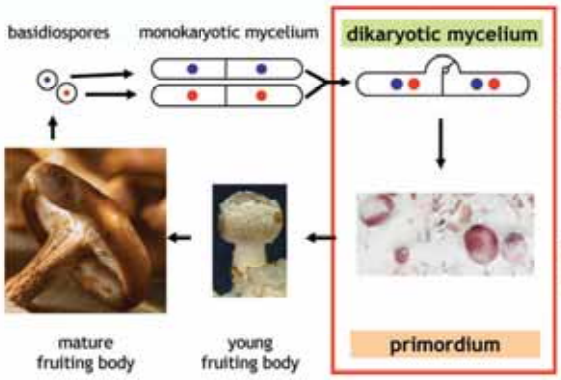

Question

- Which genes are involved in such differentiation?

Hypothesis

- Differentially expressed genes are involved in such differentiation

Objective

- To identify genes differentially expressed in either stages, through serial analysis of gene expression

Serial Analysis of Gene Expression

Bioinformatics

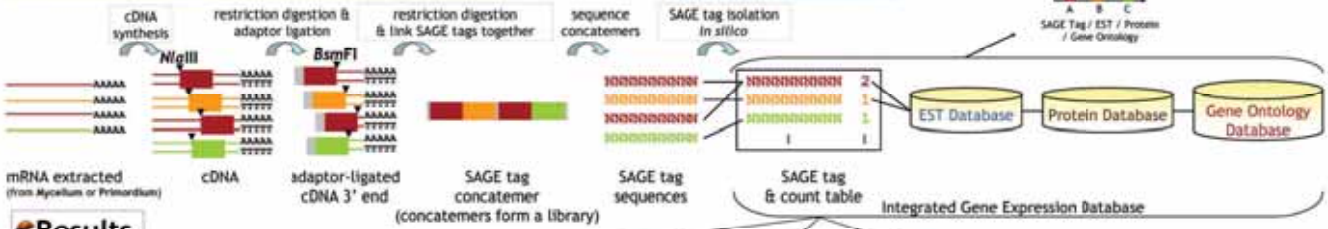

Results

Summary of both SAGE libraries

	Dikaryotic mycelium	Primordium	Combined Both
Total tags	3,278	3,085	6,363
Unique tags	1,984	1,895	3,545
Unique tags (copy no. ≥ 3)	184	191	293
Unique tags mapped to EST	108	113	164
Unique tags mapped to EST (copy no. ≥ 3)	66	78	93
Unique tags differentially expressed	34	40	-

Roles of differentially expressed genes in either stages

	Dikaryotic mycelium	Primordium
Structural component	Hydrophobin 2 & others	Hydrophobin 1
Transcription and translation machinery	(less) ↓ Diversity	↑ (more)
Signal Transduction	↓ Gα & ADP-Ribosylation factor 1	↑
Proteome turnover	↓ Ubiquitin	↑
Stress response	NADPH oxidase I	Metallothioneins

SAGE tag distribution

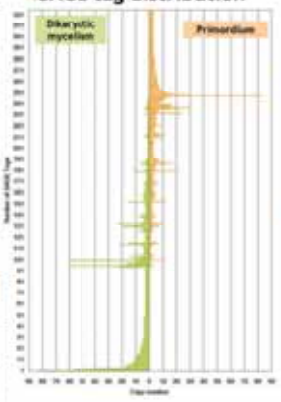

Most abundant SAGE tags in either stages

SAGE Tag	Copy number: Myc	Pri	F-value	Protein Homolog	EST Clone
Most abundant in dikaryotic mycelium					
GCTTGACGAG	83	0	2E-16	-	-
GAAGACGAAA	61	11	4E-09	-	01B02
CAGTTCAAAC	60	3	3E-14	Hydrophobin 2	10E01
TTTTCTATAT	56	0	2E-16	-	-
GATATTGTCT	40	0	3E-12	Hydrophobin 3	03G08
Most abundant in primordium					
CCAATCCCAG	0	83	2E-16	Hydrophobin 1	PEL0163
TCCCTATTAA	4	30	2E-06	-	-
ATGGGGCATA	0	29	7E-10	-	-
CCAATGACAG	4	24	7E-05	40S ribosomal protein S27a	HKLC10859
CGCTTAGGTT	3	22	6E-05	-	HKLC15204

Summary

- SAGE libraries of dikaryotic mycelium and primordium prepared, cloned and sequenced
- SAGE tags are matched to EST, protein and Gene Ontology (automated)
- 34 and 40 SAGE tags are differentially expressed in dikaryotic mycelium and primordium, respectively

Future Perspectives

- Comparative gene expression analysis of *Lentinula edodes* and *Coprinopsis cinerea*
- Functional studies of differentially expressed genes presented here in *Coprinopsis cinerea*, a model mushroom for genetic study

Key References

- Velculescu VE, Zhang L, Vogelstein B, Kinzler KW, 1995. Serial analysis of gene expression. Science 270: 484-487
- Chum WWY, Kwan HS, 2005. Modification of LongSAGE for obtaining and cloning long concatemers. Biotechniques 39: 637-638, 640

Notes

*Corresponding Author: Prof. Hoi Shan KWAN
(email address: hoishankwan@cuhk.edu.hk)

WONG Yuk Lau **Supervisor: Prof. KWAN Kin Ming**
Department of Biology, Faculty of Science

Project Title "Functional analysis of BMPs signaling in mouse limb bud interdigital cell death"

Functional Analysis of BMPs signaling in mouse limb bud interdigital programmed cell death

Yuk Lau Wong and Kin Ming Kwan
Department of Biology, The Chinese University of Hong Kong

Abstract

Programmed cell death is an important process that regulates development and homeostasis in multicellular organisms. It also plays an important role in sculpting the shape and structure of developing limb and is coordinated in developing limb by reciprocal epithelial-mesenchymal interactions between specialized regions of the limb bud under the effects of different signaling factors like FGFs, BMPs, Wnts and Shh.
Bone morphogenetic proteins (BMPs), members of TGF-β superfamily, are secreted signaling molecule shown to be one of the important factors that regulate programmed cell death but the intracellular molecular components and pathways involved remain largely unknown.
Cre/loxP system was employed to investigate the molecular components of BMPs signaling in developing limb. Bmprla or Smad1 and Smad5 were inactivated in developing limb ectoderm in a tissue-specific manner by the use of Bmprla or Smad1 and Smad5 floxed alleles and Engrailed1-Cre-recombinase transgene (En1-Cre).The preliminary data of our lab showed that the limb of the mutants has syndactyly. This shows that Bmprla, Smad1 and Smad5 are involved in regulating BMPs-mediated cell death in interdigital regions.
Further experiments including cell proliferation and cell death assay and in situ hybridization will be performed to investigate possible molecular mechanisms of Smad1 and Smad5 in regulating programmed cell death in interdigital regions.

Background: Summary of BMPs signaling pathway

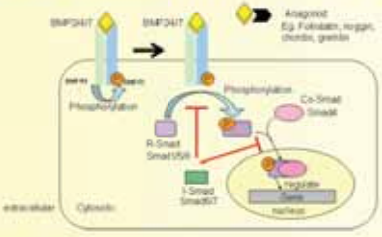

Binding of BMP ligands to membrane-bound serine/threonine kinase receptors would result in receptor phosphorylation and hence activation of receptor-regulated Smad proteins (R-Smads) by phosphorylation. Smads1/5/8 are intracellular mediators that transduce extracellular BMP signals from cell surface to nucleus. Activated Smad1, 5 or 8 form complexes with common partner Smad (CoSmad), Smad4 and translocate into nucleus where they regulate transcription of target genes.
Knock-out of BMPs and its signaling components would result in early embryonic lethality which hinders studies of BMPs signaling in limb formation occurred at later stages.

Approach of the studies: Conditional Inactivation of BMPs signaling components by Cre/loxP system

Cre/loxP system was employed to inactivate Bmprla, Smad1 or Smad5 in developing limb ectoderm in a tissue-specific manner. This would circumvent the problem of embryonic lethality and allow studies of roles and molecular mechanisms of Smads protein in limb formation.

Principle of Cre/loxP system:
The gene to be inactivated is flanked by two loxP site and is said to be floxed. When the Cre-recombinase is expressed, it will recognize the two loxP sites and excise the loxP-flanked sequence then gene will be disrupted and inactivated. The tissue-specificity is achieved by using Cre driven by specific promotor. Cre is expressed at certain tissue but not other. Thus the targeted gene is inactivated only in that particular tissue while remains unaffected in other tissue.

Cre Transgene to be used: En1-Cre Transgene

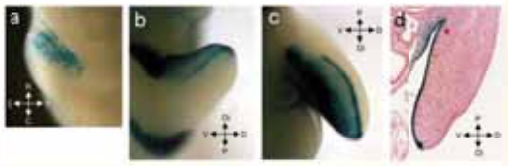

En1-Cre first expresses in ventral ectoderm of forelimb in E9.5 embryo and in ventral ectoderm of both forelimb and hindlimb in E10.5 embryo.

Limb showing partial syndactyly in conditional Bmprla mutant using En1-Cre mouse line

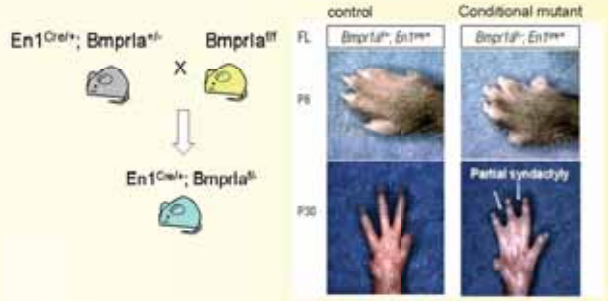

Bmprla was inactivated using En1-Cre transgere and the mutant limbs show partial syndactyly. At P8, stage which the digits are separated in normal nice, the digit are connected by interdigital tissue so as P30 individuals. Therefore, the webbing phenotype is due to problem with interdigital tissue regression but not delay in interdigital regression. Bmprla is the receptor involved in regulating cell death in interdigital regions

Limb showing syndactyly in conditional Smad1/5 mutant using En1-Cre mouse line

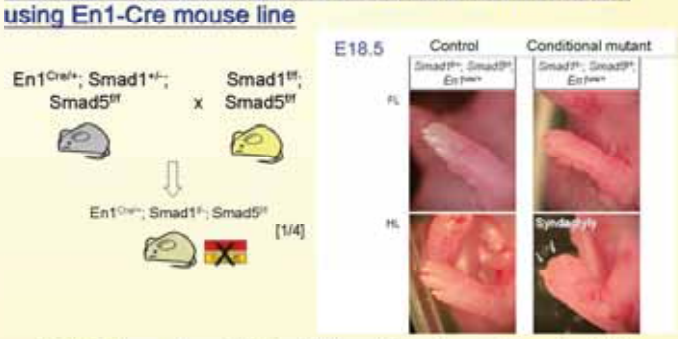

At E18.5, stage where individual digit could be observed, separated digits were not clearly seen in both forelimb and hindlimb. They remain plate-like. This shows that Smad1 and Smad5 are intracellular mediators of BMPs -mediated cell death and are of redundant role.

Reference

1. Kwan K. M., Li A.G., Wang X.J., Wurst W. and Behringer R.R. 2004. Essential roles of BMPR-IA signaling in differentiation and growth of hair follicles and in skin tumorigenesis. Genesis 39(1):10-25.
2. Pajni-Underwood S., Wilson C.P., Elder C., Mishina Y. and Lewandoski M. 2007. BMP signals control limb bud interdigital programmed cell death by regulating FGF signaling. Development 134(12):2359-68.
3. Robert B. 2007. Bone morphogenetic protein signaling in limb outgrowth and patterning. Dev. Growth Differ. 49(6):455-68.
4. Zuzarte-Luis V. and Hurle, J.M. 2005. Programmed cell death in the embryonic vertebrate limb. Semin Cell Dev Biol. 16(2):261-9

TSUI Wing Wun **Supervisor: Prof. KWAN Kin Ming**
Department of Biology, Faculty of Science

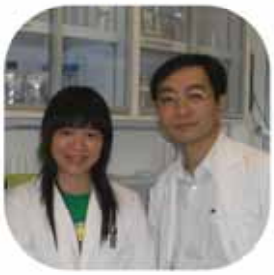

Student Poster

Project Title "Generation of Lhx1-tauGFP transgenic mice: a tool for in vivo study of Lhx1 functions"

Generation of *Lhx1-tauGFP* transgenic mice: a tool for *in vivo* study of *Lhx1* functions

Wing Wun Tsui and Kin Ming Kwan

Department of Biology, The Chinese University of Hong Kong

Abstract

The LIM-homeodomain (HD) proteins are essential during development as they play diverse roles in different organogeneses. *Lhx1* (also known as *Lim1*), a LIM-HD protein (figure 1), has been shown to be essential for the development of head, kidney, and gonads during mouse embryogenesis. *Lhx1* and *Lhx5*, another closely related LIM-HD protein, have also been shown to play important role in the Purkinje neurons development in prenatal mouse cerebellum (figures 2 and 3). *Lhx1* and *Lhx5* also co-express in postnatal and adult cerebellar Purkinje neurons (figure 4), suggesting that they may also play important role in Purkinje neurons survival and/or maintenance. To dissect the functions of *Lhx1* and *Lhx5* in the differentiating and fully mature Purkinje neurons, the strategy of conditional inactivation of *Lhx1* and *Lhx5* genes will be employed. To achieve this goal, an *Lhx1* null allele with reporter function is required to visualize any phenotypic changes in living *Lhx1* expressing Purkinje neurons in the *Lhx1/5* double conditional mutant mice. However, previously used *Lhx1-LacZ* reporter gene cannot be applied to trace living *Lhx1* expressing cells, despite its faithful expression which resembles endogenous *Lhx1* expression (figure 5). To address this limitation, the *tau-GFP* (Green Fluorescent Protein) reporter gene will be used instead of *Lhx1-LacZ* reporter gene. *Tau* is a microtubule-associated protein and microtubules are known to be abundant in axons. GFP requires no substrate and can be directly detected in living cells by fluorescence microscopy. Thus, the *tau-GFP* fusion gene product can be efficiently targeted to axonal processes, permitting the visualization of the morphology of the *Lhx1* expressing Purkinje neurons in exquisite detail by live imaging of fresh cerebellum tissue.

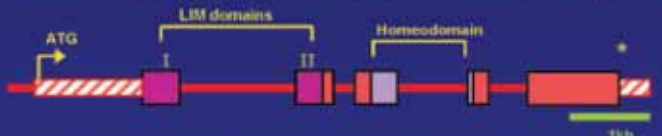

Figure 1. Structure of mouse *Lhx1* gene. The 5 exons are indicated by boxes, introns are represented by the lines connecting the exons. The thinner hatched boxes indicate the 5' and 3' UTRs. The asterisk indicates the translation stop codon. (Ref. 5)

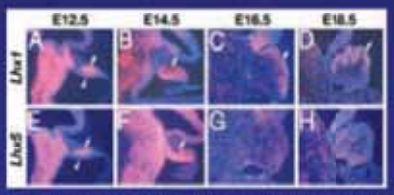

Figure 2. *In situ* hybridization showing the co-expression of *Lhx1* and *Lhx5* genes in the Purkinje neurons in prenatal mouse cerebellum. Arrows in (A – H) point at region where *Lhx1* or *Lhx5* was expressed. Arrowheads in (A) and (E) show the ventricular zone of the cerebellum (Ref. 7)

Objective

To generate the *Lhx1-tauGFP* transgenic mouse (*Lhx1* $^{tauGFP/+}$) which is heterozygous for the *Lhx1* locus, carrying one wild-type *Lhx1* allele and one modified *Lhx1- tauGFP* reporter allele

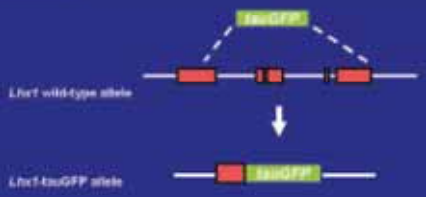

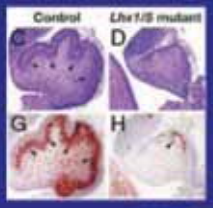

Figure 3. Severe reduction in cerebellar Purkinje neurons number in *Lhx1/Lhx5* double mutants. The cerebellum of mutant embryos (D and H), as compared with that of wild-type embryos (C and G), was analyzed by hematoxylin and eosin staining (C and D) and immunostaining of calbindin, a marker for Purkinje neuron (G and H). Arrowheads in (C) and (G) point out the developing Purkinje neurons. The arrowhead in (H) shows residual calbindin-positive cells present in the *Lhx1/Lhx5* double mutants. (Ref. 7)

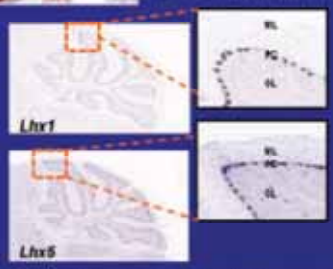

Figure 4. *In situ* hybridization showing the co-expression of *Lhx1* and *Lhx5* genes in 7-week old adult mouse cerebellum. ML: Molecular layer; PC: Purkinje neuron layer; GL: Granule cell layer (Ref. 4)

Methodology

Phase I: Introduction of *tau-GFP* reporter gene into *Lhx1* locus by gene targeting using *Lhx1* replacement vector and embryonic stem cell technology

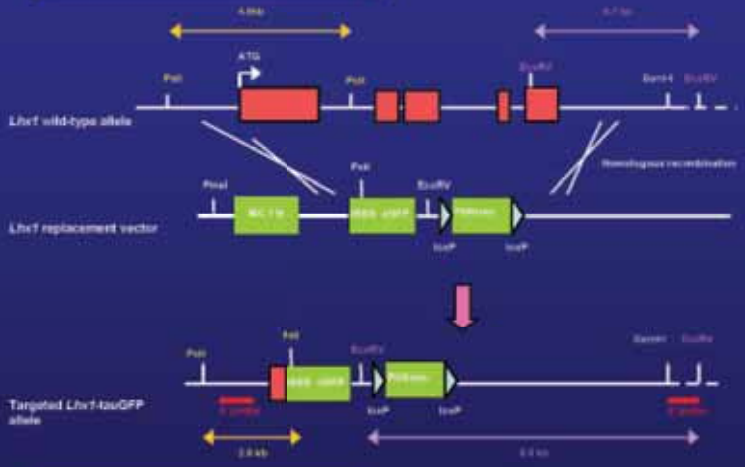

Figure 5. *Lhx1-LacZ* reporter gene expression resembles endogenous *Lhx1* expression as shown by beta-galactosidase staining of postnatal mouse cerebellum. ML: Molecular layer; PC: Purkinje neuron layer; GL: Granule cell layer

Phase II: Production of heterozygous *Lhx1-tauGFP* transgenic mice through embryonic stem cell technology

Phase III: Visualization of *Lhx1-tauGFP* expressing Purkinje neurons in fresh mouse cerebellum by fluorescence microscopy

Future prospects

The *Lhx1-tauGFP* transgenic mouse will be useful in studying *Lhx1* functions in mice *in vivo*, as *Lhx1* has been shown to play essential roles in the specification of different tissues and different organogeneses

References

1. Callahan, C. and Thomas, J. (1994) Tau-b-galactosidase, an axon-targeted fusion protein. *PNAS* 91: 5972 – 5976
2. Fujii, T., Pichel, J.G., Taira, M., Toyama, R., Dawid, I.B. and Kikuchi, H. (1994) Expression patterns of the murine LIM class homeobox gene lim1 in the developing brain and excretory system. *Developmental dynamics* 199: 73 – 83
3. Kania, A., Jonsson, B.G. and Jessell, T.M. (2000) Coordinate roles for LIM homeobox genes in directing the dorsoventral trajectory of motor axons in the vertebrate limb. *Cell* 102: 161-173
4. Lein et al (2007) *Nature* 445:168
5. Li, Y., Dudek, S.S., Geng, J.M., Stawicki, W. and Behringer, R.R. (1999) Sequence and genomic organization of the mouse Lim1 gene. *Mammalian genome* 10: 444-448
6. Shawlot, W. and Behringer, R.R. (1995) Requirement for Lim1 in head-organizer function. *Nature* 374: 425 – 430
7. Zhao, Y., Kwan, K.M., Mailloux, C.M., Lee, W.K., Grinberg, A., Wurst, W., Behringer, R.R. and Westphal, H. (2007) LIM-homeodomain proteins Lhx1 and Lhx5, and their cofactor Ldb1, control Purkinje cell differentiation in the developing cerebellum. *PNAS* 104: 12442 – 12447

PHANG Tsui Hung Supervisor: Prof. LAM Hon Ming
Department of Biology, Faculty of Science

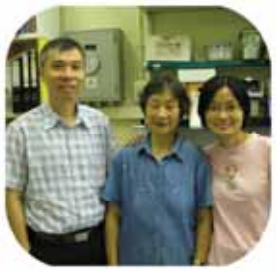

Project Title "High external phosphate (Pi) increases sodium (Na+) ion uptake and reduces salt tolerance of soybean"

High external phosphate (Pi) increases sodium (Na^+) ion uptake and reduces salt tolerance of soybean

PHANG Tsui-Hung[1] SHAO Guihua[1,2] LIAO Hong[3] YAN Xiaolong[3] LAM Hon-Ming[1]

[1] Department of Biology and State (China) Key Laboratory for Agrobiotechnology, The Chinese University of Hong Kong
[2] Institute of Crop Breeding and Cultivation, The Chinese Academy of Agricultural Sciences, Beijing 100081, China
[3] Laboratory of Plant Nutritional Genetics, South China Agricultural University, Guangzhou 510642, China

Aim of study:

Study the interaction between external Pi and Na^+ ions (major salt components in saline croplands) in soybean.

Hypothesis:

External Pi can affect the salt tolerance of soybeans by increasing Na^+ ion uptake.

Project significances:

Address the complicated interactions of ions in soil and provide scientific background for practicing soybean cultivation in saline croplands, which is essential for the enhancement of crop production and promotion of food security.

Research strategy:

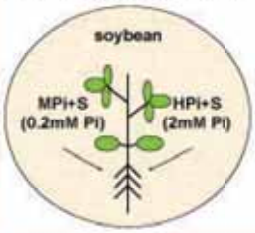

Comparative studies (include phenotypic, physiological and cellular studies) between soybean plants treated in 150mM NaCl (+S) condition supplemented with 0.2mM Pi (MPi) or 2mM Pi (HPi)

Major finding 1:

High external Pi could exacerbate the salt damage and reduce the salt tolerance of soybean.

Fig. 1: Performance of soybean plants (5 days after treatment)

Major finding 2:

High external Pi increases the net sodium uptake, but not phosphorus accumulation, in soybean plants.

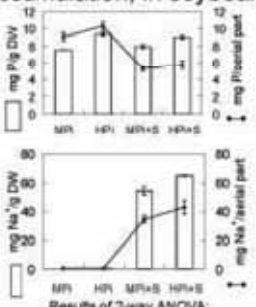

Results of 2-way ANOVA:

Parameter	mg Pi/g Dry weight	mg Pi/aerial part	mg Na^+/g Dry weight	mg Na^+/aerial part
NaCl	p = 0.72	p < 0.001	p < 0.001	p < 0.001
Pi	p < 0.001	p < 0.05	p < 0.001	p < 0.15
NaCl x Pi	p = 0.11	p = 0.57	p < 0.001	p < 0.05

Fig. 2: Effect of high external Pi on the sodium and phosphorus contents, in soybean plants. (N=6; Error bar ± S.E.)

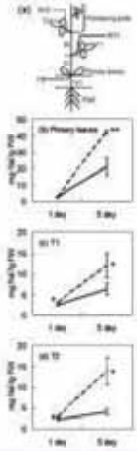

Fig. 3: Effect of high external Pi on the distribution of soluble sodium in different parts of soybean plants. There is no significant difference between sodium concentration in other parts of soybean plants treated in MPi+S or HPi+S (* < 0.05; ** < 0.01; *** < 0.001; N=6; Error bar ± S.E.)

Major finding 3:

Root is the principle site of the interaction between external Pi and salinity.

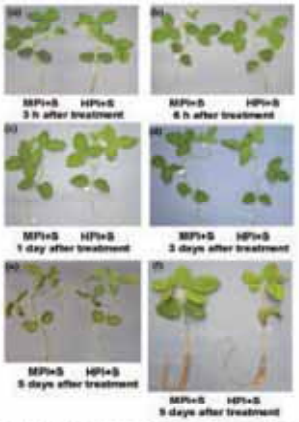

Fig. 4: High external Pi does not reduce the salt tolerance of de-rooted soybean plants.

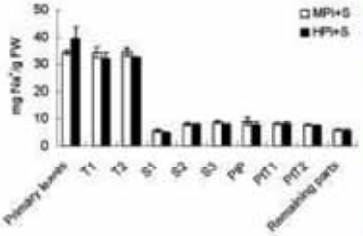

Fig. 5: High external Pi does not change the concentration of soluble Na^+ in different parts of de-rooted soybean plants. (Independent Student's *t* test result: ns, non-significant difference; N=8; Error bar ± S.E.)

Major finding 4:

High external Pi can increase the net Na^+ uptake and aggravate damaging effects in plant cells subjected to Na^+ stress.

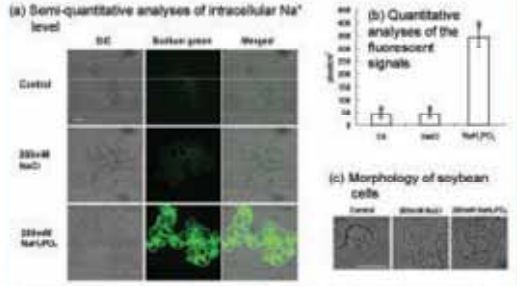

Figure 6: Effect of high external Pi on (a, b) the Na^+ uptake and (c) the morphology of soybean suspension cells under Na^+ stress for 1 day. (a) The signal of Sodium Green indicator increases when the level of intracellular Na^+ increases. (b) Treatment indicating with different letters belonged to different groups ($p < 0.05$). Error bar ± S.E. N=10. DIC: Differential interference contrast. Scale bar = 50 μm.

Remarks: Similar results was obtained in tobacco BY-2 cells.

Acknowledgements: The authors thank Dr. LIN TY (National Tsinghua U, Taiwan) for supplying the soybean suspension cells. This work was supported by the Hong Kong RGC Earmarked Grant CUHK4434/04M and the Hong Kong UGC AoE Plant & Agricultural Biotechnology Project AoE-B-07/09 (to LAM HM).

Modulatory effects of tryptanthrin on the murine myeloid leukemia cells

A 04

Chan H.L. and Leung K.N.
Department of Biochemistry, The Chinese University of Hong Kong, Shatin, N.T., Hong Kong, China Email: avischan8@hotmail.com Tel: (852) 26098026

Introduction:

Conventional treatments against leukemia often cause severe adverse side effects, hence there has been an increasing interest on the development of novel tactics for leukemia treatments. Tryptanthrin (6,12-dihydro-6,12-dioxoindolo-(2,1-b)-quinazoline) is a naturally-occurring, weakly basic alkaloid isolated from a number of medicinal indigo plants, including *Polygonium tinctorium*, *Isatis tinctoria* and *Strobilanthes cusia* (Figure 1). It has been reported to have various biological and pharmacological activities, such as anti-microbial, anti-inflammatory, anti-allergic and anti-tumor effects. However, its modulatory effects and action mechanisms on leukemia cells remain poorly understood. In this study, tryptanthrin was examined for its modulatory effects on the proliferation, differentiation and apoptosis of the murine myeloid leukemia WEHI-3B JCS cells.

Methodology & Results:

1. The [^{3}H]-TdR incorporation assay showed that tryptanthrin exerted a potent antiproliferative effect on the murine myeloid leukemia WEHI-3B JCS cells in a dose-dependent manner (Figure 2) and caused no significant cytotoxic effect on normal murine peritoneal macrophages as measured by the MTT reduction test (Figure 3).
2. Tryptanthrin induced apoptosis of the WEHI-3B JCS cells in a dose- and time-dependent (Figure 4) manner, as evidenced by the formation of apoptotic DNA fragments and further supported by the change of membrane integrity by using Annexin V and propidium iodide staining (Figure 5).
3. Detection of the mitochondrial membrane depolarization by using JC-1 staining (Figure 6) suggested that apoptosis of WEHI-3B JCS caused by tryptanthrin may be mediated by the mitochondrial dependent pathway.
4. Mechanistic studies on the caspase 3 activity (Figure 7) demonstrated that apoptosis of WEHI-3B JCS induced by tryptanthrin was caspase-3 dependent.
5. Cell cycle analysis by flow cytometry indicated that tryptanthrin caused a G_2/G_1 phase arrest in the treated cells in a dose-dependent manner (Figure 8).
6. Gene expression studies by RT-PCR showed that tryptanthrin could down-regulate the expression of *cyclin A*, *cyclin* D_1, *Cdk 4*, *Cdk 6*, *Bcl-2*, *Bcl-*x_L genes but up-regulated the expression of *Bax* and *Bad* genes at 24 h of treatment (Figure 9).
7. Tryptanthrin was capable of inducing morphological differentiation in JCS cells, as shown by a decrease in the nucleus-to-cytoplasm ratio, an increase in cellular granularity, and an enlargement of the cells (Figure 10).

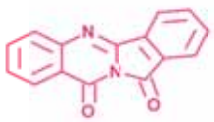

Figure 1. The chemical structure of tryptanthrin (6,12-dihydro-6,12-dioxoindolo-(2,1-b)-quinazoline)

Figure 2. Anti-proliferative effect of tryptanthrin on murine myeloid leukemia WEHI-3B JCS cells. JCS cells were incubated with different concentrations of tryptanthrin for 48 h. Cultures were then pulsed with 0.5 μCi of [^{3}H]-TdR for 6 h before harvest. Results were expressed as % inhibition of [^{3}H]-TdR incorporation, using the solvent treated cells as a control.

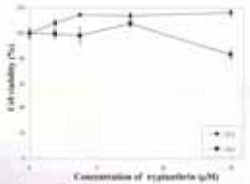

Figure 3. Effect of tryptanthrin on the viability of murine peritoneal macrophages *in vitro*. Murine peritoneal macrophages were incubated with different concentrations of tryptanthrin for 24 and 48 h. MTT was added to the cultures and incubated for 2 h. The blue formazan product formed was solubilized with DMSO. The absorbance was measured. Results were expressed as % decrease in absorbance measured at 540 nm, using solvent treated cells as a control.

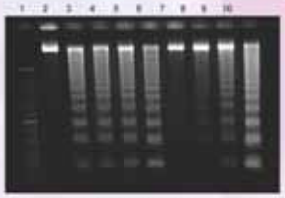

Lane 1: 100 bp DNA marker
Lane 2: Solvent control (0.05% DMSO)
Lane 3: Treated with 1 μM of tryptanthrin for 48 h
Lane 4: Treated with 1.5 μM of tryptanthrin for 48 h
Lane 5: Treated with 2.5 μM of tryptanthrin for 48 h
Lane 6: Treated with 5 μM of tryptanthrin for 48 h
Lane 7: Treated with 1 μM of tryptanthrin for 24 h
Lane 8: Treated with 1.5 μM of tryptanthrin for 24 h
Lane 9: Treated with 2.5 μM of tryptanthrin for 24 h
Lane 10: Treated with 5 μM of tryptanthrin for 24 h

Figure 4. Induction of DNA fragmentation in tryptanthrin-treated WEHI-3B JCS cells. JCS cells were incubated with different concentrations of tryptanthrin for 24 and 48 h. Apoptotic DNA fragments were isolated by mild detergent IGEPAL CA-630 lysis buffer, and were analyzed by electrophoresis on 2% agarose gel stained with ethidium bromide.

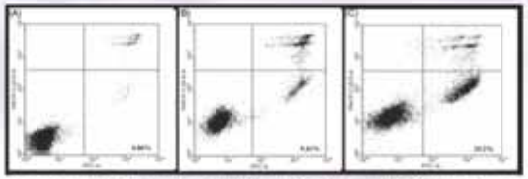

Figure 5. Induction of apoptosis in WEHI-3B JCS cells as measured by Annexin V and PI staining. JCS cells were incubated with (A) solvent control (0.05% DMSO), or tryptanthrin: (B) 1.5 μM, (C) 5 μM for 48 h and then stained with the FITC-conjugated Annexin V and propidium iodide (PI).

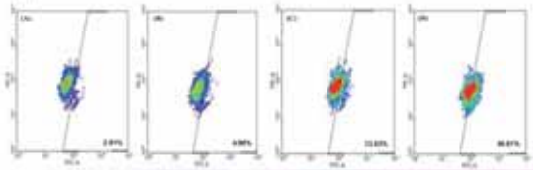

Figure 6. Effect of tryptanthrin on the mitochondrial membrane depolarization in WEHI-3B JCS cells. JCS cells were incubated with (A) solvent control (0.05% DMSO), or tryptanthrin: (B) 1 μM, (C) 2.5 μM, (D) 5 μM for 18 h and then stained with the mitochondria-selective JC-1 dye.

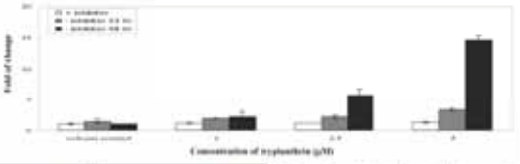

Figure 7. Effect of tryptanthrin on the induction of caspase-3 activity in WEHI-3B JCS cells. JCS cells were either incubated with solvent control (0.05% DMSO) or treated with different concentrations of tryptanthrin for 24 and 48 h. Protein samples were extracted and added the specific substrate with or without its specific inhibitor. The fluorescence intensity was then measured.

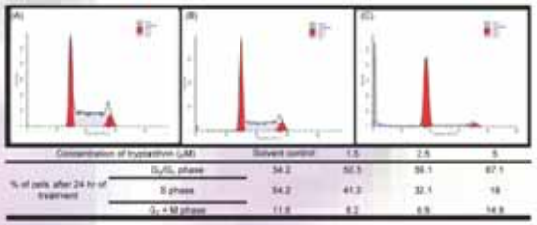

% of cells after 24 hr of treatment	Concentration of tryptanthrin (μM)	Solvent control	1.5	2.5	5
	G_0/G_1 phase	54.2	52.5	56.1	67.1
	S phase	34.2	41.3	32.1	18
	G_2 + M phase	11.6	6.2	8.9	14.9

Figure 8. Effect of tryptanthrin on cell cycle distribution of WEHI-3B JCS cells. JCS cells were incubated with different concentrations of tryptanthrin for 24 h. The DNA was stained with propidium iodide and the fluorescent intensity was analyzed with a flow cytometer. (A) JCS cells treated with 0.05% of solvent DMSO for 24 h; (B) JCS cells treated with 1.5 μM of tryptanthrin for 24 h; (C) JCS cells treated with 5 μM of tryptanthrin for 24 h.

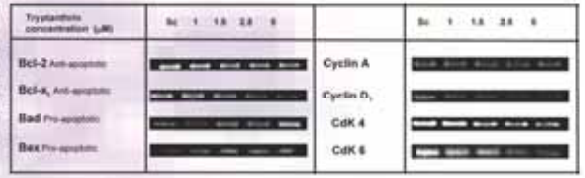

Tryptanthrin concentration (μM): 0 (Sc) 1 1.5 2.5 5

Bcl-2 Anti-apoptotic
Bcl-x_L Anti-apoptotic
Bad Pro-apoptotic
Bax Pro-apoptotic
Cyclin A
Cyclin D_1
CdK 4
CdK 6

Figure 9. Effect of tryptanthrin on the gene expression of Bcl family and cell cycle proteins of WEHI-3B JCS cells. JCS cells were incubated with solvent control (0.05% DMSO) or treated with different concentrations of tryptanthrin for 24 h. Total RNA were extracted by using TRIZOL reagent. Semi-quantitative RT-PCR was performed and the PCR products were separated on 2 % agarose gel.

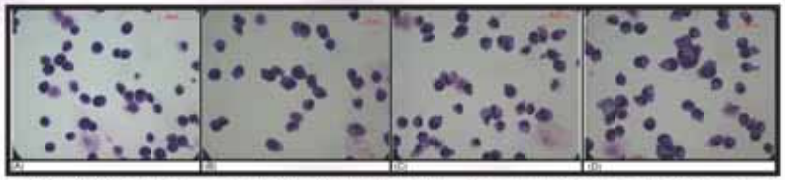

Figure 10. Morphological changes in tryptanthrin-treated WEHI-3B JCS cells. JCS cells were incubated with different concentrations of tryptanthrin for 48 h. The cells were cytocentrifuged and stained with hemacolor staining solutions. JCS cells were cultured in (A) 0.05% DMSO; (B) 1.5 μM of tryptanthrin; (C) 2.5 μM of tryptanthrin; and (D) 5 μM of tryptanthrin.

Conclusions:

In this study, the murine myeloid leukemia WEHI-3B JCS cells were used as the leukemia cell model. Tryptanthrin was shown to exhibit potent anti-leukemia effect in a dose- and time-dependent manner. The anti-proliferative effect could be resulted from the induction of apoptosis and differentiation. Tryptanthrin triggered apoptosis in the JCS cells, as evidenced by the induction of DNA fragmentation, phosphatidylserine externalization, and mitochondrial membrane depolarization after tryptanthrin treatment. A time- and dose-dependent activation of caspase 3 activity was also observed in tryptanthrin-treated JCS cells. Flow cytometric analysis of the tryptanthrin-treated JCS cells showed an obvious cell cycle arrest at the G0/G1 phase. The expression of cyclin A, cyclin D1, Cdk 4 and Cdk 6 genes in JCS cells was found to be down-regulated at 24 h as measured by RT-PCR. Moreover, Further mechanistic studies showed that tryptanthrin treatment up-regulated the expression of pro-apoptotic Bax and Bad genes but down-regulated the anti-apoptotic Bcl-2 and Bcl-xL genes in JCS cells. Interestingly, morphological and flow cytometric studies revealed that tryptanthrin induced the differentiation in JCS cells, as indicated by the increases in vacuolization, cell size and granularity. Therefore, tryptanthrin isolated from Chinese herbs (Indigo plants) can be a potential candidate drug for the treatment of some forms of leukemia, which will probably have fewer side effects and be more affordable for the leukemia patients.

CHAN Hoi Ling Supervisor: Prof. LEUNG Kwok Nam
Department of Biochemistry, Faculty of Science

Project Title "Modulatory effect of tryptanthrin on the murine myeloid leukemia cells"

Student Poster

DEVELOPMENTAL EXPRESSION OF Ca^{2+}-PERMEABLE AMPARs UNDERLIES DEPOLARIZATION-INDUCED LTD (DiLTD) AT MOSSY FIBER-CA3 PYRAMID SYNAPSES

M.T. Ho[1,3*], K.A. Pelkey[1], L. Topolnik[4], R.S.Petralia[2], K.Takamiya[5], J.Xia[5], R.L. Huganir[5], J-C Lacaille[4], and C.J. McBain[1]

[1] NICHD, NIH, Bethesda, MD; [2]NIDCD, NIH, Bethesda,MD; [3]Dept of Biochemistry, CUHK, HK; [4]Dépt de Physiologie UM, Montréal, Québec; [5]Dept. of Neuroscience,JHU, Baltimore, MD

Summary and conclusions:

Emerging evidence indicates that GluR2-lacking, Ca^{2+}-permeable (CP)-AMPARs may be synaptically expressed by principal neurons early in development. Moreover, GluR1 homomeric AMPARs overexpressed in slice culture are constitutively inserted at mossy fiber (MF)-CA3 pyramid (PYR) synapses, but excluded from collateral fiber-PYR synapses unless driven by CaMKII activity. These observations prompted us to investigate whether endogenous CP-AMPARs exist at developing MF-PYR synapses. In immature mouse hippocampal slices (P10-17) CP-AMPARs contributed significantly to MF-PYR transmission as revealed by inwardly rectifying I-V relations (rectification index=Rin0.5/Rin30, 0.6±0.05, n=13) obtained with spermine in the recording pipette (no spermine controls, Rin=0.9/Rin30.08, n=7). EPSCs were blocked by GYKI53655 eliminating potential KAR contribution to the rectification. Additionally, philanthotoxin reduced EPSCs to 73 ± 4.9% of control (n=16), confirming the presence of CP-AMPARs at immature MF-PYR synapses. In contrast, MF-PYR EPSCs in slices from older animals (~P26) had near linear I-Vs (Rin=0.8±0.06, n=16) consistent with prior observations. Additionally, CP-AMPAR mediated CaT_s were observed at immature MF-PYRs, further supporting the presence of CP-AMPARs at immature MF-PYR synapses. The developmental window of CP-AMPAR expression is reminiscent of the period during which MF-PYR synapses express DiLTD. Thus, we examined whether CP-AMPARs participate in this postsynaptically expressed form of plasticity. In slices from young mice PYR depolarization (from -60 to -10mV) for 5' produced robust DiLTD: 15' post-induction EPSCs were 63.3±3.4% of control responses (n=28). Interestingly, postsynaptic CP-AMPAR-mediated Ca^{2+} transients (CaT_s) at MF–PYR contacts in acute hippocampal slices were also depressed to 8.5 ± 3.4% of baseline responses after DiLTD induction. In a subset of these recordings the ~40-60mV EPSC ratio was examined and found to increase by 57.0±16.2% after DiLTD induction in blocking a decreased contribution of CP-AMPARs at depressed synapses (n=8). Furthermore, DiLTD was absent in young PICK1$^{-/-}$ mice (EPSCs were 97±6.9% of control 15' after induction, n=10) consistent with reports of deficient CP-AMPAR plasticity after disruption of PICK1-GluR2 interactions in cerebellar stellate cells. Interestingly, young PICK1$^{-/-}$ mice exhibited linear I-V relations (Rin=0.84±0.08, n=11) perhaps explaining the absence of DiLTD. We propose that the developmental window of CP-AMPARs expression at MF-PYR synapses dictates the critical period for observing DiLTD.

Figure 1. Developmental expression of CP-AMPARs at MF-PYR synapses

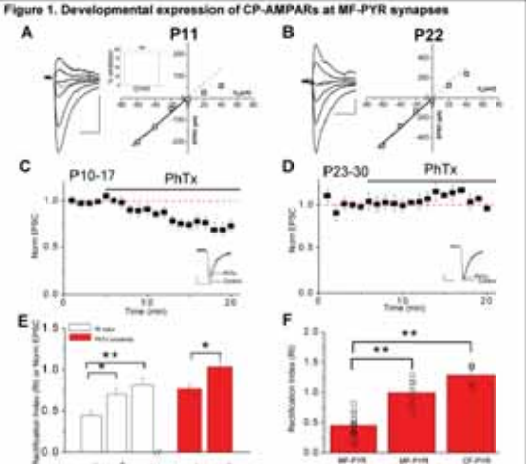

A,B Comparison of MF-PYR EPSC I-V relations (V_{cmd} from -60 to +40mV in steps of 20 mV) from young (**A**) and old mice (**B**) reveals inwardly rectifying responses in slices from young animals. **Inset A** GYKI53655 sensitivity of MF-PYR recordings in young mice reveals that synaptic events are primarily AMPAR-mediated. Traces in **A,B** are from representative recordings (average of 5-10 events per holding potential). Solid lines represent the linear fit to data points between -60 and 0 mV holding potentials. Dotted line extends this fit to highlight the deviation of the I-V relationship from linearity. **C,D** Normalized group data for recordings in which the effects of PhTx (2microM) were examined on MF-PYR transmission in slices from young (**C**, n=16), and old mice (**D**, n=4). Traces are from representative recordings (bars 100pA/10ms for **A-D**). **E** Summary histogram illustrating the average Ri values for, and effects of PhTx on, MF-PYR transmission for the indicated age ranges. PhTx data are expressed as the average EPSC amplitude at the end of PhTx treatment, normalized to the average EPSC amplitude obtained immediately preceding PhTx application and are from the recording in C and D. Ris plotted in **E and F** were calculated as the ratio of the actual current amplitude at +40 mV to the predicted linear value at -40 mV as determined by a linear fit of I-V relations for points between -90 to -5 mV holding potential. **F** Bar graph summary comparing the Ris from P10-P17 young mouse for MF-PYR (n=13), CF-CA3 (n=5), and in no spermine control (n=7). Error bars indicate SEM. Here and throughout, *p<0.05 and **p<0.01).

Figure 2. CP-AMPARs mediate CaT_s at developing MF-PYRs synapses

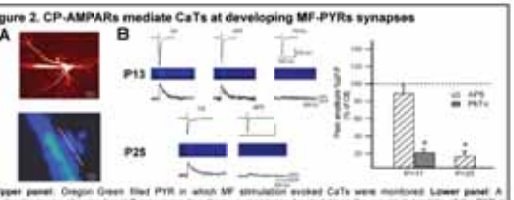

A Upper panel: Oregon Green filled PYR in which MF stimulation evoked CaT_s were monitored. **Lower panel**: A pseudocolor image showing basal fluorescence in a thorny excrescence located along the proximal dendrite of the PYR in the upper panel (arrow). Position of line scan used to monitor stimulus evoked Ca^{2+} signals was marked. **B** Representative recording from a P13 rat showing the effects of D-APS (50microM) and PhTx (2microM) on stimulus evoked CaT_s recorded in a thorny excrescence and simultaneously monitored EPSCs (top traces, average of 4 consecutive events under each condition). Representative recording from a P23 rat showing the effects of D-AP5 on stimulus evoked CaT_s and simultaneously monitored EPSCs. **B right panel**: Summary histogram for group data examining the effects of D-AP5 and PhTx on stimulus-evoked CaT_s in thorny excrescences from young rats (n=5) and of D-AP5 on CaT_s in old rats (n=4). Data are expressed as percentage of control responses that were obtained before any drug treatment. Error bars indicate SEM. Here and throughout, *p<0.05 and **p<0.01).

Figure 3. Developmental expression of DiLTD

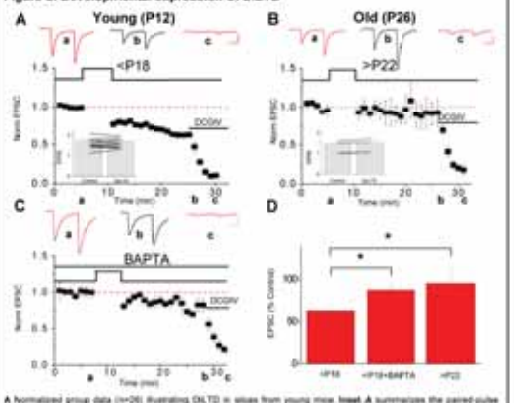

A Normalized group data (n=26) illustrating DiLTD in slices from young mice. **Inset A** summarizes the paired-pulse ratios (PPR) obtained before and after DiLTD induction for a subset of the recordings. Traces above in **A** (and throughout) are the average of 20 consecutive EPSC pairs (20 Hz) obtained at the times indicated (bars 100pA/20ms). Basal stimulation rate was 0.33Hz (except during induction when stimulation is paused) and all experiments are carried out in DL-APS (50-100 microM) to isolate the non-NMDAR-mediated component of EPSCs. Sensitivity of synaptic events to DCGIV (1microM) confirms that inputs are mossy fiber in origin. **B** Normalized group data (n>4 for each time point) for recordings in which the DiLTD induction protocol was attempted in slices from old mice (>P22). **Inset B** summarizes the paired-pulse ratios (PPR) obtained before and after DiLTD induction for a subset of the recordings. **C** Normalized group data for recordings in which the DiLTD induction protocol was attempted in slices from young mice (<P18) in the presence of calcium chelator BAPTA (20mM). **D** Bar graph summary comparing DiLTD for interleaved recordings from young, old mice and young mice in the presence of BAPTA. Data represent EPSC amplitude measured at 15 minutes post-induction expressed as a percentage of control responses obtained prior to induction (*p<0.05 for indicated comparison).

Figure 4. DiLTD results in a loss of postsynaptic MF-PYR CaT_s

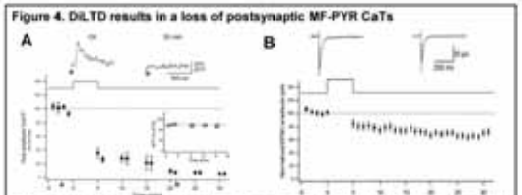

A Group data time course plot for experiments in which stimulus evoked CaT_s were continuously monitored before and after the DiLTD induction protocol (time, 0 min) was applied (black, n=5). CaT_s (average of 4 events) were monitored at regular intervals during the recordings and expressed as percentage of control CaT_s obtained during the baseline recording period. The traces above are CaT_s obtained at the times indicated from a representative recording that was subject to the DiLTD induction protocol. **Inset A** time course plot summarizes control recordings in which stimulation was interrupted but PYRs were not subject to depolarization (n =3). **B** Group data time course plot showing DiLTD of EPSCs that were recorded during CaT monitoring. The traces above are EPSC obtained at the times indicated from the same recording in A. Error bars indicate SEM.

Figure 5. The GluR2 content of MF-CA3 PYR synapses changes with DiLTD.

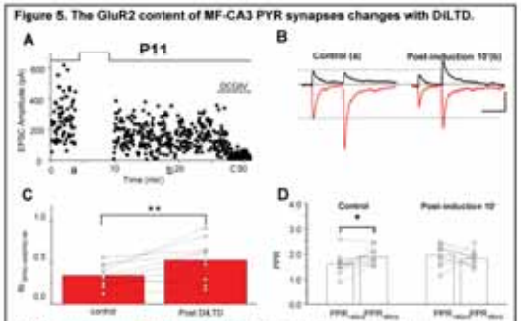

A,B,C Representative recording (**A**), sample traces (**B**) and group data (**C**, n= 6) revealing changes in Ri associated with DiLTD induction in slices from young mice (<P17). **D** PPR at +40mV and -60mV before and postinduction of DiLTD (PPR at +40mV compared with PPR at -60mV). For these experiments Ri values before and after DiLTD induction (10-15 minutes) were determined as the ratio of response amplitudes at +40 and -60 mV (minimum of 5 responses obtained at each holding potential and averaged, e.g. traces in **B**, bars 100pA/50ms. *p<0.05, **p<0.01).

Figure 6. Disruption of PICK1 inhibits DiLTD

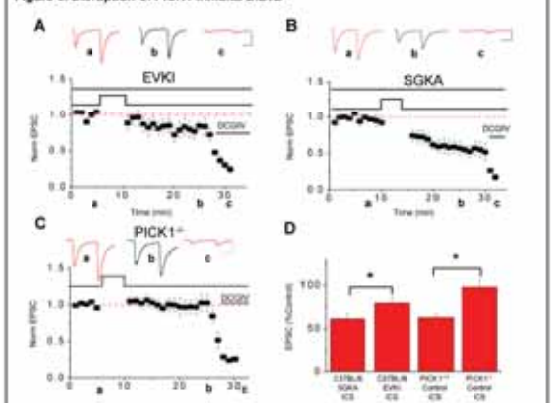

A Postsynaptic application of a peptide (EVKI) that specifically disrupts GluR2-PICK1 interactions inhibits DiLTD of MF-CA3 transmission (**A**, n=5), while a control peptide (SGKA) does not affect DiLTD (**B**, n=5). **C** Group data (post DiLTD 15' n=10) for MF-CA3 recordings performed in PICK1$^{-/-}$ hippocampal slices. **D** Summary bar graph comparing DiLTD for the conditions indicated and the level of inhibition after DiLTD induction for PICK1$^{+/+}$ (n=4) and PICK1$^{-/-}$ littermates (n=10) (*p<0.05 for indicated comparison). Data represent EPSC amplitude measured at 15 minutes post-induction expressed as a percentage of control responses obtained prior to induction.

Figure 7. Loss of CP-AMPARs at developing MF-PYR synapses after PICK1 disruption

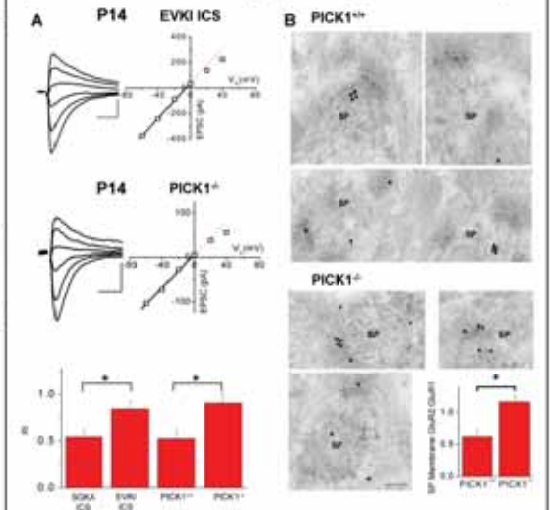

A Upper panel MF–PYR EPSC I-V relationship (V_{cmd} from -60 to+40mV in steps of 20 mV) obtained during a representative recording on a slice from young C57BL/6 mouse using EVKI-containing ICS. The line is the linear fit to data points for holding potentials between -60 and 0 mV. **Middle panel** The traces are the average of 5–10 events at each holding potential (Bars 100 pA,10 ms). Representative MF–PYR EPSC I-V relationship obtained in a slice from young PICK1$^{-/-}$ mouse (Bars, 50 pA,10 ms). **Lower panel** Group data summary bar chart for Ri values obtained in slices from C57BL/6 mice aged P12 –P17 using ICS supplemented with EVKI (n=5) or SGKA (n=5). Also shown is the group data summary bar chart of Ri values obtained in P10 –P17 PICK1$^{-/-}$ (n=11) and PICK1$^{+/+}$ (n=5) mice. Error bars indicate SEM. **B** Representative photomicrographs of immunogold labeling in PYR spine profiles (SPs) for GluR1 (5 nm gold particles) and GluR2 (15 nm gold particles) in PICK1$^{+/+}$ mice (top panel; three micrographs showing 4 SPs) and PICK1$^{-/-}$ mice (bottom left panel; 3 micrographs each with 1 SP). The bottom right panel is a histogram (bin width, 0.1) of GluR2/GluR1 signal ratios in SP membranes of PICK1$^{+/+}$ mice (n=87 SPs from 3 animals) and PICK1$^{-/-}$ mice (n=66 SPs from 3 animals). Scale bar (bottom left photomicrograph), 100 nm. *p<0.05 throughout the figure.

Support contributed by an NIH/NICHD intramural award to Dr. CJ McBain, as well as NIH extramural and HHMI awards to Dr. RL Huganir.

HO Tsz Wan Michelle

Department of Biochemistry, Faculty of Science

Supervisor: Prof. Chris J. McBain

Prof. SHAW Pang Chui

Project Title "Developmental expression of Ca2+-permeable AMPARs underlies depolarization-induced LTD (DiLTD) at mossy fiber-CA3 pyramid synapses"

Student Poster

LEUNG Ka Kit **Supervisor: Prof. TSUI Kwok Wing**
Department of Biochemistry, Faculty of Science

Project Title "Whole-genome sequencing and analysis of polymorphisms in an extensively drug resistant (XDR) strain of Mycobacterium tuberculosis W/Beijing isolate"

Whole-Genome Sequencing & Analysis of Polymorphisms in an eXtensively Drug Resistant (XDR) strain of Mycobacterium tuberculosis W/Beijing Isolate

Ka-Kit Leung [1,2], Ting-Fung Chan [1,2], Patrick Tik-Wan Law [3], Wendy Yin-Wan Fung [3], Kwok-Pui Fung [1,2], Hoi-Shan Kwan [4], Shao-ke Lou [1,2], Kai-Man Kam [5], Raphael Chiu-Yeung Chan [6] and Stephen Kwok-Wing Tsui [1,2].
[1] Department of Biochemistry, [2] Hong Kong Bioinformatics Center, [3] Faculty of Science, [4] Department of Biology, [6] Department of Microbiology, The Chinese University of Hong Kong, [5] Tuberculosis Reference Laboratory, Public Health Laboratory Center, Department of Health, Hong Kong

Background

Tuberculosis statistics in 2006

	World	China	HK
Prevalence	14,415,397	2,658,377	5,856
Death	1,654,805	200,820	294
Drug resistance	2,500	<1,250	N/A

A single sneeze can release up to 40,000 (less in cough) droplets. Each one of these droplets may transmit the disease, since the infectious dose of tuberculosis is very low (a single bacterium). Spit, speak, or kiss can also transmit if infectious phlegm is present.

Materials & Methods

Bacterial genome get sequenced in days with reduced cost and manpower

```
Reference sequence:     4351463+ TCCC-GG-CGTGATCGGGGTTCCCGG-TGTGC

E5KITCJ02GGM04  (2)         287+ TCCC-GGG-GTGATCGGGGTTCCCGGCTGT-C
E5KITCJ02GNW2K  (2)         283+ TCCC-GGG-GTGATCGGGGTTCCCGGCTGT-C
E5KITCJ02I240P  (3)         111- TCCC-GGG-GTGATCGGGGTTCCCGGCTGT-C
E5KITCJ02GG7BP  (3)         104- TCCC-GGG-GTGATCGGGGTTCCCGGCTGT-C
E5KITCJ02GPMM0              122- TCCC-GGG-GTGATCGGGGTTCCCGGCTGT-C
E5KITCJ02JWX29              140- TCCCCGGG-GTGATCGGGGTTCCCGGCTGT-C
                                    *  #                 †   ‡

*: low quality read filtering
#: G to C substitution
†: insertion of C
‡: deletion of G
```

Polymorphism identification

Conclusions

1. Provision of two W/Beijing isolate genomic sequences
2. Identification of an "XDR-specific" set for better understanding of underlying factors and evolvement - accordingly, better deployment on new drug development
3. Analysis on a "Beijing-common" set on its virulence, structure and adaptation, metabolism and regulation-related gene polymorphisms so to devise strategies on disease control and prevention, complementing the line of drug development
4. Establishment of a platform for high-throughput comprehensive comparative genomics studies

Results

Polymorphisms identified solely in XDR that are related to drug resistance

Drug	Genes affected	Synonymy
Streptomycin	*rpsL* *rrs*	K → R A → G (16S rRNA)
Amikacin and Kanamycin	*rrs*	A → G (16S rRNA)
Ofloxacin	*gyrA*	D → H
Capreomycin	*rrs*	A → G (16S rRNA)
Rifampicin	*rpoB*	S → L
Floroquinolones	*gyrA*	D → H
Isoniazid and ethionamide	*MabA*	16 bp upstream of the coding region, C → T
Ethambutol	*embB*	M → V
Pyrazinamide	*pncA*	P → Q

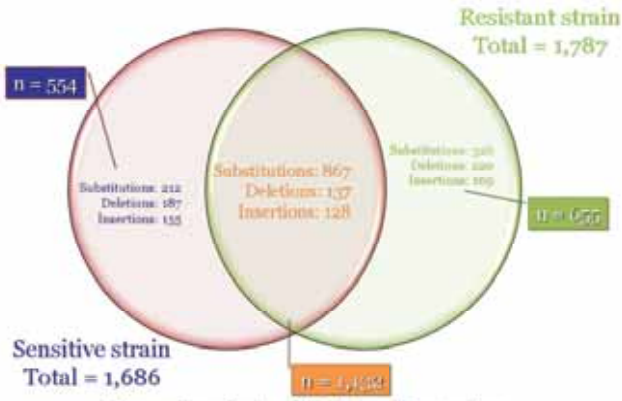

Genomic variants within the coding regions

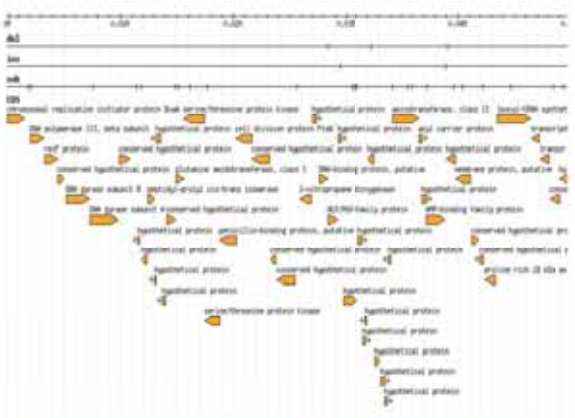

Visualization of analysis result and gene annotation of virulence, structure, adaptation and metabolism

Joint Faculty Research Day 2008

CHAN Wing Man **Supervisor: Prof. Edwin CHAN**
Prof. SHAW Pang Chui

Department of Biochemistry, Faculty of Science

Project Title "The Influence of Protein Nucleocytoplasmic Transport on Expanded Polyglutamine-induced Neurodegeneration"

The Influence of Protein Nucleocytoplasmic Transport on Expanded Polyglutamine-induced Neurodegeneration

The Chinese University of Hong Kong

Wing Man CHAN[1,2], Frankie Ho TSOI[1,3], Pang Chui SHAW[2,3], Ho Yin Edwin CHAN[1,2,3]

1)Laboratory of *Drosophila* Research, 2)Molecular Biotechnology Program, 3) Department of Biochemistry, The Chinese University of Hong Kong, HKSAR, China

Laboratory of Drosophila Research CUHK Est 2002

RESEARCH BACKGROUND:

Features of Polyglutaminopathies:
Neurodegenerative diseases characterized by neuronal dysfunction and cell death

Etiology:
Abnormal expansion of CAG triplet repeat in the disease gene, result in expanded polyglutamine tract in disease protein

Disease Threshold: 35-40 no. of CAG repeats

Hallmark:
Formation of insoluble protein aggregates in both cytoplasm and nucleus

Example: Machado-Joseph disease (MJD/SCA3), Huntington's Disease (HD)

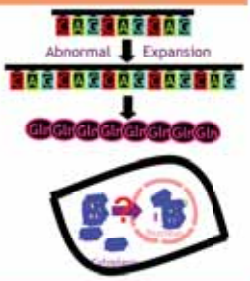

HYPOTHESIS:

The naked expanded polyglutamine (polyQ) domain carries nuclear transport activity; and the perturbation of such activity is closely correlated to toxicity

OBJECTIVES:

To demonstrate the nuclear import activity of expanded polyQ domain by biochemical fractionation and time-lapse live cell microscopy

To investigate the effects of karyopherin nuclear transport receptor family on expanded polyQ protein subcellular localization by RNA interference

To elucidate the effects of select transport receptors on polyQ-induced toxicity *in vivo*

MODEL CHARACTERIZATION:

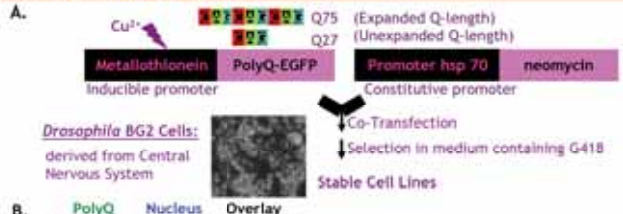

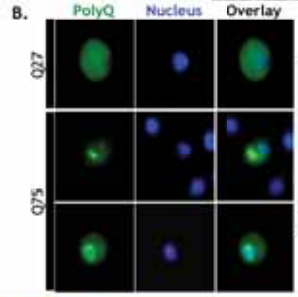

Figure 1: An *in vitro* PolyQ-EGFP model in cultured *Drosophila* cells.

A. Establishment of polyQ model in the *Drosophila* neuronal BG2 cells.

B. Fluorescence microscopy of polyQ-EGFP-expressing cells. The Q27-EGFP protein localized homogeneously in cytoplasm and nucleus; the Q75-EGFP protein formed both cytoplasmic and nuclear aggregates. Scale bar represents 5 μm.

RESULTS:

I) An expanded polyQ domain was able to initiate protein nuclear import in its soluble form

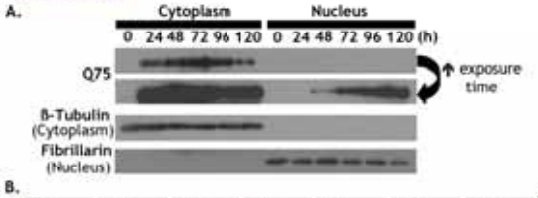

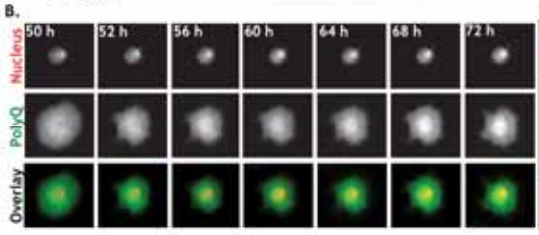

Figure 2. Expanded (Q75) polyQ protein enter into the nucleus in soluble form.

A. Biochemical fractionation of BG2 lysates into nuclear and cytoplasmic fractions at different time post-induction. The SDS-soluble Q75 proteins accumulated in the nucleus in a time-dependent manner.

B. Time-lapse experiment on BG2 cells expressing Q75-EGFP. An enrichment of nuclear fluorescent signal was observed without the formation of microscopically visible aggregates.

II) Members from the karyopherin nuclear transport receptors exert modulatory effects on the subcellular localization of expanded polyQ protein

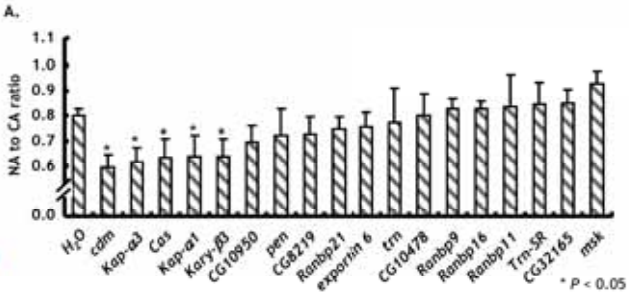

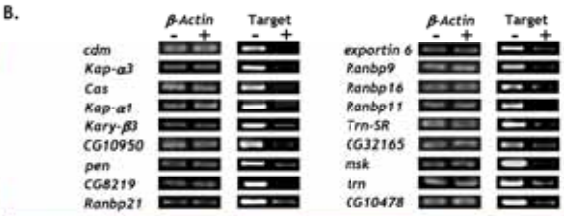

Figure 3. Karyopherin nuclear transporters modulate nucleocytoplasmic localization of expanded polyQ protein.

A. Ratio of nuclear to cytoplasmic Q75-aggregates in water or dsRNA-treated BG2 cells. Knockdown of *cdm*, *Kap-α3*, *Cas*, *Kap-α1* and *Kary-β3* in BG2 cells resulted in significant changes of the NA to CA ratio.

B. The knockdown efficiencies of dsRNAs were confirmed by RT-PCR.

III) Knockdown of *Karyopherin-α3* enhances polyQ-induced toxicity *in vivo*

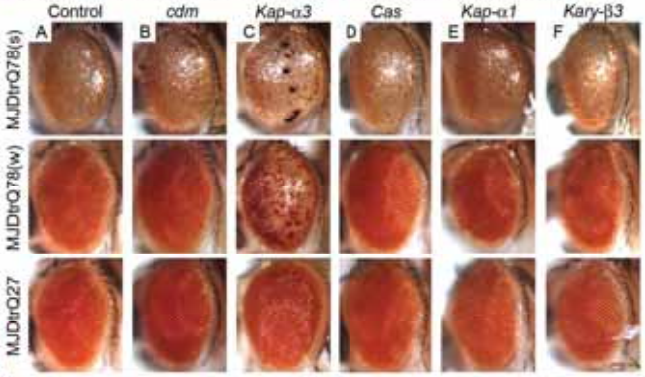

Figure 4. Knockdown of *kap-α3* enhances trMJD-induced toxicity.

Select targets from Figure 3 were knock-downed *in vivo* and their effects were compared to control (A) in MJD *Drosophila* models. Transgene expressions were driven by GMR-Gal4 in eyes. The knockdown of *kap-α3* (C) enhances trMJDQ78-induced toxicity, as revealed by external eye depigmentation (MJDtrQ78w) and scar formation (MJDtrQ78s). There was no dominant phenotype caused by the knockdown of *kap-α3* in flies expressing unexpanded trMJD proteins (MJDtrQ27).

CONCLUSIONS:

- A naked polyQ domain possesses nuclear import activity
- Specific karyopherin nuclear transporters regulate the nucleocytoplasmic localization of expanded polyQ protein, and in particular, karyopherin-α3 also modulates polyQ-induced toxicity *in vivo*

REFERENCES:

Martindale *et al.*, (1998) *Nat Genet* **18**: 150-154.
Xia *et al.*, (2003) *Hum Mol Genet* **13**: 1393-1403.

ACKNOWLEDGEMENT:

This work was supported by a grant from the Research Grants Council of Hong Kong Special Administrative Region, China (Project No. CUHK4413/04M).

LAM Sheung Kwan **Supervisor: Prof. JIANG Liwen**
Molecular Biotechnology Programme, Faculty of Science

Student Poster

Project Title "Molecular characterization of plant endocytosis"

Molecular Characterization of Plant Endocytosis

Sheung Kwan LAM & Liwen JIANG
Department of Biology and Molecular Biotechnology Program, Chinese University of Hong Kong

Plant endocytosis is the internalization of materials from plasma membrane into the cells which governs cell survival and this process remained unknown for decade.
Secretory carrier membrane protein (SCAMP) was used as a tool to study plant endocytosis and protein trafficking in this study.
Major contribution of this study is the identification of *trans*-Golgi network (TGN) as the early endosome in plant cell which revolutionized view of the plant cell trafficking pathways.

SCAMP and SCAMP-YFP were localized on plasma membrane (PM) and cytosolic organelles distinct from Golgi, prevacuolar compartment (PVC) and lytic vacuole (LV).

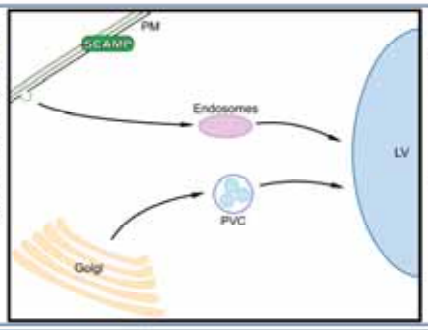

Figure 1. SCAMP-YFP (yellow fluorescent protein) fusion protein localized on plasma membrane (PM) and cytosolic organelles.

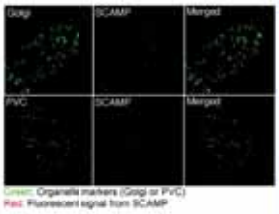

Figure 2. SCAMP positive organelles were not Golgi (upper panel) or prevacuolar compartment (PVC, lower panel).

Internalized endocytic marker FM4-64 reach SCAMP positive organelles prior to PVC.

So SCAMP positive organelles are the early endosome.

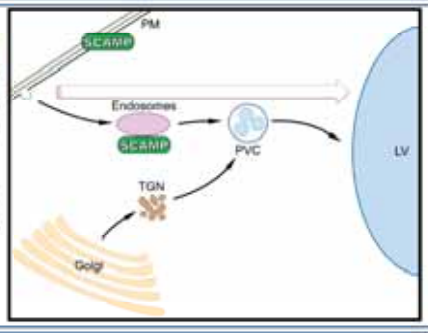

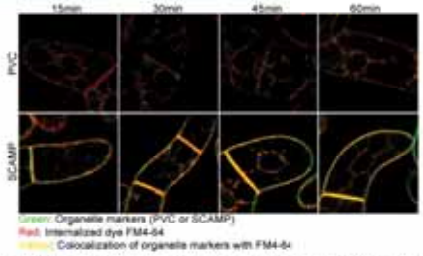

Figure 3. FM4-64 was internalized into transgenic BY-2 cells and reached SCAMP positive organelles prior to PVC.

***trans*-Golgi network (TGN)** is the SCAMP positive organelle.

So TGN merges endocytosis and secretory pathway.

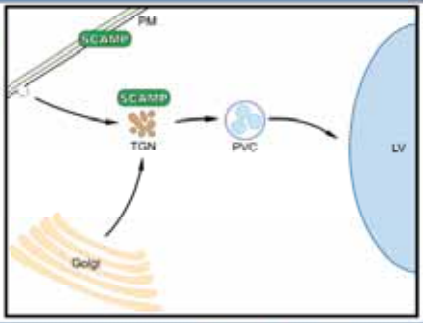

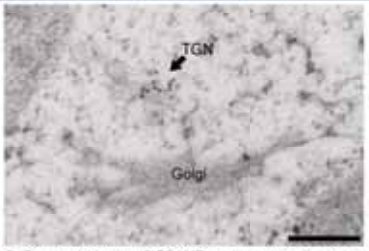

Figure 5. Structural identity of SCAMP positive organelle under electron microscopy. SCAMP proteins (represented by the gold particles pointed by arrow) localized on the *trans*-Golgi network (TGN) which lied adjunct to the Golgi. Scale bar: 200nm.

Significance of this study changes the current view of endocytosis and unites the two previously separated pathways together at the TGN.

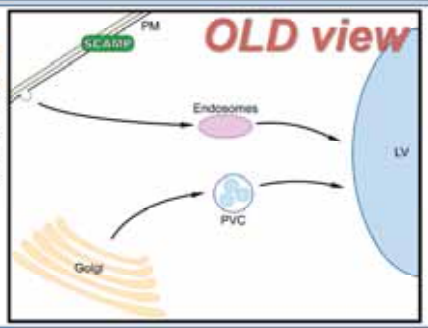

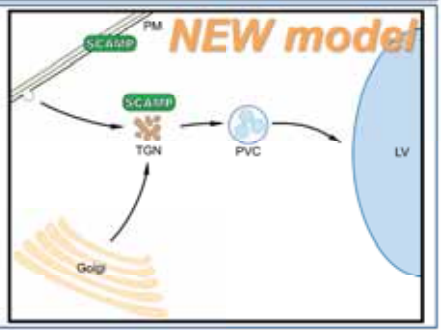

Publications

- **Lam SK, Tse, YC, Jiang L, Oliviusson P, Heinzerling O, and Robinson DG** (2005) Plant Cell Monograph **1:** 37-61
- **Lam SK, Siu CL, Hillmer S, Jang S, An G, Robinson DG and Jiang L** (2007) Plant Cell **19:** 296-319
- **Lam SK, Tse YC, Miao Y, Li HY, Wang J, Lo SW, and Jiang L** (2007) Journal of Integrative Plant Biology **49**: 1119-1128
- **Lam SK, Tse YC, Robinson DG and Jiang L** (2007) Trends in Plant Science **12:** 497-505

Acknowledgement

Supported by Research Grants Council of Hong Kong (CUHK4260/02M and CUHK4580/05M), National Science Foundation of China (30529001) and CUHK Scheme C.

ZHOU Quan **Supervisor: Prof. Ke Qing XIA**
Department of Physics, Faculty of Science

Project Title "Morphological Evolution of Thermal Plumes in Turbulent Rayleigh-Bénard Convection"

Morphological Evolution of Thermal Plumes in Turbulent Rayleigh-Bénard Convection

Quan Zhou, Chao Sun and Ke-Qing Xia
Department of Physics, The Chinese University of Hong Kong, Shatin, Hong Kong, China

Q. Zhou, C. Sun & K.-Q. Xia, Phys. Rev. Lett. 98, 074501 (2007)

Introduction

Turbulent Rayleigh-Bénard convection (RBC) has become a paradigm for many convection phenomena occurring in nature. A prominent feature of turbulence is the ubiquity of coherent structures, such as thermal plumes, which are localized thermal structures having a temperature contrast with the background fluid and generated from the upper and lower thermal boundary layers of the convection cell. There are two different morphologies for plumes observed in RBC. However, our understanding of the nature of plumes remains incomplete.

Mushroomlike plumes viewed from the side, Xi, Lam & Xia, JFM, 2004

Sheetlike plumes observed from above, Funfschilling & Ahlers, PRL, 2004

Experimental Setup

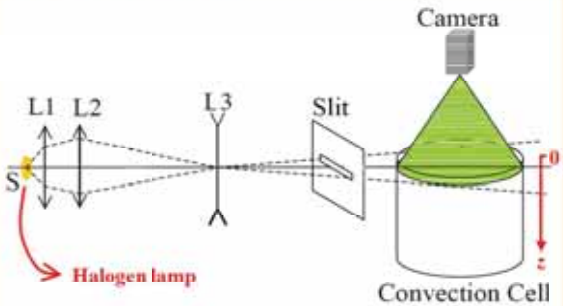

TLC: Thermochromic liquid crystal microspheres with mean diameter 50 μm.

Color:	**Red**	**Green**	**Blue**
Temperature:	**29°C**		**33°C**

Results

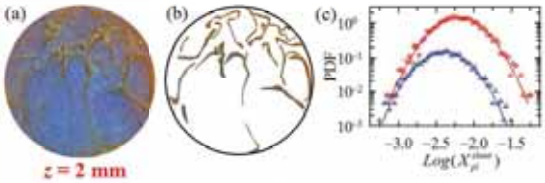

$z = 2$ mm

(a): Sheetlike plumes with the shape of reddish "lines" align mostly in directions perpendicular to the flow.

(b): 25 such sheetlike plumes identified from (a) (background removed).

(c): PDFs of the logarithm of the normalized sheetlike-plume area (red circles) and heat content (blue triangles). Here heat content is the "heat" carried by each plume.

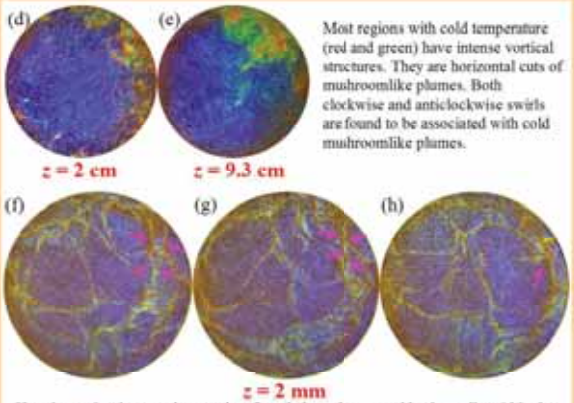

Most regions with cold temperature (red and green) have intense vortical structures. They are horizontal cuts of mushroomlike plumes. Both clockwise and anticlockwise swirls are found to be associated with cold mushroomlike plumes.

Hot plumes impinge on the top plate from below, then spread horizontally within the layer and form sheetlike plumes. As the sheetlike plumes propagate, they collide with each other or with the sidewall to form swirls.

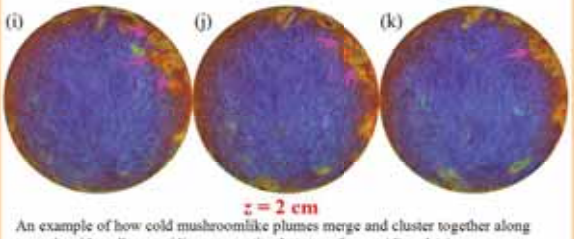

An example of how cold mushroomlike plumes merge and cluster together along opposite sidewalls, providing connection between figures (d) and (e).

Cross-correlation functions between the simultaneously measured temperature and vertical vorticity at three positions. The vertical vorticity is found to have an exponential distribution.

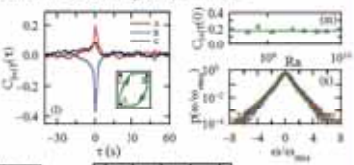

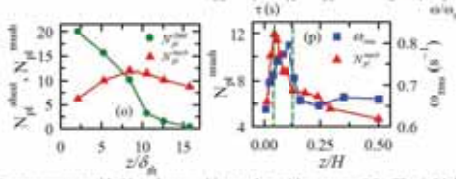

N_{pl}^{sheet} crosses over with N_{pl}^{mush} around its peak position at $z = 8\delta_{th}$. The initial rapid increase of ω_{rms} is seen to correspond to the increase of N_{pl}^{mush} and the decrease of N_{pl}^{sheet}. The vertical dashed lines in figure (p) indicate the region of FWHM of ω_{rms}. In this region N_{pl}^{mush} experiences a steep drop, providing a quantitative measure of the mixing zone in which most of plume mixing, merging, and clustering take place.

Conclusions

- **Plumes have log-normal distributions.**
- **$0 < z < 8\delta_{th}$: sheetlike plumes collide with each other or with the sidewall and form swirls**
- **$8\delta_{th} < z < 0.13H$: mushroomlike plumes mix and group together**
- **Mushroomlike plumes associate with intense vertical vorticity.**

Acknowledgement

This work was supported by the Hong Kong Research Grants Council (Grant No. CUHK 403705) and a CUHK Direct Grant (Project No. 4450088). K.-Q. X. acknowledges the support of the Croucher Foundation of Hong Kong.

Tailoring Surface Plasmonic Properties of Gold Nanorods and Their Assembly

Xiaoshan Kou, Weihai Ni, Zhenhua Sun, Zhi Yang and Jianfang Wang
Department of Physics, The Chinese University of Hong Kong, Shatin, Hong Kong SAR

Abstract

Gold nanorods have great potentials in optical, electronic, and biotechnological applications because of their rich surface plasmon properties. The longitudinal surface plasmon wavelengths (LSPWs) of gold nanorods are linearly dependent on their aspect ratios. The surface plasmon derived-properties of gold nanorods can be controlled not only during synthesis but also by remodeling after their growth.

In this poster, tailoring the LSPWs, scattering, and absorption cross sections of gold nanorods has been demonstrated by combining anisotropic shortening and transverse overgrowth and choosing the same starting Au nanorods. Dark-field imaging and FDTD calculations are also performed on the resulting nanorod samples.

Moreover, we have developed a feasible approach for the assembly of gold nanoparticle necklace structures in aqueous solutions using glutathione and cysteine. Three types of necklace structures have been demonstrated.

Taken together, our developed growth, shortening, and assembly approaches will facilitate the use of gold nanostructures in the areas of optics, optoelectronics, and biotechnology.

Surface Plasmon of Gold Nanospheres and Nanorods

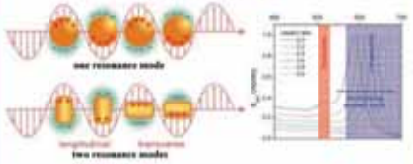

Anisotropic Shortening of Gold Nanorods By Oxidation

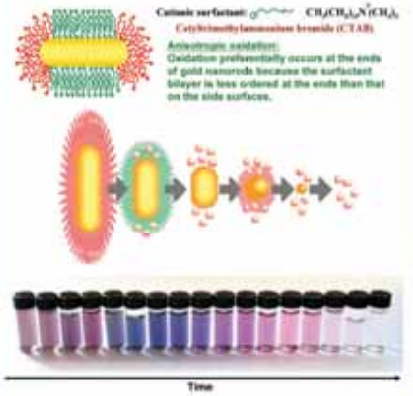

Selective Shortening of Gold Nanorods through Oxidation by H_2O_2

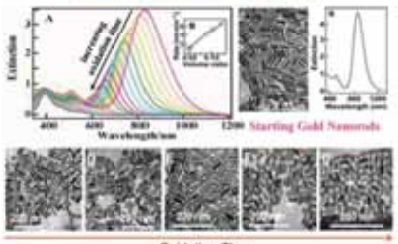

Oxidation Time

Transverse Overgrowth on Gold Nanorods

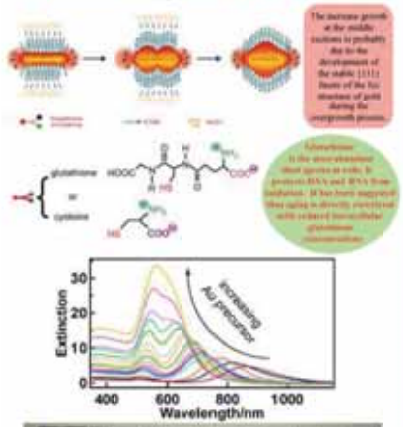

Increasing Au source

Comparison between Shortened and Overgrown Gold Nanorods

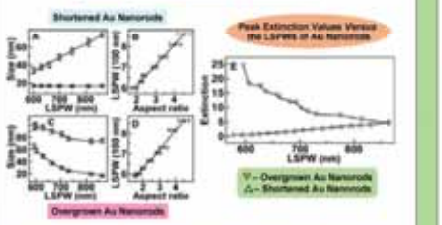

Single-Particle Dark-field Imaging and Spectroscopy

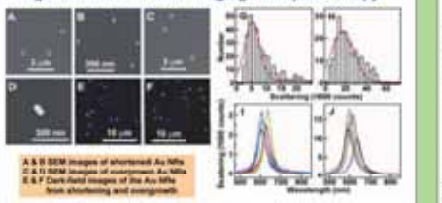

A & B SEM images of shortened Au NRs
C & D SEM images of overgrown Au NRs
E & F Dark-field images of the Au NRs from shortening and overgrowth

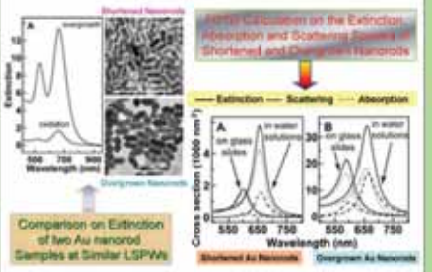

FDTD Calculated Surface Plasmon-related Properties of Au Nanorods With Varying Diameters

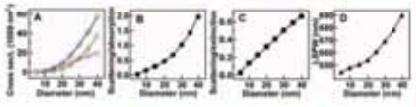

Au Nanorods at a Fixed Aspect Ratio

Nanonecklaces Assemblies of Au Nanorods, Nanosphers and Bipyramids

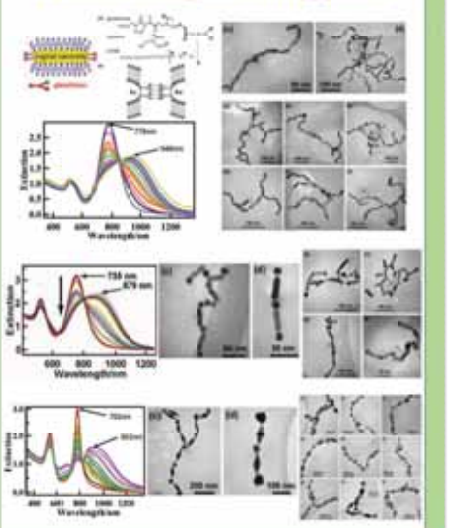

Conclusions

Anisotropic shortening and transverse overgrowth have been carried out to prepare Au nanorods with tunable LSPWs from the same starting nanorods. The use of the same starting nanorods allows for a quantitative comparison of the extinction values between the shortened and overgrown Au nanorods. It has been found that the scattering intensity of the overgrown nanorods is larger than that of the shortened nanorods. The experimental results are in very good agreement with the FDTD calculated ones. FDTD calculations further show that the scattering-to-extinction ratio increases linearly as a function of the diameter for Au nanorods with a fixed aspect ratio.

In addition, we have used glutathione or cysteine to assemble gold nanoparticles in an end-to-end fashion into necklace structures, in the aqueous solution without the addition of organic solvents. We believe that our results have great implications for the use of Au nanorods in a variety of optical and biotechnological applications.

Acknowledgments and References

This work was supported by the RGC Direct Allocation through CUHK under the Project Code of 2060285, and a RGC grant under the Project Code of 2150250.

References

1. W. H. Ni, X. S. Kou, Z. Yang, J. F. Wang, *ACS Nano.* **2008**, *2*, 677.
2. X. S. Kou, S. Z. Zhang, Z. Yang, C.-K. Tsung, G. D. Stucky, L. D. Sun, J. F. Wang, C. H. Yan, *J. Am. Chem. Soc.* **2007**, *129*, 6402.
3. C.-K. Tsung, X. S. Kou, Q. H. Shi, J. P. Zhang, M. H. Yeung, J. F. Wang, G. D. Stucky, *J. Am. Chem. Soc.* **2006**, *128*, 5352.
4. S. Z. Zhang, Y. S. Kou, Z. Yang, Q. H. Shi, G. D. Stucky, L. D. Sun, J. F. Wang, G. D. Stucky, *Chem. Commun.* **2007**, 1816.
5. Z. H. Sun, W. H. Ni, Z. Yang, X. S. Kou, L. Li, J. F. Wang, *Small* **2008**, accepted.

Conclusions

Anisotropic shortening and transverse overgrowth have been carried out to prepare Au nanorods with tunable LSPWs from the same starting nanorods. The use of the same starting nanorods allows for a quantitative comparison of the extinction values between the shortened and overgrown Au nanorods. It has been found that the scattering intensity of the overgrown nanorods is larger than that of the shortened nanorods. The experimental results are in very good agreement with the FDTD calculated ones. FDTD calculations further show that the scattering-to-extinction ratio increases linearly as a function of the diameter for Au nanorods with a fixed aspect ratio.

In addition, we have used glutathione or cysteine to assemble gold nanoparticles in an end-to-end fashion into necklace structures, in the aqueous solution without the addition of organic solvents. We believe that our results have great implications for the use of Au nanorods in a variety of optical and biotechnological applications.

KOU Xiaoshan Supervisor: Prof. Jianfang WANG
Department of Physics, Faculty of Science

Project Title "Tailoring Surface Plasmonic Properties of Gold Nanorods and Their Assembly"

Student Poster

ZHENG Mingjie **Supervisor: Prof. Kin Wah YU**
Department of Physics, Faculty of Science

Project Title "Anomalous size dependence of inverse participation ratio of localized eigenfunctions in graded elastic lattices"

The Chinese University of Hong Kong

Anomalous size dependence of inverse participation ratio of localized eigenfunctions in graded elastic lattices

M. J. ZHENG[a], M. GODA[b], K. YAKUBO[c], K. W. YU[a]
[a]*The Chinese University of Hong Kong, China;* [b]*Niigata University*, Japan; [c]*Hokkaido University, Japan*

Introduction

Graded materials have attracted extensive research interest and have shown great potential applications. Based on our finding of gradons which are localized vibrational modes peculiar to graded lattices and gradon-phonon transition, we continued to study and formulate the system-size dependence of the inverse participation ratio (IPR), which is important to identify gradon modes.

Objective

To obtain the analytical envelope function through quantum analog interpreation and study the system-size dependence of IPR of localized eigenfunctions in graded elastic lattices.

Model and Methods

1D graded elastic chain and 2D orthogonal graded square lattice (OGSL) with linearly graded mass and graded force constant

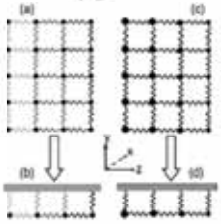

- Effective 1D model

$$\omega^2 A = \frac{K}{m} A$$

- Exact 2D model

$$M = e^{ik_x} e^{K} \Rightarrow \begin{cases} \mathrm{Abs}[\mathrm{Eigenvalue}[M]] = \omega^2 \\ \mathrm{Arg}[\mathrm{Eigenvalue}[M]] = k_x \\ \mathrm{Eigenvector}[M] = A_i \end{cases}$$

- **IPR** (inverse participation ratio):

$$IPR = \frac{\sum_{n=1}^{N} A_n^4}{\left(\sum_{n=1}^{N} A_n^2\right)^2}$$

- **Quantum analogue**
  - Hump structure of gradon wave function, is similar to that of quantum wave function with high quantum number in harmonic potential.
  - The probability

$$|A(x)|^2 \propto 1/v(x) \propto 1/\sqrt{x - x_c}$$

where x_c is the classical turning point $v(x)|_{x=x_c} = 0$

  - IPR can be derived analytically as a function of the system size:

$$N^{\alpha} \propto IPR = C_1 \log(N) + C_2$$

Mode patterns

Gradon modes ($\omega > \omega_c$)
Hump structure at a gradon front

Critical modes ($\omega = \omega_c$)
Hump structure appearing at one end

Phonon modes ($\omega < \omega_c$)
Almost flat structure

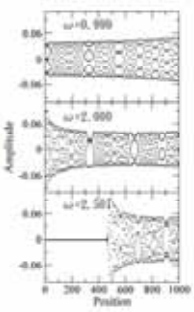

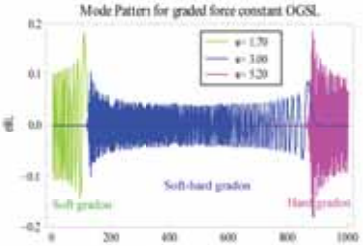

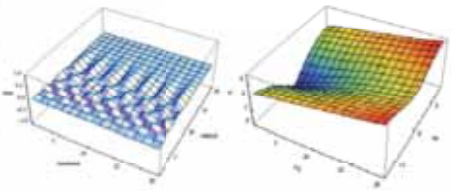

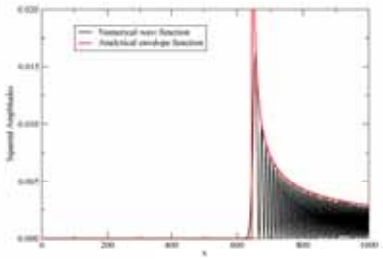

Results

I: IPR change rapidly at transition frequency (1D)

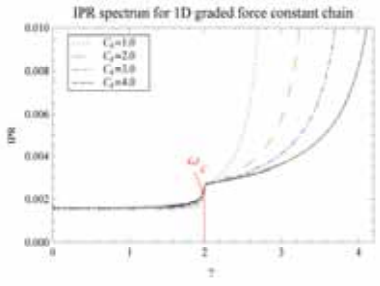

II: IPR change rapidly at transition frequency (2D)

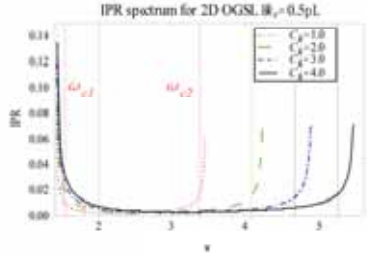

III: System-size dependence of IPR (1D)

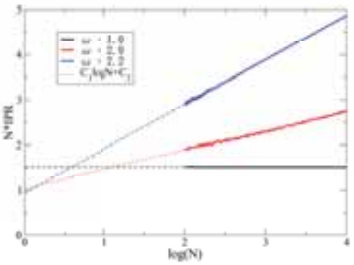

ω	C_1	C_2
1.0	0	1.507
2.0	0.423	1.040
2.2	0.983	0.935

IV: System-size dependence of IPR (2D)

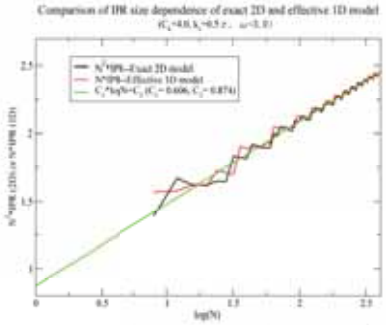

Coefficient	Phonons	Gradons	Contribution from
C_1	Vanish	finite	Gradon hump
C_2	> unity	unity	Gradon body

Conclusions

- Study IPR spectrum in graded 1D and 2D elastic lattices by using the effective 1D model and exact 2D model.
- Investigate the system-size dependence of IPR and formulate the results.
- Obtain the analytical envelope function from quantum analogue interpretation and derive the formula of IPR size dependence. The analytical results match quite well with the numerical results.
- The quantum analogue envelope function will be used to study other properties of graded system.

Acknowledgements

This work was supported by RGC Earmarked Grant of Hong Kong SAR Government.

References

[1] J. J. Xiao, K. Yakubo, and K. W. Yu, *Phys. Rev. B* **73**, 054201 (2006).
[2] J. J. Xiao, K. Yakubo, and K. W. Yu, *Phys. Rev. B* **73**, 224201 (2006).

KO Tze Cheung **Supervisor: Prof. Emily CHING**
Department of Physics, Faculty of Science

Project Title "Ultimate-state scaling in a shell model for homogeneous turbulent convection"

Student Poster

Ultimate-state scaling in a shell model for homogeneous turbulent convection*

Emily S.C. Ching[1,2] and T.C. Ko[1]

[1] *Department of Physics, The Chinese University of Hong Kong, Shatin, Hong Kong*
[2] *Institute of Theoretical Physics, The Chinese University of Hong Kong, Shatin, Hong Kong*

INTRODUCTION

An interesting question in turbulent convection is how the heat transport measured by the Nusselt number (Nu) depends on the strength of the thermal forcing, measured by the Rayleigh number (Ra), in the limit of very high Ra.

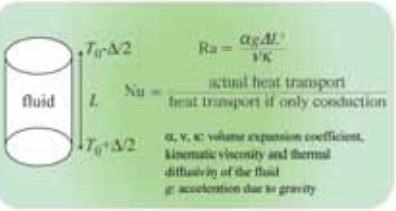

Kraichnan [1] argued that at very high Ra, convective eddies produced in the bulk generate turbulent boundary layers and the turbulence of which enhances heat transport. He obtained $\mathrm{Nu} \sim \mathrm{Ra}^{1/2}$ with logarithmic corrections. On the other hand, Grossmann and Lohse (GL) [2] argued that at very high Ra, the boundary layers would not contribute to energy and thermal dissipation and thus play no role in heat transport. Although their assumption of the role of the boundary layers in heat transport is different, they also predicted $\mathrm{Nu} \sim \mathrm{Ra}^{1/2}$. This kind of scaling behavior is taken as the signature of the ultimate state of turbulent convection.

By modelling the bulk of convective flow by three-dimensional homogeneous turbulent convection with periodic boundary conditions, Lohse and coauthors [3] reported $\mathrm{Nu} \sim \mathrm{Ra}^{1/2}\mathrm{Pr}^{1/2}$ and $\mathrm{Re} \sim \mathrm{Ra}^{1/2}\mathrm{Pr}^{-1/2}$ as predicted in GL, where $\mathrm{Pr} = \nu/\kappa$ and Re is the Reynolds number measuring the root-mean-squared velocity fluctuations. However buoyancy acts only at the largest scales in this system.

SHELL MODEL

We study the scaling of Nu and Re using a shell model for homogeneous turbulent convection in which buoyancy is acting on most of the scales. Shell model is constructed in a discretized Fourier space where $k_n = k_0 l^n$, $n = 0,1,\ldots,N\text{-}1$, is the wavenumber in the nth shell, $k_0 = 1$ and $l = 2$. The velocity and temperature variables u_n and θ_n satisfy

$$\frac{du_n}{dt} = ak_n(u_{n+1}^* u_{n+2}^* - lu_{n-1}u_{n+1}^*) + bk_n(u_{n-1}u_{n-2} - lu_{n+1}^* u_{n-1}) - \nu k_n^2 u_n + \alpha g \theta_n$$

$$\frac{d\theta_n}{dt} = k_n(u_{n+1}\theta_{n+1}^* - lu_{n-1}\theta_{n+1}^*) + k_n(u_{n-1}\theta_{n-1} - lu_{n+1}\theta_{n-1}) - \kappa k_n^2 \theta_n + \beta u_n$$

with positive parameters a and b. The model is forced by a temperature gradient of $-\beta$.

When b/a is larger than some critical value around 2, buoyancy is acting directly on most scales and the scaling behavior is given by Bolgiano-Obukhov (BO) ($u_n \sim k_n^{-3/5}$, $\theta_n \sim k_n^{-1/5}$) [rather than Kolmogorov 1941 (K41) scaling ($u_n \sim k_n^{-1/3}$, $\theta_n \sim k_n^{-1/3}$)] plus corrections. Also, there is an inverse energy transfer from small to large scales so that a drag $-\beta u_0 \delta_{n,0}$ acting on that largest scale has to be added.

We define Ra, Nu and Re in the shell model as

$$\mathrm{Ra} = \frac{\alpha g \beta}{\nu\kappa k_0^4} \qquad \mathrm{Re} = \frac{\left[\sum_n \langle u_n^2 \rangle\right]^{1/2}}{\nu k_0}$$

$$\mathrm{Nu} = \frac{\sum_n \langle u_n \theta_n \rangle}{\kappa\beta} + 1$$

Two exact results are derived:

$$\varepsilon_{total} = \nu^3 k_0^4 (\mathrm{Nu} - 1)\mathrm{Ra}\,\mathrm{Pr}^{-1} \quad (1)$$

$$\chi = \kappa\beta^2 \mathrm{Nu} \quad (2)$$

where the total energy dissipation rate is $\varepsilon_{total} = \varepsilon + \varepsilon_{drag}$, with $\varepsilon = \nu^3 \sum_n k_n^2 \langle u_n^2 \rangle$ being the average energy dissipation rate due to viscosity and $\varepsilon_{drag} = f(\langle u_0^2 \rangle)$ is the average energy dissipation rate due to the large scale drag. The average thermal dissipation rate is

$$\chi = \kappa \sum_n k_n^2 \langle \theta_n^2 \rangle + \kappa\beta^2$$

RESULTS & DISCUSSIONS

In our simulations, we obtained

$\mathrm{Nu} \sim \mathrm{Ra}^{0.500\pm0.001}\mathrm{Pr}^{0.51\pm0.01}$

$\mathrm{Re} \sim \mathrm{Ra}^{0.500\pm0.001}\mathrm{Pr}^{-0.50\pm0.01}$

which is consistent with GL.

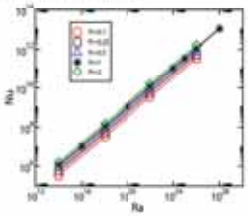

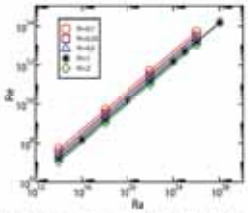

We also check the scaling of ε and χ. Our results are:

$$\chi \sim \kappa\beta^2 (\mathrm{RePr})^{1.000\pm0.001} \quad (3)$$

and $\varepsilon \sim \nu^3 k_0^4 \mathrm{Re}^{2.48\pm0.02}$. The former result is consistent with GL but the latter is not.

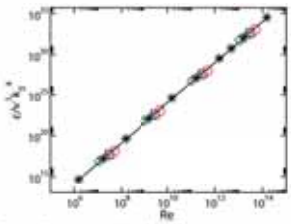

We show that $\varepsilon \sim \nu^3 k_0^4 \mathrm{Re}^{(2+\eta)}$ where η is defined by $u_n \sim k_n^{-\eta}$. When buoyancy is acting on most scales, $\eta = 3/5$ giving $4/(1+\eta) = 5/2$ as observed. Moreover,

$$\varepsilon_{total} \approx \varepsilon_{drag} \sim \nu^3 k_0^4 \mathrm{Re}^{3.00\pm0.01} \quad (4)$$

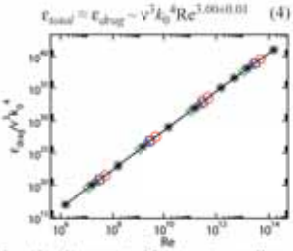

Solving (1)-(4), we get ultimate-state scaling: $\mathrm{Nu} \sim \mathrm{Ra}^{1/2}\mathrm{Pr}^{1/2}$ and $\mathrm{Re} \sim \mathrm{Ra}^{1/2}\mathrm{Pr}^{-1/2}$.

As a damping mechanism at large scale cannot exist by itself in the bulk of turbulent convection but could be resulted from the boundaries, this suggests that when buoyancy is acting directly on most scales, the boundaries must play a crucial role in giving rise to the ultimate-state scaling.

On the other hand, when buoyancy acts only on the largest scales, $\eta = 1/3$ and $4/(1+\eta) = 3$. In this case ε_{total} is dominated by ε and ultimate-state scaling also follows.

CONCLUSION

There are two different physical scenarios that can lead to the ultimate-state scaling. In the first scenario, which is illustrated in the present work, buoyancy is acting directly on most of the scales of the bulk of turbulent convection. An effective damping at the largest scales, which can be provided by the interaction of the inverse energy transfer with the boundaries, is crucial. In the second scenario, buoyancy is acting only as a driving force on the largest scales, and the boundary layers play no role in heat transport. The first scenario is in accord with the physical picture presented in [1] while the second scenario is in accord with that proposed by [2].

[1] R.H. Kraichnan, Phys. Fluids **5**, 1374 (1962).
[2] S. Grossmann and D. Lohse, J. Fluid Mech. **407**, 27 (2000).
[3] E. Calzavarini, D. Lohse, F. Toschi, and R. Tripiccione, Phys. Fluids **17**, 055107 (2005).

*This work is supported in part by the Hong Kong Research Grants Council (Grant No. CA05/06.SC01).

LIANG Yao **Supervisor: Prof. HARK Sui Kong**
Department of Physics, Faculty of Science

Project Title "The Synthesis and Optical Properties of ZnGa2O4 Nanowires with Axial Structural Modulation"

The Synthesis and Optical Properties of $ZnGa_2O_4$ Nanowires with Axial Structural Modulation

Yao Liang and Sui Kong Hark
Department of Physics, The Chinese University of Hong Kong
yliang@phy.cuhk.edu.hk

Introduction

Zinc gallate ($ZnGa_2O_4$) with a band gap of 4.4-5.0 eV is a new and interesting phosphor. Its high chemical and thermal stability also suggest promising applications in field emission display devices. Some novel 1D $ZnGa_2O_4$ nanostructures have been synthesized successfully via various methods[1]. We have synthesized nanowires with a modulated structure on Si (100) substrates via the catalyst-free chemical vapor deposition. Transmission electron microscopy investigations show that all the nanowires are cubic in structure and grow along the <111> direction. More interestingly, two kinds of structural changes are found along the growth direction. One is the formation of twin boundaries ($[1\bar{1}\bar{1}]/[\bar{1}\bar{1}1]$) and the other is the 30° twisted boundaries ($[\bar{1}12]/[011]$), both kinds of defects are rare in ternary oxide nanowires. The dependence of the optical properties of the nanowires on the crystalline structure was studied by cathodoluminescence (CL) spectroscopy and imaging.

Synthesis

Sample distance from source (ZnO, Zn powder & Ga droplet)
(**S1**): 1cm; (**S2**): 4cm

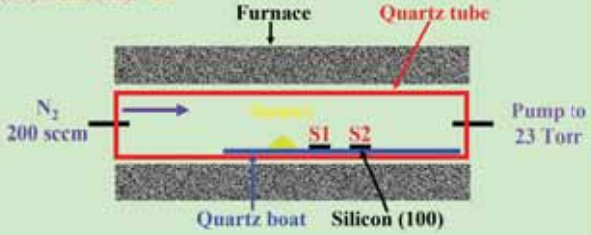

Furnace center temperature: 1100 ℃ Kept for 1h

Sample S1

Morphology

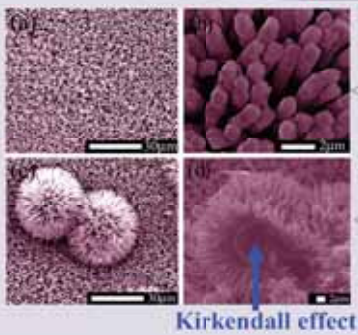

Aligned $ZnGa_2O_4$ nanowires

Flower-like assemblies

Kirkendall effect

Structure by TEM

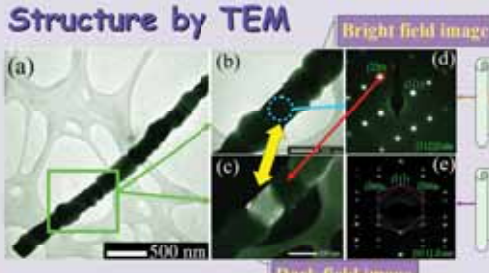

Selected area electron diffraction pattern

Twin boundary
$[1\bar{1}\bar{1}]/[\bar{1}\bar{1}1]$

Optical properties by CL

In large nanowires strong luminescence overwhelms the observation of defects

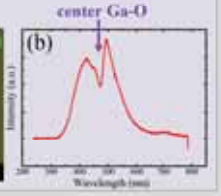

Sample S2

Morphology

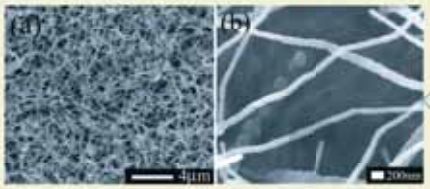

Lower growth temperature, finer nanowires

Zn Ga O

Structure by TEM

Structural changes along the Growth direction

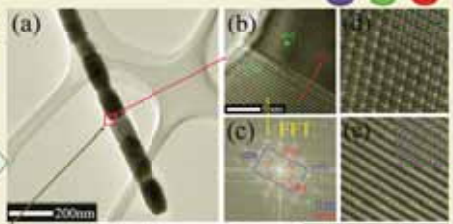

30° twisted boundary

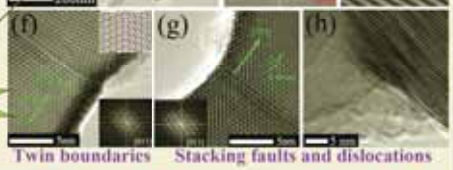

Twin boundaries Stacking faults and dislocations

Optical Properties by CL

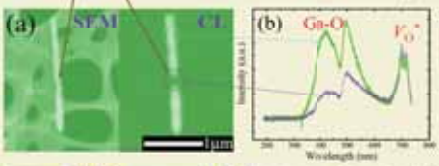

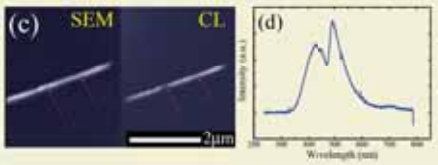

The emission intensity is strongly dependent on the crystalline structure

Conclusion

Structurally modulated $ZnGa_2O_4$ nanowires were synthesized. The presence of stacking faults, dislocations, twin boundaries and 30° twisted boundaries along their axial direction were observed. More interestingly, CL imaging shows that the luminescence of the nanowires is strongly affected by their structure. The luminescence from 350 to 600 nm are attributed to octahedral Ga-O related self-activation centers[2] and the peaks around 700 nm to oxygen vacancy $V_O^{\bullet\bullet}$[3].

Acknowledgement

The work described in this paper was partially supported by a grant from the Research Grants Council of the Hong Kong Special Administrative Region, China (Project No. 411807) and a CUHK direct grants (Project codes: 2060305)

Reference

1. U. K. Gautam, Y. Bando, J. Zhan, et. al., *Adv. Mater.* **20** (2008) 810.
2. S. Y. Bae, H. W. Seo, C. W. Na, et. al., *Chem. Commun.* (2004) 1834.
3. J. S. Kim, H. I. Kang, W. N. Kim, et.al., *Appl. Phys. Lett.* **82** (2003) 2029.

ZHU Jiangtao **Supervisor: Prof. Dickon NG**
Department of Physics, Faculty of Science

Project Title "Growth of Carbon Nanostructure by Minerals in Bamboo"

Student Poster

Growth of Carbon Nanostructure by Minerals in Bamboo

Jiangtao Zhu, Fung-luen Kwong and Dickon H.L.Ng
Department of Physics, The Chinese University of Hong Kong
jtzhu@phy.cuhk.edu.hk

Abstract

A carbon nanostructure/porous carbon composite has been prepared by ethanol CVD method on bamboo charcoal. The growth of carbon nanostructure is catalyzed by minerals in bamboo. There are several kinds of carbon nanostructures: hollow carbon nanotube (CNT), silicate/CNT nanocable and silicate nanowires covered with turbostratic carbon. The growth mechanism of the carbon nanostructure is proposed base on SEM, TEM, and EELS characterization. The change of the CNT diameter might due to the poor wettability between the silicate and the carbon.

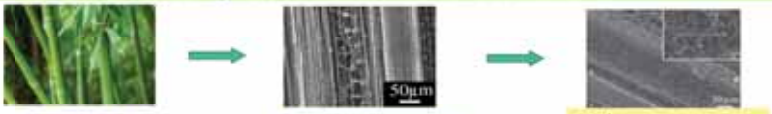

Bamboo → Bamboo Charcoal → Carbon nanostructure /Bamboo Charcoal

SEM and TEM images

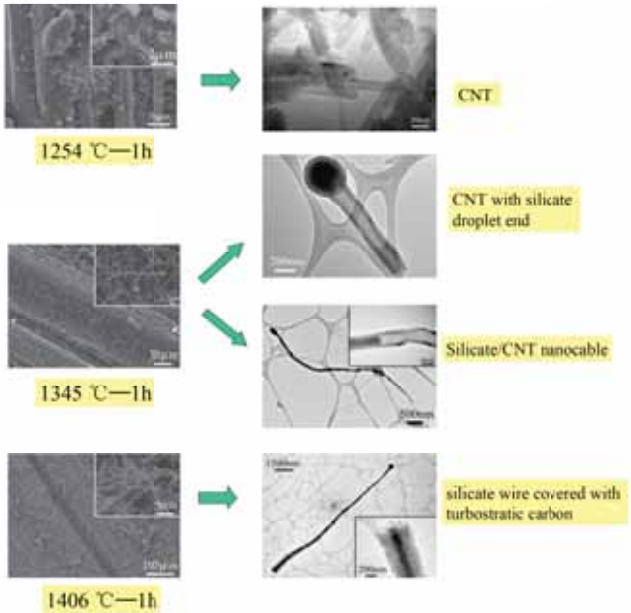

1254 ℃—1h → CNT

1345 ℃—1h → CNT with silicate droplet end; Silicate/CNT nanocable

1406 ℃—1h → silicate wire covered with turbostratic carbon

EELS maps

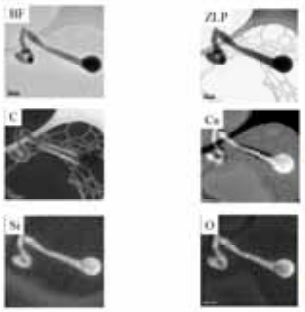

Silicon, Calcium and Oxygen completely filled inside the CNT, named as silicate/CNT nanocable structure

Capillary force

$$\Delta P = -\frac{2\gamma\cos\theta}{r}$$

θ=Contact angle= 120-130°
r = Radius of the tube =50nm
γ=Surface tension= 200mN/m
ΔP= Pressure difference across the liquid-vapor interface = -4.6×10^6 Pa

A pressure about 4.6×10^6 Pa is needed to fill the silicate into CNT. So the growth of the silicate is expected to happen before or at the same of the growth of CNT.

Growth mechanism of carbon nanostructure

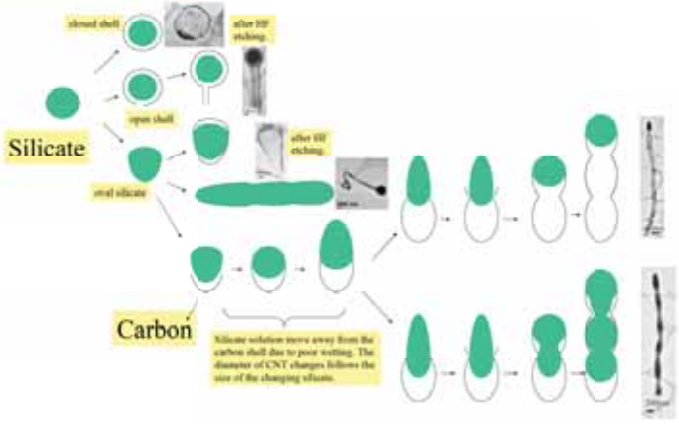

Experiment Setup

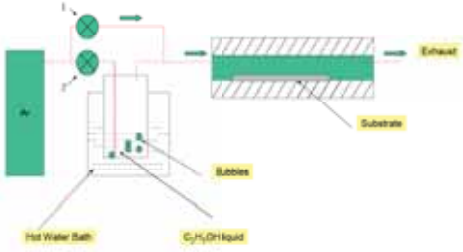

Valve 1: Ar gas to protect the sample from oxidation.
Valve 2: Ar gas carry carbon source into furnace.
During reaction: valve 1 close, valve 2 open
During heating or cooling: valve 1 open valve 2 close.

JIA Juncai **Supervisor: Prof. Jimmy YU**
Environmental Science Programme, Faculty of Science

Project Title "Microwave-Assisted Synthesis of Monodispersed Silver@Phenol Formaldehyde Resin Core/Shell Nanostructures"

Microwave-Assisted Synthesis of Monodispersed Silver@Phenol Formaldehyde Resin Core/Shell Nanostructures

Juncai Jia, Jimmy C. Yu*, Xianluo Hu
Environmental Science Programme, The Chinese University of Hong Kong
***Email: jimyu@cuhk.edu.hk**

Abstract

A series of Silver@phenol formaldehyde resin core/shell architectures including monodispersed nanospheres, nanoglobes and nanocables have been prepared by an efficient microwave-hydrothermal process. The size of the monodispersed nanospheres could be controlled in the range of 100 to 400 nm by changing the ratio of phenol to hexamine. The interesting nanoglobes and nanocables could be synthesized by adding triblock copolymers Pluronic F127 (EO97PO69EO97) or CTAB. The as-prepared products were characterized by scanning electron microscopy (SEM), transmission electron microscopy (TEM), X-ray diffraction (XRD), Fourier transform IR (FTIR), and HRTEM. The synthesized core/shell nanostructures with controllable morphologies may have potential applications in biotechnology and many other fields.

Formation Mechanism of core/shell silver@Phenol Formaldehyde Resin (PFR)

Microwave-Assisted Mono-core/shell Ag@PFR Nanospheres

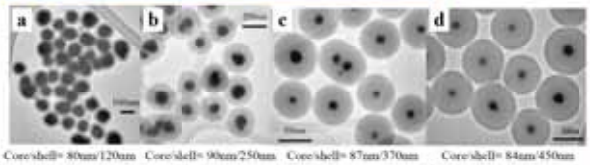

Figure 1. TEM images of the centered mono-core/shell spheres prepared at 220 ℃ for 10mins at various Phenol/Hexamine/$AgNO_3$ mole ratios (mmol/mmol/mmol) (a)0.2:0.1:0.05, (b) 0.3:0.15:0.05, (c) 0.4:0.2:0.05, (d) 0.5:0.25:0.05

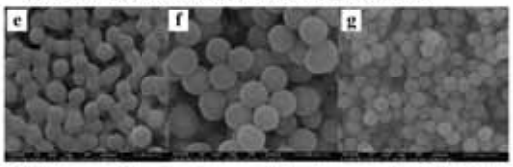

Figure 2. TEM images of the centered mono-core/shell spheres prepared at 220 ℃ for 10mins at various Phenol/Hexamine/$AgNO_3$ mole ratios (mmol/mmol/mmol) (e) 0.3:0.15:0.05, (f) 0.4:0.2:0.05,(g) 0.5:0.25:0.05

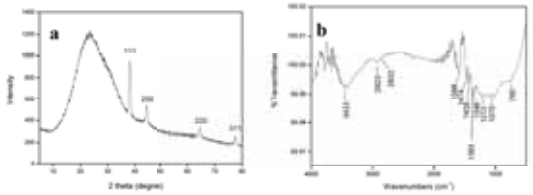

Figure 3. (a) XRD patterns and (b) FT-IR spectrum of the mono-core/shell spheres prepared at Phenol/Hexamine/$AgNO_3$ mole ratio (mmol/mmol/mmol) = 0.5:0.25:0.05

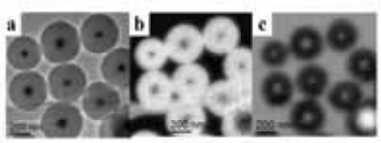

Figure 4. EELS mapping of the mono-core/shell spheres prepared at Phenol/Hexamine/$AgNO_3$ mole ratio= 0.5:0.25:0.05(mmol/mmol/mmol) (b) Carbon map (c) silver map

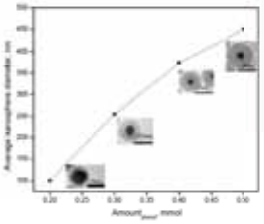

Figure5. A plot of average nanosphere diameter versus amounts of phenol/hexamine

Microwave-assisted Synthesis of Ag/PFR Nanocables

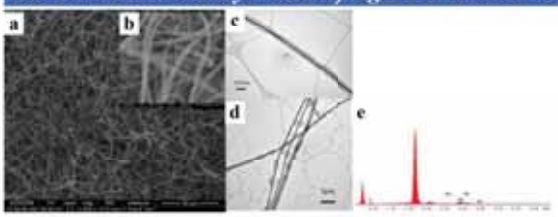

Figure 6. FESEM images (a,b), TEM images (c,d) and EDX of Ag/PFR nanocables prepared at 220 ℃ for 10mins, Phenol/Hexamine/AgNO3 mole ratio=0.2:0.1:0.05(mmol/mmol/mmol) in the presence of 0.25g CTAB

Microwave-assisted Synthesis of Ag/PFR Nanoglobes

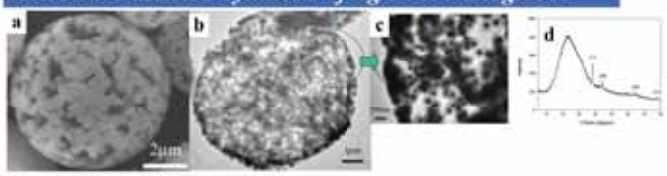

Figure 7. SEM image (a), TEM images (b, c) and XRD pattern (d) of Ag/PFR nanoglobes prepared at 220 ℃ for 10mins, Phenol/Hexamine/AgNO3 mole ratio=0.2:0.1:0.05(mmol/mmol/mmol) in the presence of 0.5g F127

Schematic Illustration of Ag/PFR Monodispersed Nanopheres Formation Process

Schematic Illustration of the Ag/PFR Coaxial Nanocables Formation Process 1, 2

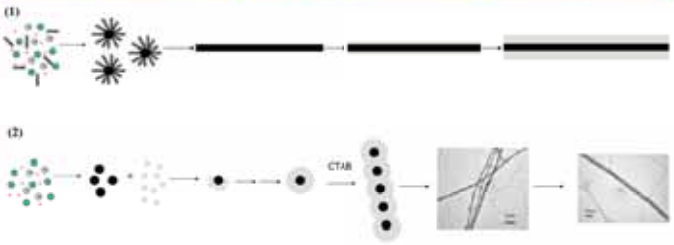

Schematic Illustration of the Ag/PFR Coaxial Nanoglobes Formation Process

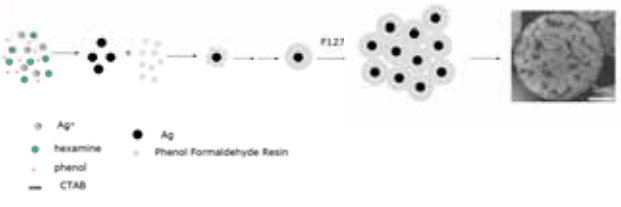

CHAN Kwok Wai **Supervisor: Prof. Conan LEUNG**
Department of Mathematics, Faculty of Science

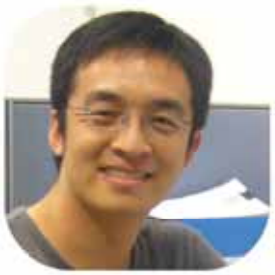

Student Poster

Project Title "Mirror symmetry for toric Fano manifolds via SYZ transformations"

Mirror symmetry for toric Fano manifolds via SYZ transformations

Kwok-Wai CHAN
Department of Mathematics
Chinese University of Hong Kong
kwchan@math.cuhk.edu.hk

1. Introduction

Mirror symmetry for Calabi-Yau manifolds was discovered by string theorists almost twenty years ago. In the mid nineties, it was extended to the non-Calabi-Yau setting, notably to **Fano manifolds**, by the works of Givental, Kontsevich, and Hori-Vafa [4]. Let $N \cong \mathbb{Z}^n$ be a lattice and $M = \mathrm{Hom}(N, \mathbb{Z})$ the dual lattice. If X is a toric Fano manifold associated to a polytope $P = \{x \in M_{\mathbb{R}} = N \otimes_{\mathbb{Z}} \mathbb{R} : \langle x, v_i \rangle \geq \lambda_i \text{ for } i = 1, \ldots, d, \}$, then the mirror of X is given by a pair (Y, W), where Y is **Hori-Vafa's mirror manifold**, which turns out to be isomorphic to the algebraic torus $(\mathbb{C}^*)^n$, and $W : Y \to \mathbb{C}$ is Laurent polynomial

$$W = e^{\lambda_1} y^{v_1} + \ldots + e^{\lambda_d} y^{v_d},$$

for $y = (y_1, \ldots, y_n) \in Y$, which is a holomorphic Morse function. In the physics literature, this is called a **Landau-Ginzburg (LG) model** and W is called the **superpotential**. We will focus on one half of the story namely, the correspondence between the symplectic geometry (**A-model**) on X and the complex geometry (**B-model**) on (Y, W). There are two main mathematical predictions:

Conjecture 1.1.

(1) The quantum cohomology ring $QH^*(X)$ is isomorphic to the Jacobian ring $Jac(W)$.

(2) There is a equivalence of triangulated categories:

$$D^b Fuk(X) \cong D_{Sg}(Y, W)$$

where $D^b Fuk(X)$ is the derived Fukaya category of X and $D_{Sg}(Y, W)$ is the triangulated category of singularities of the pair (Y, W).

Conjecture (1) has been verified for toric Fano and flag manifolds by the works of Givental and many others. The homological mirror symmetry conjecture (2), which has been checked in some cases, was first formulated by Kontsevich. However, despite these evidences, a straightforward and simple geometric explanation for the mirror symmetry phenomenon for Fano manifolds is still lacking. On the other hand, the **Strominger-Yau-Zaslow (SYZ) conjecture** [5] suggested that mirror symmetry for Calabi-Yau manifolds should be understood as a **T-duality** with corrections. The aim of our work [2] is to explore the mirror symmetry phenomenon for toric Fano manifolds via this SYZ approach, in order to provide a simple geometric picture to see how it works.

2. Derivation of Hori-Vafa's mirror manifold by semi-flat SYZ

We first review Hori-Vafa's description of the mirror of the toric Fano manifold X. In constructing X as a symplectic quotient, we encounter an exact sequence:

$$0 \longrightarrow K \xrightarrow{\iota} \mathbb{Z}^d \xrightarrow{\beta} N \longrightarrow 0 \tag{2.1}$$

where $\beta : \mathbb{Z}^d \to N$ is defined by $\beta(\sum_{i=1}^d k_i e_i) = \sum_{i=1}^d k_i v_i$ and $K = \ker(\beta)$. If $Q_1 = (Q_{11}, \ldots, Q_{d1}), \ldots, Q_l = (Q_{1l}, \ldots, Q_{dl}) \in \mathbb{Z}^d$ is a $\mathbb{Z}$-basis of K, then the mirror manifold of X, derived by Hori and Vafa in [4] using physical arguments, is the complex submanifold

$$Y = \left\{(Z_1, \ldots, Z_d) \in (\mathbb{C}^*)^d : \sum_{i=1}^d Q_{ia} Z_i = r_a, \quad a = 1, \ldots, l\right\},$$

in $(\mathbb{C}^*)^d$, where $r_a = -\sum_{i=1}^d Q_{ia} \lambda_i$ for $a = 1, \ldots, l$. In these coordinates, the superpotential $W : Y \to \mathbb{C}$ is given by

$$W = e^{-\lambda_1} z_1 + \ldots + e^{-\lambda_d} z_d$$

Now, the moment map corresponding to the Hamiltonian T^m-action on X gives rise to a Lagrangian torus fibration $\mu : X \to P$, the restriction of which to the open dense orbit $X_0 \subset X$ is the **SYZ fibration**

$$\mu : X_0 \to P^\circ,$$

which turns out to be a torus bundle. Indeed, in the symplectic coordinates, X_0 splits into a product $P^\circ \times T_N$ where T_N is the real torus $N_{\mathbb{R}}/N$; and X_0 can be viewed as the quotient T^*P°/N. Applying T-duality gives the **semi-flat SYZ mirror** $Y_{SYZ} = T P^\circ / M = P^\circ \times T_M$ where T_M is the torus $M_{\mathbb{R}}/M$, together with the fibration

$$\nu : Y_{SYZ} \to P^\circ.$$

Proposition 2.1. *(Chan-Leung [2]) The semi flat mirror manifold Y_{SYZ} is an open complex submanifold in Hori-Vafa's mirror manifold Y.*

A key in the proof is the simple observation that the dual of the quotient torus $T_N = T^d/T_K$, where $T_K = K_{\mathbb{R}}/K$, is the subtorus $T_M \subset (T_d)^*$. Note that the SYZ mirror is "smaller" than Hori-Vafa's mirror, this issue was discussed in Hori-Vafa [4] and Auroux [1]. For our purposes, we will confuse the notations and use Y to denote either the SYZ mirror or Hori-Vafa's mirror.

3. SYZ mirror transformations

While semi-flat SYZ constructions can produce the mirror manifold Y, we cannot get the superpotential $W : Y \to \mathbb{C}$. This is basically because we have ignored the toric boundary $X \setminus X_0 = \bigcup_{i=1}^d H_i$, and hence quantum corrections. Here H_i denotes the toric divisor which corresponds to $v_i \in N$. To restore this information, we consider the cover

$$\pi : \overline{X}_0 = X_0 \times N \to X_0,$$

and introduce a generating function for holomorphic discs counting as follows. Fix a point $x \in P^\circ$, where P° denotes the interior of the polytope P, and let $L_0 = \mu^{-1}(x)$ be the Lagrangian torus fibre over x. Then the above exact sequence (2.1) coincides with the following exact sequence of homotopy groups:

$$0 \longrightarrow H_2(X, \mathbb{Z}) \xrightarrow{\iota^*} \pi_2(X, L_0) \xrightarrow{\partial} \pi_1(L_0) \longrightarrow 0.$$

It is known that $\pi_2(X, L_0)$ is generated by d classes $\beta_1, \ldots, \beta_d$ each of which is represented by a unique holomorphic disc (see Cho-Oh [3])

$$\varphi_i : (D^2, \partial D^2) \to (X, L_0).$$

Let $\pi_2^+(X, L_0) = \left\{\sum_{i=1}^d k_i \beta_i \in \pi_2(X, L_0) : k_i \in \mathbb{Z}_{\geq 0}, \ i = 1, \ldots, d\right\}$ be the cone generated by $\beta_1, \ldots, \beta_d$. For $\beta = \sum_{i=1}^d k_i \beta_i \in \pi_2^+(X, L_0)$, we let $w(\beta) = \prod_{i=1}^d \lambda_i^{k_i}$ be its weight. Now consider the Kähler cone $\mathcal{K} \subset H^2(X, \mathbb{R})$ of X. Each $q = (q_1, \ldots, q_l) \in \mathcal{K}$ ($l = d - n =$ Picard number of X) determines a symplectic structure of X.

Definition 3.1. *For $\tau = (q_1, \ldots, q_l) \in \mathcal{K}$, define the function $\Phi_\tau \in C^\infty(\overline{X}_0)$ by*

$$\Phi_\tau(x, v) = \sum_{\beta \in \pi_2^+(X, L_0), \ \beta \neq 0} \frac{1}{w(\beta)^x} \cdot \overline{z}^{\partial \beta}.$$

This gives a family of functions $\{\Phi_\tau\} \subset C^\infty(\overline{X}_0)$ over $\mathcal{K}$. The upshot is that we can now define the **SYZ mirror transformation**

$$\mathcal{F} : \Omega^n(\overline{X}_0) \to \Omega^n(Y),$$

which is of **Fourier-type**, using the fiber product of the dual fibrations:

$$\begin{array}{ccc} \overline{X}_0 = \rho_P Y & \xrightarrow{\pi_Y} & \overline{X}_0 \\ {\scriptstyle \pi_N}\downarrow & & \downarrow{\scriptstyle \rho} \\ Y & \xrightarrow{\nu} & P^\circ \end{array}$$

One of our main results was showing how to obtain W:

Theorem 3.1. *(Chan-Leung [2]) The SYZ transformation of the generating function Φ_τ for holomorphic discs counting on the toric Fano manifold X gives the superpotential W on the mirror manifold $Y \cong (\mathbb{C}^*)^n$:*

$$\mathcal{F}(\Phi_\tau) = e^W.$$

Furthermore, we can incorporate the symplectic structure ω_X on X to give the holomorphic volume form on the Landau-Ginzburg model (Y, W) in the sense that

$$\mathcal{F}(\Phi_\tau \omega^n) = e^W \Omega_Y.$$

Here $\Phi_\tau \omega^n$ should be regarded as the symplectic form on X weighted by quantum corrections, the mirror of which is the holomorphic volume form $e^W \Omega_Y$ on Y.

4. Quantum cohomology vs. Jacobian ring

If we further assume that X is a product of projective spaces, then $\{\Phi_\tau\}$ can be used to compute the quantum cohomology $QH^*(X)$ as follows. We first showed that the logarithmic derivatives of Φ_τ with respect to q_a for $a = 1, \ldots, l$, are given by

$$\frac{\partial \Phi_\tau}{\partial q_a} = \Phi_\tau * \Psi_{\pi(\log q_a)}$$

Here, for $i = 1, \ldots, d$, $\Psi_i \in C^\infty(\overline{X}_0)$ is defined by

$$\Psi_i(x, v) = \begin{cases} e^{-\int_{x_0}^x \omega + 2\pi i \langle v, v_i \rangle} & \text{if } x = x_0, \\ 0 & \text{if } x \neq x_0, \end{cases}$$

and $*$ denotes the **convolution product** with respect to the lattice N. Then we have

Proposition 4.1. *(Chan-Leung [2]) There is a natural isomorphism of $\mathbb{C}$-algebras*

$$QH^*(X) \cong \mathbb{C}[\Psi_1, \ldots, \Psi_d] / \sim$$

provided that X is a product of projective spaces.

Here $\mathbb{C}[\Psi_1, \ldots, \Psi_d]$ is the polynomial algebra generated by $\Psi_1, \ldots, \Psi_d$ with respect to the convolution product, and $\sim$ is a relation that corresponds to the linear equivalence among the toric divisors $H_1, \ldots, H_d$. The key to the proof is by observing that the holomorphic curves which are responsible for the quantum corrections can be obtained by gluing the holomorphic discs $\varphi_1, \ldots, \varphi_d$. This can be seen by passing to the tropical picture, and we argue using **tropical geometry**.

The above proposition says that **the quantum product can be realized as a convolution product**. And now the SYZ mirror transformation takes the quantum product to the ordinary product of functions, just as what Fourier series does:

Theorem 4.1. *(Chan-Leung [2]) The SYZ mirror transformation induces a natural isomorphism of $\mathbb{C}$-algebras*

$$\mathcal{F} : QH^*(X) \xrightarrow{\cong} Jac(W)$$

provided that X is a product of projective spaces.

5. An example

Consider $X = \mathbb{P}^2$. We take $N = \mathbb{Z}^2$, $v_1 = (1, 0)$, $v_2 = (0, 1)$ and $v_3 = (-1, -1)$, and $P = \{x \in \mathbb{R}^2 : x_1 \geq 0, \ x_2 \geq 0, \ x_1 + x_2 \leq t\}$, where $t > 0$. The mirror manifold is given by $Y = \{(Z_1, Z_2, Z_3) \in \mathbb{C}^3 : Z_1 Z_2 Z_3 = q\} \cong (\mathbb{C}^*)^2$, where $q = e^{-t}$ is the Kähler parameter, and the superpotential $W : Y \to \mathbb{C}$ can be written as

$$W = Z_1 + Z_2 + Z_3 = z_1 + z_2 + \frac{q}{z_1 z_2}$$

for $(z_1, z_2) \in Y$. The Jacobian ring $Jac(W)$ is given by

$$Jac(W) = \mathbb{C}[Z_1, Z_2, Z_3] / \langle Z_1 - Z_2 Z_3, Z_2 - Z_3 Z_1 Z_3 Z_3 - q \rangle = \mathbb{C}[Z_1] / \langle Z^3 - q \rangle.$$

There are three toric divisors H_1, H_2, H_3 corresponding to the three holomorphic discs $\varphi_1, \varphi_2, \varphi_3 : (D^2, \partial D^2) \to (X, L_0)$ (and also three functions $\Psi_1, \Psi_2, \Psi_3 : \overline{X}_0 \to \mathbb{C}$) respectively, if we fix $x \in P^\circ$. The quantum cohomology ring is well-known to be given by

$$QH^*(X) = \mathbb{C}[H_1, H_2, H_3] / \langle H_1 - H_3, H_2 - H_3, H_1 + H_2 + H_3 - q \rangle = \mathbb{C}[H] / \langle H^3 - q \rangle$$

where H is the hyperplane class. Quantum corrections appear in only one relation, namely,

$$H_1 + H_2 + H_3 = q.$$

Fix a point $x \in P^\circ$. Then the correction is due to the unique holomorphic curve $\varphi : (\mathbb{P}^1, \infty_0, \infty_1, \infty_2, \infty_3) \to X$ of degree 1 (i.e. a line) with 4 marked points such that $\varphi(\infty) = p$ and $\varphi(\infty_i) \in H_i$ for $i = 1, 2, 3$. **The holomorphic curve φ can be obtained by gluing the holomorphic discs $\varphi_1, \varphi_2, \varphi_3$**, as can be seen in the tropical picture. The tropical curve corresponding to this line is Γ, which is glued from three half lines emanating from the point $y_0(x) \in N_{\mathbb{R}}$ in the directions $v_1 = (1, 0)$, $v_2 = (0, 1)$ and $v_3 = (-1, -1)$. These half lines are the tropical discs corresponding to $\varphi_1, \varphi_2, \varphi_3$. See Figure 1 below.

Figure 1

6. Discussion

The difficulty in removing the condition that X is a product of projective spaces in Proposition 4.1 can be seen by considering the Hirzebruch surface $X = Y_\Sigma$, which is the blow-up of $\mathbb{P}^2$ at one T_N-invariant point. In this case, there are four toric prime divisors H_1, H_2, H_3, H_4, and the quantum cohomology ring is given by

$$QH^*(X) = \frac{\mathbb{C}[H_1, H_2, H_3, H_4]}{\langle H_1 - H_3 + H_4, H_2 - H_3, H_1 + H_3 - q_1, H_2 + H_4 - q_2 H_4 \rangle}$$

However, the corrections in the quantum relation

$$H_2 + H_4 = q_2 H_4$$

is due to the exceptional curve H_4 which lies entirely in the toric boundary and hence **does not correspond to any tropical curve**. We thus cannot argue using tropical geometry as before. Nevertheless, we believe that this is just a technical difficulty and the argument should go through after modification. Indeed, Proposition 4.1 is known to be true for any toric Fano manifold X by Givental's mirror theorem.

References

[1] D. Auroux, *Mirror symmetry and T-duality in the complement of an anticanonical divisor*, preprint, 2007 (arXiv:0706.3207).

[2] K.-W. Chan and N.-C. Leung, *Mirror symmetry for toric Fano manifolds via SYZ transformations*, preprint, 2008 (arXiv:0801.2830).

[3] C.-H. Cho and Y.-G. Oh, *Floer cohomology and disc instantons of Lagrangian torus fibers in Fano toric manifolds*, Asian J. Math. 10 (2006), no. 4, 773–814 (math.SG/0308225).

[4] K. Hori and C. Vafa, *Mirror symmetry*, preprint, 2000 (hep-th/0002222).

[5] A. Strominger, S.-T. Yau and E. Zaslow, *Mirror symmetry is T-duality*, Nuclear Phys. B 479 (1996), no. 1-2, 243–259 (hep-th/9606040).

Joint Faculty Research Day 2008

ZHAO Jing **Supervisor: Prof. WONG Hoi Ying**

Department of Statistics, Faculty of Science

Project Title "An Artificial Boundary Method For American Option Pricing Under The CEV Model"

An Artificial Boundary Method for American Option Pricing under the CEV Model

JING ZHAO

Department of Statistics, The Chinese University of Hong Kong, Shatin, N.T., Hong Kong

Introduction

- American options: popular derivatives
- Valuation: challenge (early exercise strategy)
- Closed-form solutions do not exist
- Numerical methods:

(1) Simulation: inaccurate, time-consuming

(2) Lattice methods: an explicit finite difference method (FDM), conditionally stable

(3) Solving the partial differential equations (PDEs) numerically: e.g. implicit FDM, unconditionally stable for a PDE with a bounded domain. How to truncate the infinite domain into a finite one?

- Black-Scholes model: 1997 Nobel Prize for Economics
- Volatility smile in the financial market: Black-Scholes model, which assumes a constant volatility, is incorrect.

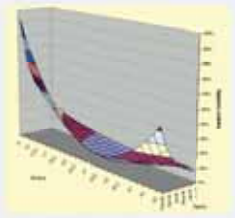

Figure 1: MSFT implied volatility surface for Feb06

- To capture the volatility smile: the constant elasticity of variance (CEV) model (Cox, 1975)
- This work proposes an artificial boundary method for PDEs to compute American option prices and Greeks under the CEV model.

Option Pricing under CEV

- Under the risk-neutral probability measure:

$$dS=(r-q)Sdt+\sigma S^{\alpha}dZ$$

- Nests several models as special cases:

(1) Local volatility given by $\sigma(S)=\sigma S^{\alpha-1}$

(2) Black-Scholes model: $\alpha=1$

(3) Ornstein-Uhlenbeck process: $\alpha=0$

(4) Square-root model: $\alpha=1/2$

- When $\alpha<1$, the local volatility increases as the stock prices decreases. This creates a probability distribution similar to the empirical distribution of equities that has a heavy left tail and a less heavy right tail.

Figure 2: Volatility smile for equities

Note: Since the financial crisis of 1987, the volatility smile used by the traders to price equity options (both on individual stocks and stock indices) had the general form shown in Fig.2.

- When $\alpha>1$, the local volatility increases as the stock price increased. This creates a probability distribution with a heavy right tail and a less heavy left tail. Such volatility smile often appears for options on futures, as shown in Fig.3.

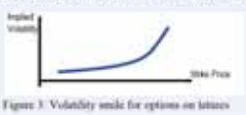

Figure 3: Volatility smile for options on futures

Option Pricing under CEV

- Closed-form solution for European options available, involves the noncentral chi-square cdf, computationally expensive→numerical PDE method: an efficient alternative approach
- No closed form solution for finite maturity American options→numerical methods, optimal strategy determined using the Bellman principle of dynamic programming
- Put-call symmetry: focus on the put option
- Advantage of implicit FDM: simple and robust, unconditionally stable, generates option prices on the entire grid of S value, easy to implement the Bellman principle
- Drawback of implicit FDM: computationally infeasible over an unbounded domain $[0, \infty)$
- A traditional approach: works on a truncated domain $[0, S_{max}]$ for some suitably large S_{max} with approximated far-field boundary condition (unknown under the CEV model)
- How "far" is enough? Large domain (accurate, but inefficient)↔Small domain (error), lacks theoretical support, tradeoff between accuracy and efficiency
- The more accurately the boundary conditions conform to the characteristics of the desired solution, the closer we can place the boundary to the domain of interest.
- Remedy: artificial boundary method (ABC)

The Proposed Approach

- Motivation: exact boundary condition?
- Idea: to introduce an artificial boundary to reduce the infinite computational domain into a finite one, on which an exact boundary condition is derived.
- Theoretical support: the problem on the bounded domain is proved to share the same solution with the original problem.
- Procedures:

(1) Transform the PDE under CEV into a standard form

(2) Introduce the artificial boundary Γ_M to divide the infinite domain into the bounded interior domain and the unbounded exterior domain ↔ exact solution of the original problem

(3) Perform FDM to the problem on the bounded domain

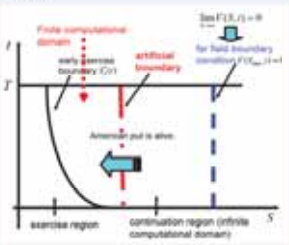

Figure 4: Illustration of the idea of artificial boundary

- Exact ABC: Neumann boundary condition involving Laplace inversion, which needs to be handled carefully.
- Analytical solution of Laplace inversion is not apparent all the time: numerical computation of the integral over a semi-infinite domain may deteriorate the efficiency.
- Technique: numerical Laplace inversion using a mixture of the Euler summation and the fast Fourier transform (FFT), which is efficient and accurate.

Numerical Experiments

- Numerical scheme:

(1) Crank-Nicolson (CN) method: an average between explicit FDM and implicit FDM, second order scheme in time and state

(2) After imposing an artificial boundary to bound the domain, we need only to solve the problem with the derived ABC.

(3) For the exact artificial boundary condition, we use trapezoid rule and numerical Laplace inversion.

- Compare with the traditional CN scheme (FDM) with far-field boundary condition for a large S_{max}.
- The proposed scheme: unconditionally stable
- Sensitivity on the truncated size, which plays a key role in the proposed method.

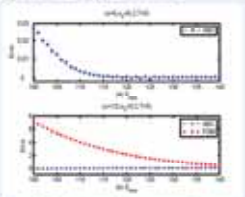

Figure 5: Sensitivity of the errors on the truncation

Note: Fig. 5 plots the errors of the proposed ABC scheme and the traditional CN scheme against the value of S_{max}. ABC method is more robust with the truncation size and the model parameters than is the FDM.

- Benchmark: For European options, closed-form pricing formulas are available. For American options, as there is no exact solution, the binomial method with many time steps is regarded to produce true values to examine the numerical scheme.
- The proposed scheme is implemented with different grid points.
- Examples:

(1) The ABC method is more efficient and accurate, which computes many option prices at the same time. By interpolation, we are able to obtain the option value on the entire domain.

(2) Many option prices are useful for computing Greeks, such as Delta and Gamma. In the financial market, the aim of the trader is to mange the Greeks so that all risk are acceptable.

(3) European options: with the same level of accuracy, the proposed ABC method is much faster than the traditional CN scheme. The binomial method with 5000 time steps also generates accurate results but is much less efficient.

(4) For American options, with a finite computational domain, the optimal strategy can be determined very efficiently by dynamic programming.

(5) American options: the ABC method outperforms the traditional CN method with its high convergent speed. Moreover, the ABC method exceeds the binomial method with its greater efficiency.

(6) We plot the computational error against the execution time for different strike price, K, in Fig. 6 for $\alpha=0$ and Fig. 7 for $\alpha=2/3$. The lower the curve, the better the performance of the scheme. It is obvious that, for all three cases, the ABC method outperforms the traditional CN scheme, especially for out-of-the money and at-the-money options.

(7) Numerical Laplace inversion: efficient

Numerical Experiments

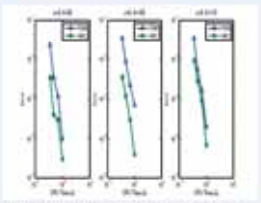

Figure 6: Error for the FDM and ABC with $\alpha=0$

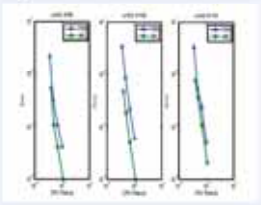

Figure 7: Error for the FDM and ABC with $\alpha=2/3$

- Order of convergence: larger than 1.5

Conclusion

- This work proposes an artificial boundary method for PDEs to compute American option prices and Greeks under the CEV model.
- The idea is to reduce the infinite computational domain into a finite one by introducing an artificial boundary, on which an exact boundary condition is derived.
- Boundary condition: approximated→exact
- Computational domain: infinite→finite
- Several examples are implemented.
- With a finite computational domain, the optimal exercise boundary can be determined efficiently.
- The proposed scheme is accurate, robust with respect to the truncation size, and more efficient than alternative methods for accurate option prices.
- This work lays the theoretical grounds for option pricing under CEV with an FDM.

References

[1] A. BECKER, *The constant elasticity of variance model and its implications for option pricing*, J. Finance, 35 (1980), pp. 661-673.

[2] P. CARR, R. JARROW, AND R. MYNENI, *Alternative characterizations of American put options*, Math. Finance, 2 (1992), pp. 87-106.

[3] J. COX, *Notes on Option Pricing I: Constant Elasticity of Variance Diffusions*, working paper, Stanford University, 1975 (reprinted in J. Portfolio Management, 22 (1996), pp.15-17).

[4] H. HAN AND X. WU, *A fast numerical method for the Black-Scholes equation of American options*, SIAM J. Numer. Anal., 41 (2003), pp. 2081-2095.

[5] R. KANGRO AND R. NICOLAIDES, *Far field boundary conditions for Black-Scholes equations*, SIAM J. Numer. Anal., 38 (2000), pp. 1357-1368.

[6] M. SCHRODER, *Computing the constant elasticity of variance option pricing formula*, J. Finance, 44 (1989), pp. 211-219.

[7] D. WINDCLIFF, P. A. FORSYTH, AND K. R. VETZAL, *Analysis of the stability of the linear boundary condition for the Black-Scholes equation*, J. Comput. Finance, 8 (2004), pp.65-92.

[8] H. Y. WONG AND J. ZHAO, *An artificial boundary method for American option pricing under the CEV model*, SIAM J. Numer. Anal., 46 (2008), pp. 2183-2209.

Contact information

For further information please contact Jing ZHAO (jzhao@sta.cuhk.edu.hk).

Acknowledgement: Special thanks go to the advisor, Dr. Hoi Ying WONG.

LAU Ting Fong **Supervisor: Prof. Dennis NG**
Department of Chemistry, Faculty of Science

Student Poster

Project Title "Synthesis, Photophysical Properties, and in vitro Photodynamic Activities of β-Cyclodextrin Conjugated Silicon(IV) Phthalocyanines"

Synthesis, Photophysical Properties, and *in vitro* Photodynamic Activities of β-Cyclodextrin Conjugated Silicon(IV) Phthalocyanines

Janet T. F. Lau,[a] Wing-Ping Fong,[b] and Dennis K. P. Ng*[,a]

[a]*Department of Chemistry and Center of Novel Functional Molecules, The Chinese University of Hong Kong, Shatin, N.T., Hong Kong, China*
[b]*Department of Biochemistry and Center of Novel Functional Molecules, The Chinese University of Hong Kong, Shatin, N.T., Hong Kong, China*

Introduction

Photodynamic therapy (PDT) is an innovative therapeutic modality for the treatment of a variety of malignant tumors and wet age-related macular degeneration.[1] It involves a non-invasive process with three individually non-toxic components, namely a photosensitizer, visible light, and oxygen. Owing to the desirable photophysical and photochemical properties, phthalocyanines have been widely studied as second-generation photosensitizers for PDT. However, the intrinsic aggregation tendency and poor solubility of these macrocycles in aqueous environment somewhat limit their application in this area. To alleviate these problems, we have designed and synthesized a novel series of silicon(IV) phthalocyanines axially substitutec with two permethylated β-cyclodextrin moieties through different spacers (compounds **4a-d**). By taking the advantage of the biocompatability and hydrophilicity of the cyclodextrin moieties, we aim to increase the water solubility of the macrocycles and facilitate the formation of monomeric species, thereby enhancing the photosensitizing efficiency.[2] We describe herein the synthesis, photophysical properties, and *in vitro* photodynamic activities of these phthalocyanine compounds.

Synthesis

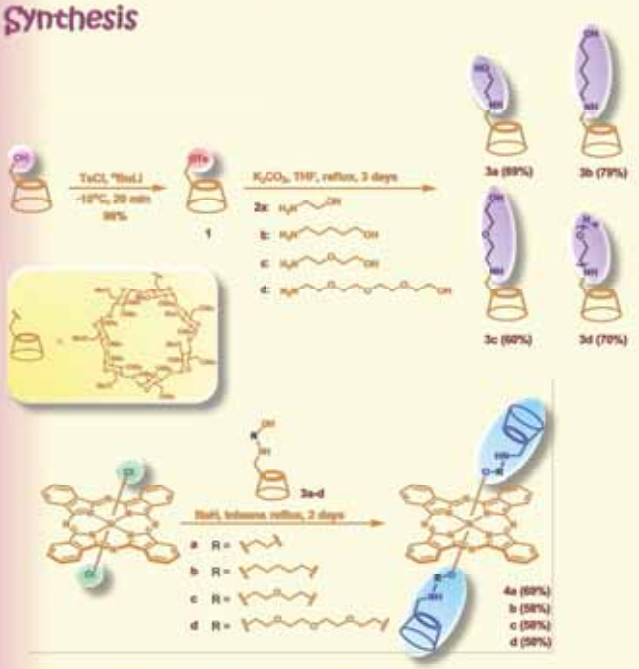

Photophysical Properties

Table 1 shows the electronic absorption and basic photophysical data of **4a-d** in DMF. Owing to the fact that **4a** pcssesses the shortest spacers, the amino groups are close to the macrocycle and can reductively quench its singlet excited state in an effective manner. Hence, the fluorescence (Φ_F) and singlet oxygen quantum yields (Φ_Δ) of the compound are comparatively lower.

Table 1

Compound	λ_{max} (nm) (log ε)	λ_{em}(nm)[a]	Φ_F[b]	Φ_Δ[c]
4a	355 (4.90), 606 (4.61), 643 (4.55), 674 (5.38)	678	0.20	0.19
4b	355 (4.88), 606 (4.61), 642 (4.55), 673 (5.39)	675	0.40	0.36
4c	356 (4.83), 606 (4.57), 645 (4.51), 674 (5.35)	676	0.36	0.33
4d	355 (4.89), 606 (4.63), 643 (4.57), 674 (5.41)	678	0.40	0.36

[a] Excited at 610 nm. [b] Using unsubstituted zinc(II) phthalocyanine (ZnPc) as the reference [fluorescence quantum yield (Φ_F) = 0.28 in DMF]. [c] Using ZnPc as the reference [singlet oxygen quantum yield (Φ_Δ) = 0.56 in DMF].

in Vitro Photodynamic Activities

Phthalocyanines **4a-d** are all photocytotoxic against HT29 human colon hepatocarcinoma and HepG2 human hepatocarcinoma cells. Figure 1, showing their dose-response curves against HT29 cells, is given below as an example. The corresponding IC_{50} values are summarized in Table 2.

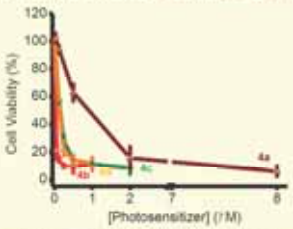

Figure 1. Effects of **4a-d** on HT29 in the presence of light (λ = 610 nm, 40 mW / cm², 48 J / cm²).

Table 2

Sample	HT29 IC_{50}* (μM)	HepG2 IC_{50}* (μM)
4a	0.91	1.32
4b	0.04	0.05
4c	0.16	0.17
4d	0.14	0.15

* Defined as the dye concentration required to kill 50% of the cells.

The difference in *in vitro* photocytotoxicities of these compounds is well correlated with the difference in intracellular reactive oxygen species (ROS) production efficacy as shown in Figure 2. Aggregation does not seem to be an important factor as a strong Q-band was observed for all these compounds in the culture media (Figure 3).

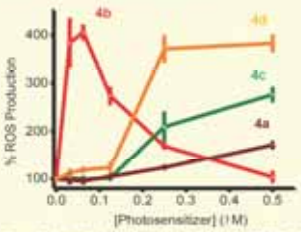

Figure 2. Intracellular ROS production of **4a -d** of HT29 in the presence of light (λ = 610 nm, 40 mW / cm², 48 J / cm²).

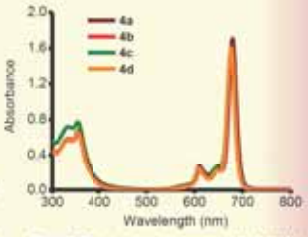

Figure 3. Electronic absorption spectra of **4a-d** (8 μM) in the DMEM culture medium (for HT29 cells).

Subcellular Localization Properties

Apart from cell viability studies, we also employed confocal microscopy to study the subcellular localization properties of **4b** in HT29 cells. As shown in Figure 4, the fluorescence caused by **4b** and the LysoTracker Green (a dye resides specifically in the lysosomes) is well superimposed with each other. This observation suggests that **4b** can target lysosomes, an important organelle to initiate apoptosis in PDT,[3] of the HT29 cells.

Figure 4. Visualization of intracellular fluorescence of HT29 using filter sets specific for (a) phthalocyanine **4b** (in red) and (b) the LysoTracker Green (in green). Figure c shows the corresponding superimposed image.

Conclusion

In summary, we have synthesized and characterized a series of silicon(IV) phthalocyanines conjugated with permethylated β-cyclodextrin moieties through various spacers. The cyclodextrin moieties can reduce the aggregation and increase the water solubility of these marcocycles. Phthalocyanine **4b** exhibits the highest photocytotoxicity toward HT29 and HepG2 cells. It generates ROS efficiently and targets lysosomes of the HT29 cells.

Acknowledgment

This work was supported by the Research Grants Council of the Hong Kong Special Administrative Region, China (Project No. 402306).

References

1. Castano, A. P.; Mroz, P.; Hamblin, M. R. *Nat. Rev. Cancer* **2006**, *6*, 535.
2. Moan, J. *J. Photochem. Photobiol., B: Biol.* **1990**, *5*, 521.
3. Olenick, N. L.; Morris, R. L.; Belichenko, I. *Photochem. Photobiol. Sci.* **2002**, *1*, 1.

DONG Jia qiang **Supervisor: Prof. N C WONG**
Department of Chemistry, Faculty of Science

Project Title "Studies Toward the Total Synthesis of a Naturally Occurring Diterpene"

Joint Faculty Research Day 2008

香港中文大學
The Chinese University of Hong Kong

Studies Toward the Total Synthesis of a Naturally Occurring Diterpene

Jia-qiang Dongand Henry N. C. Wong*

Department of Chemistry, Centre of Novel Functional Molecules, Institute of Chinese Medicine and Institute of Molecular Technology for Drug Discovery and Synthesis, the Chinese University of Hong Kong, *Shatin, New Territories, Hong Kong SAR, China*

Introduction

Liverworts biosynthesized many novel new skeletons of diterpenoids with interesting and diversified bioactivities.[1] Thus, the total synthesis and structural modification of these molecules are of synthetic and pharmaceutical importance. In our previous work, the total syntheses of (±)-pallavicinin and (±)-neopallavicinin had been completed.[2] As a continuing research program, we are now exploring the total synthesis of another novel skeletal diterpene **1** (Scheme 1) which was isolated from the Japanese liverwort *Pallavicinia subciliata*.[3]

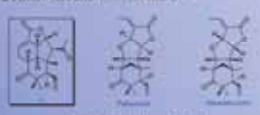

Scheme 1. Structure of novel diterpene

The target molecule **1** is shown to be a modified labdane-type diterpene. As shown in Scheme 2, it was presumed that the biosynthesis was performed by C7-C8 bond cleavage of labdane, followed by bond reconstruction of C15-C2 and C12-C1.[4,5]

Scheme 2. Possible biogenetic pathway of 1

Results and Discussion

Encouraged by our recent success in the syntheses of naturally occurring molecules[1,2] and the above biogenetic pathway,[4,5] we designed the following synthetic route to study the total synthesis of **1** from the simple (*S*)-Wieland-Miescher ketone **2**. The retro-synthetic analysis is shown in Scheme 3.

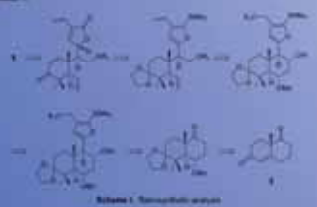

Scheme 3. Retrosynthetic analysis

As shown in Scheme 4, after several steps, the starting material (*S*)-Wieland-Miescher ketone **2** was converted to intermediate **7** which partially satisfied the stereochemical requirements of the Grob fragmentation.

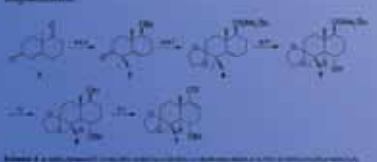

Scheme 4.

Scheme 5 shows the synthesis of another crucial structural motif. Thus, the commercially available 3-furoic acid **8** underwent preferentially 2-lithiation followed by anylation to give the compound **9**. After reduction by LAH and

protection, the intermediate **11** was obtained in high yield.

Scheme 5.

As shown in Scheme 6, we tried to convert **7** to the desired **1** following the sequence Coupling-Grob fragmentation-Oxidation of furan ring-D-A cyclization. Firstly, Negishi coupling between vinyl triflate **7** and furan derivative **11** afforded the pivotal olefin **12** in good yield. After hydroboration and protection, the intermediate **14** containing an epoxide and furyl group was obtained. The Grob fragmentation precursor **16** was prepared smoothly after catalytic hydrogenation, mesylation and deprotection. However, the key Grob fragmentation[6] gave an inseparable mixture of products with about 5:1 diastereomeric ratio. Many attempts failed to give much higher dr value of this reaction by controlling the amount of base, temperature, the sequence of reagents and using different base, etc. Then we tried to separate them by converting **18** to **19**, unfortunately, it was still hard to be separated.

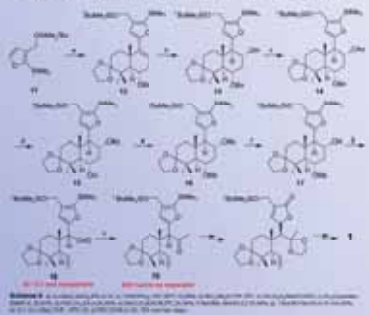

Scheme 6.

So we reduced the crude aldehyde **18** to their alcohol. Fortunately, after careful column chromatography, alcohol **20** was obtained in a moderate yield. By the X-ray analysis of its derivative **23**, we confirmed that the main isomer from Grob fragmentation was our desired one. (Scheme 7).

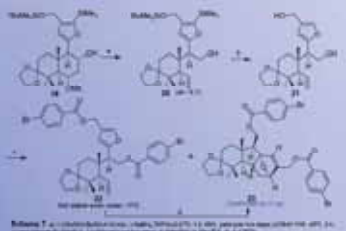

Scheme 7.

After 4 steps, alcohol **26** was then converted to the intermediate **27** (Scheme 8).

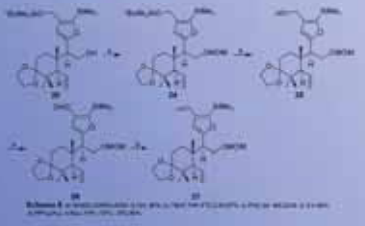

Scheme 8.

With compound **27** in hand, we then focused on the oxidation of furan species to the corresponding butenolide. After considerable investigation, we found that when the compound **27** was allowed to react with singlet oxygen[7] followed by Luche reduction,[8] the butenolide **28** as the main isomer was obtained in good yield with about 5:1 dr value. After deprotection, ketone **29** was formed and it was confirmed by X-ray analysis (Scheme 9).

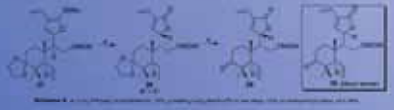

Scheme 9.

It was worthy to note that the obtained ketone **29** was the epimer of our desired one. We presumed that the epimerization occurred during the singlet oxygenation. Using this intermediate, we will obtained the epimer **1'** of our desired product and it could be converted to the latter by base-promoted enolization (Scheme 10).

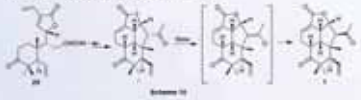

Scheme 10.

Then we began to explore a method to form the D-A precusor. Many routine methods were tried However, all of them gave negative results. At last, the α,β-unsaturated ketone **32** was obtained successfully by using Mukaiyama's method.[10] This substrate underwent an IMDA cycloaddition when heated in toluene to give a mixture of cycloadduct **33** and its de-MOM product **34**. The diastereochemistry of **34** was confirmed by X-ray analysis. We presumed that the formation of this molecule was due to the epimerization during the double bond production (Scheme 11).

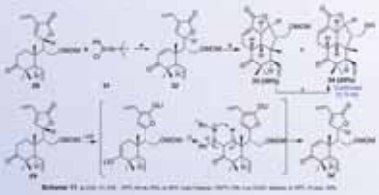

Scheme 11.

After the next oxidation, careful addition of the forming aldehyde by methyllithium and the second oxidation, the diastereosomer **37** of the natural product was obtained (Scheme 12).

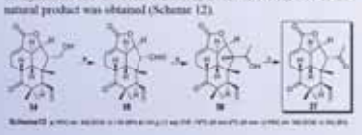

Scheme 12.

Conclusion

In conclusion, the diastereisomer **37** of the natural molecule was obtained starting from (*S*)-Wieland-Miescher ketone in 34 steps of longest linear sequence with an overall yield of 0.11%. Now we are checking our synthetic route toward the natural product.

Acknowledgements

The work described in this project is fully supported by a grant from the Research Grants Council of the Hong Kong Special Administrative Region, China (Project No. CUHK 403505) and Area of Excellence Scheme established under the University Grants Committee of the Hong Kong SAR, China (Project No. AoE/P-10/01).

References and Notes

‡An Area of Excellence of the University Grants Committee (Hong Kong)
* To whom correspondence should be addressed. E-mail: hncwong@cuhk.edu.hk

(1) V. Asakawa, *Phytochemistry* **2001**, *56*, 297-317.
(2) X. S. Peng, H. N. C. Wong, *Chem. Asian. J* **2006**, *1*, 111-120.
(3) M. Toyota, T. Sato, Y. Asakawa, *Chem. Pharm. Bull.* **1998**, *46*, 178-180.
(4) *Z. J. Li, H. X. Lou, W. T. Yu, P. H. Fan, H. M. Ren, B. Ma, M. S. Shi, Chin. Chem. Acta* **2005**, *63*, 2637-2640.
(5) a) H. K. Yim, Y. Liao, H. N. C. Wong, *Tetrahedron* **2003**, *59*, 1877-1884; b) H. K. Lee, H. N. C. Wong, *Chem Commun.* **2002**, *19*, 2114-2115; c) W. S. Cheung, H. N. C. Wong, *Tetrahedron* **1999**,*55*,10301-10316; d) F. Yu, Y. Yang, *Z. Y. Zhang, T. C. W. Mak, H. N. C. Wong, J. Org. Chem.* **1997**, *62*, 6359-6366.
(6) C.A. Grob, P. W. Schiess, *Angew. Chem. Int. Ed. Engl.* **1967**, *6*, 1-15.
(7) D. Dobkowski, D. Lipiak, M. Jasiukiewz, L. Wicherska, P. Bertran, *Tetrahedron Lett.* **1983**, *24*, 5035-5038.
(8) P. G. Steel, O. S. Mills, E. R. Portmer, E. J. Thomas, *J. Chem. Soc., Perkin Trans. 1* **1997**, 391-400.
(9) a) T. L. Luche, *J. Am. Chem. Soc.* **1978**, *100*, 2226-2227; b) M. Tajuria, P. L. Suarez, G. Grimaz, C. Tarna, Y. Fall, *Tetrahedron Lett.* **2000**, *41*, 5889-5892.
(10) T. Mukaiyama, J. Matsuo, T. Kitagawa, *Chem. Lett.* **2000**, 1250.

CHAK Chun Pong **Supervisor: Prof. LEUNG Cham Fai**
Department of Chemistry, Faculty of Science

Student Poster

Project Title "Superparamagnetic Iron Oxide Nanostructures for Cell Labeling and Magnetic Resonance Imaging"

Superparamagnetic Iron Oxide Nanostructures for Cell Labeling and Magnetic Resonance Imaging

Center of Novel Functional Molecules

Ken Cham-Fai Leung,*[1] Chun-Pong Chak,[1] Yi-Xiang J. Wang[2] and Hao-Hao Wang[2]

[1] *Center of Novel Functional Molecules and Department of Chemistry*
[2] *Department of Diagnostic Radiology and Organ Imaging, Prince of Wales Hospital*
The Chinese University of Hong Kong, Shatin, NT.

Introduction

RECENTLY, magnetic nanomaterials have been demonstrated to give tremendous applications in the separation of biomolecules, biocompatible contrast agents for magnetic resonance imaging (MRI), magnetic recording, spintronic devices and magnetic sensing. It has been demonstrated that the size, structure, and the functional surfaces of many spherical superparamagnetic iron oxide (SPIO) — magnetite (Fe_3O_4) nanoparticles are important parameters which influence the rate of cell attachment and uptake for specifically controlled substrate release or cell labeling.

Novel Nanostructures Prepared from Mn-Doped SPIO

Mn-Doped SPIO Nanoparticles Prepared by Co-Precipitation

Cystamine, R.T., Magnetic stirring

1-D Nanostructures

TEM images. (A) Mn-doped SPIO nanoparticles (d ~ 4 nm); (B), (C) nanowires (d ~ 38 nm, ~ 1 μm long); (D) nanorods (d ~ 30 nm); (E) and (F) nanoneedles (d ~ 8 nm).

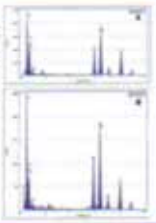

EDX spectrum of (A) Mn-doped SPIO and (B) organized nanowires prepared from Mn-doped SPIO.

Objective —

Modification of SPIO Nanoparticles

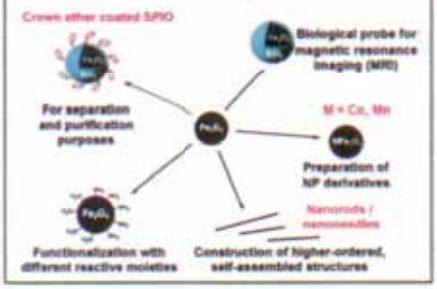

The Concept —

Magnetic Contrast Evaluation and Macrophage Cell Labeling

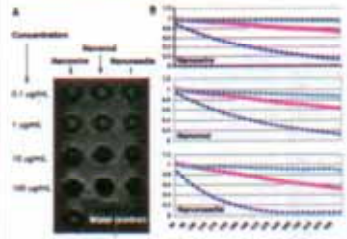

(A) MRI T2 relaxation property of the nanostructures. (B) X-axis = time of echo (TE); Y-axis = signal intensity of the nanoarchitecture suspensions against water (control). (♦), (■) and (▲) denote the concentration of 100, 10, and 1 μg/ mL, respectively. Nanoneedles revealed highest MR relaxivity.

Optical microscope images of the Raw264.7 cells with Prussian blue staining detection: (A) Control cells without nanowires labeling [Magnification: 400X]. (B) Cells incubated with nanowires at the concentration of 28 μg [Fe]/mL for 3 hours [Magnification: 800×].

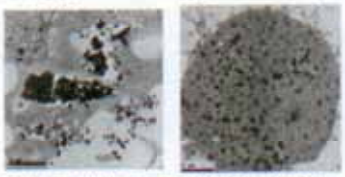

TEM images of the nanowires-labeled macrophage cells. The arrow represents some of the nanowires in the lysosome.

Ongoing Work —

Separation of Monofunctionalized Nanoparticles

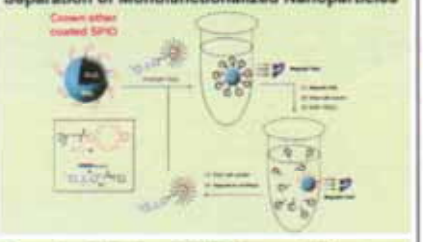

Functionalization of SPIO Nanoparticles with Biomolecules

e.g., Biotin, Streptavidin, etc. (Collaborate with Prof. Paula M. Mendes at the Department of Chemical Engineering, University of Birmingham, UK)

SPIO Nanosphere Derivatives for Stem Cell Labeling —

TEM image of the silica-coated SPIO nanoparticles (d ~ 5 nm)

Stem cells treated with SPIO nanoparticles, showing substantial nanoparticle uptake

Single, rabbit bone marrow derived stem cell with substantial SPIO nanoparticle uptake

Conclusions

— One-dimensional nanostructures were prepared from the as-synthesized Mn-doped SPIO nanoparticles.
— Magnetic relaxivities of the nanostructure were measured. All nanostructures can be used as MR contrast agents, in which nanoneedles have the highest signal.
— Nanowires were incubated with macrophage cells. Substantial uptake of the nanowires by Raw264.7 cells is demonstrated after Prussian blue staining.
— SPIO nanosphere derivatives were incubated with rabbit bone marrow derived stem cells. Substantial uptake of the nanoparticles by stem cells is demonstrated.

References

J.-H. Lee, *et al. Nature Medicine* **2007**, *13*, 95-99. A. Petri-Fink, *et al. IEEE Transactions on Nanobioscience* **2007**, *6*, 289-297. N. Nitin, *et al. Journal of Biological Inorganic Chemistry* **2004**, *9*, 706-712. Y.-X. J. Wang, *et al. European Radiology* **2001**, *11*, 2319-2331.

Acknowledgments Financial support: Innovation Technology Commission, Hong Kong SAR (ITS016/07) and CUHK Direct Grant for Research (2060301); Prof. Doris Au (CityU, for TEM analysis); Mr. Man-Hau Yeung (Physics, CUHK, for TEM, EDX, XRD measurements).

YANG Hao **Supervisor: Prof. Sik Lok LAM**
Department of Chemistry, Faculty of Science

Project Title "How does 1-methylation of adenine affect DNA structure? A Hoogsteen base pair embedded in DNA double helix"

How does 1-methylation of adenine affect DNA structure? A Hoogsteen base pair embedded in DNA double helix

Hao YANG, Yingqian ZHAN, Dickson FENN, Lai Man CHI and Sik Lok LAM*
Department of Chemistry, The Chinese University of Hong Kong
E-mail: lams@cuhk.edu.hk

Introduction

Methylation at the N1 site of adenine leads to the formation of cytotoxic 1-methyladenine (m1A) which blocks DNA replication if not being repaired. Owing to the fact that the N1 site of adenine is involved in the hydrogen bonding of T•A and A•T Watson-Crick base pairs, it is expected that the base pair structure of DNA double-helix will be seriously affected upon 1-methylation. In this study, we have investigated the T•A base pair structure upon methylation at the N1 site of adenine using high-resolution NMR spectroscopy.

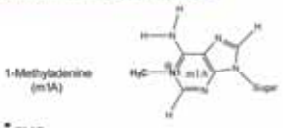

Sample Design

NMR Study

(i) Special T•m1A base pairing mode indicated by a upfield T4 imino peak

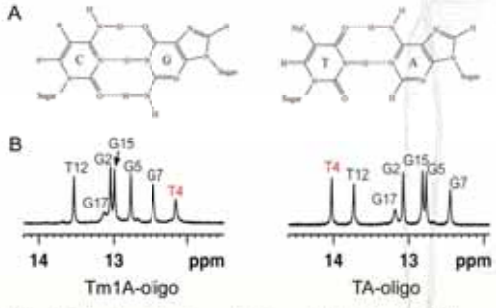

Fig. 1. (A) Chemical structures of Watson-Crick C•G and T•A base pairs. (B) Imino ^{1}H spectra at 5 °C of Tm1A-oligo (left) and TA-oligo (right).

(ii) T•m1A Hoogsteen base pair indicated by charasteric NOEs

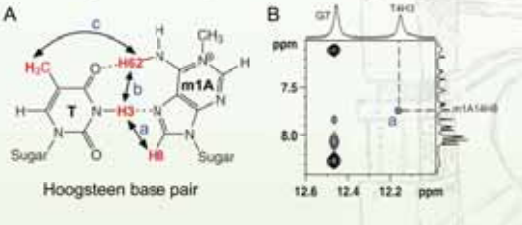

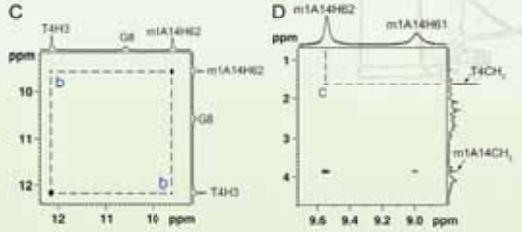

Fig. 2. (A) Schemes of T•m1A Hoogsteen base pair. Black arrows indicate its characteristic NOEs. (B) T4H3-m1A14H8, (C) T4H3-m1A14H62 and (D) T4CH$_3$-m1A14H62 NOEs were observed in the WATERGATE-NOESY spectrum of Tm1A-oligo at 5 °C.

(iii) T and m1A adopt *anti* and *syn* orientation respectively indicated by H6/H8-H1' NOE intensities

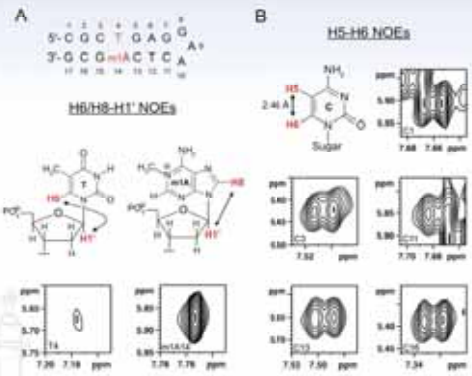

Fig. 3. NOE crosspeaks of (A) H6/H8-H1' of T4 and m1A14, and (B) H5-H6 of C1, C3, C11, C13 and C16. These NOEs were plotted using the same baseline threshold. 2D NOESY was performed with a mixing time of 100 ms.

(iv) 1-Methylation of adenine only has a local effect to sugar pucker (Table 1) and backbone conformation (Table 2 and Fig. 4.)

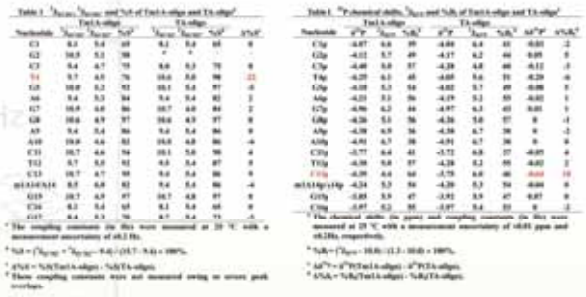

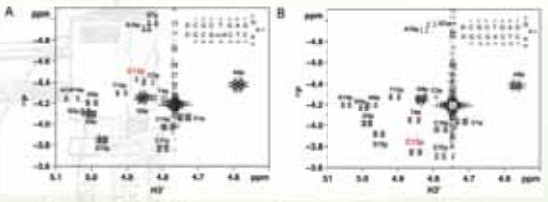

Fig. 4. ^{1}H-^{31}P COSY spectra of (A) Tm1A-oligo and (B) TA-oligo.

Summary

We found that upon 1-methylation on adenine, the T•A Watson-Crick base pair is switched to T•m1A Hoogsteen base pair. The structural findings provide possible explanations for the experimental observed differences in the AlkB-repair efficiency between dsDNA and ssDNA as the T·m1A Hoogsteen base pair remains stacked in the DNA double-helix,which possibly makes the recognition and thus the repair of m1A lesion in dsDNA by AlkB less efficient than that in ssDNA.

Acknowledgements

Research Grants Council of the Hong Kong Special Administrative Region, China (Project No.: CUHK401105).

Reference

Yang, H., Zhan, Y.Q., Chi, L.M., Fenn, D. and Lam, S.L., FEBS Lett. (2008), doi:10.1016/j.febslet.2008.04.013